# ISTANBUL TECHNICAL UNIVERSITY ★ GRADUATE SCHOOL OF SCIENCE ENGINEERING AND TECHNOLOGY

## MECHANICAL PROPERTIES OF CARBON NANOTUBE AND GRAPHENE BASED YARNS

**M.Sc. THESIS**

**Esma Nur GÜLLÜOĞLU**

**Department of Textile Engineering**

**Textile Engineering Programme**

**NOVEMBER 2017**

**ISTANBUL TECHNICAL UNIVERSITY ★ GRADUATE SCHOOL OF SCIENCE ENGINEERING AND TECHNOLOGY**

**MECHANICAL PROPERTIES OF CARBON NANOTUBE AND GRAPHENE BASED YARNS**

**M.Sc. THESIS**

**Esma Nur GÜLLÜOĞLU**

**503151803**

**Department of Textile Engineering**

**Textile Engineering Programme**

**Thesis Advisor: Assist. Prof. Dr. Elif ÖZDEN YENİGÜN**

**NOVEMBER 2017**

**ISTANBUL TEKNİK ÜNİVERSİTESİ ★ FEN BİLİMLERİ ENSTİTÜSÜ**

**KARBON NANOTÜP VE GRAFEN ESASLI İPLİKLERİN MEKANİK ÖZELLİKLERİ**

**YÜKSEK LİSANS TEZİ**

**Esma Nur GÜLLÜOĞLU**
**503151803**

**Tekstil Mühendisliği Anabilim Dalı**

**Tekstil Mühendisliği Programı**

**Tez Danışmanı: Yard. Doç. Dr. Elif ÖZDEN YENİGÜN**

**KASIM 2017**

Esma Nur Güllüoğlu, a M.Sc. student of ITU Graduate School of Textile Engineering student ID 503151803, successfully defended the thesis entitled "MECHANICAL PROPERTIES OF CARBON NANOTUBE AND GRAPHENE BASED YARNS", which she prepared after fulfilling the requirements specified in the associated legislations, before the jury whose signatures are below.

**Thesis Advisor:**      **Assist. Prof. Dr. Elif ÖZDEN YENİGÜN**   ...........................
ISTANBUL Technical University

**Jury Members:**      **Assoc. Prof. Dr. Hülya CEBECİ**          ...........................
ISTANBUL Technical University

                       **Assist. Prof. Dr. Özgür DEMİR**         ...........................
YILDIZ Technical University

**Date of Submission : 6 November 2017**
**Date of Defense       : 9 November 2017**

*To my Family,*

## FOREWORD

This work was accomplished with the support of a number of professionals, friends, and family members. Firstly, I would like to express our special gratitude to our supervisor Asst. Prof. Dr. Elif ÖZDEN YENİGÜN for her excellent guidance, strongly supports and timely suggestions throughout this research not only professionally but also personally.

November 2017                                                    Esma Nur GÜLLÜOĞLU

                                                                     (Textile Engineer)

**TABLE OF CONTENT**

## ABBREVIATIONS

| | |
|---|---|
| **AA** | : Ascorbic Acid |
| **CNTs** | : Carbon Nanotubes |
| **CTAB** | : Cetyl Trimethyl Ammonium Bromide |
| **CVD** | : Chemical Vapor Deposition |
| **DI** | : Deionized |
| **DWCNTs** | : Doublewall Carbon Nanotube |
| **E-Beam** | : Electron Beam |
| **GBFs** | : Graphene-Based Fiber |
| **GMA** | : Glycidyl Methacrylate |
| **GO** | : Graphene Oxide |
| **GOLCs** | : Graphene Oxide Liquid Crystal |
| **HI** | : Hydroiodic Acid |
| **HPG** | : Hyperbranched Polyglycerol |
| **HRTEM** | : Resolution Transmission Electron Microscopy |
| **MFC** | : Mass Flow Controller |
| **MWCNTs** | : Multiwall Carbon Nanotube |
| **NA** | : Not Available |
| **PAN** | : Polyacrylonitrile |
| **PECVD** | : Plasma Enhanced CVD |
| **PLC** | : Programmable Logic Controller |
| **PP** | : Polypropylene |
| **rGO** | : Reduced Graphene Oxide |
| **SEM** | : Scanning Electron Microscopy |
| **SWCNTs** | : Single Wall Carbon Nanotube |
| **th-CVD** | : Thermal Chemical Vapor Deposition |
| **UHV** | : Ultra-High Vacuum. |
| **UTM** | : Universal Testing Machine |
| **VA-CNT** | : Vertically Aligned Carbon Nanotube |
| **VC** | : Vitamin C |
| **XRD** | : X-Ray Diffraction |

# LIST OF TABLES

# MECHANICAL PROPERTIES OF CARBON NANOTUBE AND GRAPHENE BASED YARNS

## SUMMARY

Carbon allotropes including graphene and carbon nanotubes (CNTs) have superior mechanical, electrical and thermal properties. Both in academia and industry, these nanomaterials offer a wide range of application areas. Transferring their superior material performance at the nanomaterial level to the macro scale applications is quite challenging which also includes material, and process related problems. To overcome aforementioned problems, the "fiber" macroscopic form is an important structural assembly that can convey the nano-scale properties of graphene and CNTs to much larger scale.

This thesis traces the fiber manufacturing of carbon nanomaterials such as graphene and CNTs via traditional spinning approaches by following the methods below:

- First focus is on the wet-spinning of graphene fibers. This method started with the graphene oxide (GO) synthesis. Then, custom-made wet spinning line was used to spin GO fibers continuously. Consecutively, GO fibers were reduced to obtain graphene fibers using chemical reduction methods.
- Second objective of this thesis is to spin pure CNTs fibers from CNTs arrays. Hence, dry spinning method was selected for fiber formation. CNTs production was optimized to have spinnable CNTs arrays.

First, this thesis aimed to produce flexible and strong graphene fibers. GO nanosheets were chemically exfoliated by using the modified Hummer's method. This approach enabled to achieve highly oriented graphene oxide liquid crystals (GOLCs), where GO nanosheets were dispersed in aqueous solutions. The physical properties of GO nanosheets were confirmed by X-ray diffraction (XRD) and Raman spectroscopy, which also pointed out their potential use as of spinning solution. Fiber spinning procedure was carried out by varying GO concentrations and coagulation baths. 30 and 40 mg ml$^{-1}$ GO concentrations enabled continuous GO fiber spinning, where coagulation baths with composition of 3-5% NaOH / Ethanol and 3-5% CaCl$_2$ / Ethanol: Deionized water (3: 1) assisted the structural integrity of fibers throughout spinning. Further washing step with methanol was added to remove coagulation bath residues on GO fibers. To gain electrical conductivity, GO reduction was carried out by using Hydroiodic Acid (HI), Ascorbic Acid (AA) and Sodium borohydride (NaBH$_4$) chemicals. Subsequent NaBH$_4$ chemical reduction gave graphene fibers with highest electrical conductivity of 214 S cm$^{-1}$. The results showed that as-spun GO fibers with specific ultimate tensile strength of 7 N/tex show strain to failure (%) of 10%, which pointed out much higher ductility compared to studies in literature.

Second objective of this thesis was to explore CNTs fiber production from vertically aligned carbon nanotubes (VA-CNTs) by the implementation of dry spinning method. First, multi-walled CNTs were produced on a coated silicon bed by chemical vapor deposition (CVD) method, which also enables high purity and ease in scalable manufacturing. Several material and process parameters such as coating material, CVD production temperature and process time, nature of carbon source were systematically studied by monitoring the changes in length of individual CNTs and

their associated spinnability. Four different types of wafers with different compositions such as Fe (~ 2nm), $SiO_2$ (~ 300 nm), $Al_2O_3$ (~10 nm) and Fe (~ 2nm), $Al_2O_3$ (~10 nm) and Fe (~ 2nm), $Al_2O_3$ (~10 nm) and Fe (~ 6nm) were used in CVD system where helium/hydrogen and ethylene gases were used as carrier gases and carbon source, respectively. The effect of water vapor on the spinnability of CNTs were also investigated. Each CNTs arrays was indexed based on their length and spinnability. Apart from their ease in fiber spinning, the intensity ratio of D and G peak ($I_D/I_G$) were examined by Raman spectroscopy. The length of CNTs arrays were measured by image processing from optical microscope images. Custom-made dry spinning device, which included a motor enabling x-axis movement, another motor for twisting and a mounted stage for CNTs arrays, was built.

# KARBON NANOTÜP VE GRAFEN ESASLI İPLİKLERİN MEKANİK ÖZELLİKLERİ

## ÖZET

Grafen ve karbon nanotüpler (KNT'ler) de dâhil olmak üzere karbon allotropları, üstün mekanik, elektriksel ve termal özelliklere sahiptir. Bu malzemeler akademik çalışmalarda ve endüstriyel alanda çok çeşitli uygulama alanları sunmaktadır.

Nano düzeyde olan grafenin ve karbon nanotüp (KNT) malzemelerin moleküler mertebede gözlemlenen üstün malzeme performansının makro boyuta taşınması günümüzde ihtiyaç duyulan ve üzerinde çalışılan çalışma alanları arasında yer almaktadır. Bu alanda üzerinde çalışılması gereken malzeme, işleme ve süreç kaynaklı problemler bulunmaktadır. Ortaya çıkan problemleri çözme aşamasında "lif" formu, grafeni ve KNT kullanılabilir ölçeğe taşıyabilecek önemli yapısal formdur.

Bu tez, geleneksel iplikçilik yaklaşımlarını kullanarak grafen ve KNTler gibi karbon nanomalzemelerinin lif üretiminde aşağıdaki yöntemleri izlemektedir:

- Birincisi, grafen elyaflarının ıslak çekilmesidir. Bu yöntem, grafen oksit (GO) sentezi ile başlamıştır. Daha sonra GO elyaflarını sürekli olarak üretebilmek için özel ıslak çekim hattı kullanılmıştır. Ardından GO lifleri, kimyasal indirgeme yöntemleri kullanılarak grafen lifleri elde etmek üzere indirgenmiştir

- Bu tezin ikinci amacı, KNT dizilerinden saf KNT liflerini çekebilmektir. Bu nedenle elyaf oluşumu için kuru çekim yöntemi seçilmiştir. KNT'lerin üretimi için çekilebilir KNT dizileri optimize edilmiştir.

Bu tezin birincil amacı, esnek ve güçlü grafen lifleri üretmektir. Grafen iplik üretimi için öncelikle nano boyutlardaki GO parçacıkların ölçeklenebilir şekilde kimyasal eksfoliasyon yöntemine göre sentezlenmiştir. Modifiye Hummer metodu olarak da bilinen bu yöntemin seçilme sebebi endüstriyel boyutta da kullanılabilirliği ve bu alanda çevreye duyarlı (su bazlı) dispersiyonlarının hazırlanarak düzenli likit kristal yapının elde edilebilmesidir. Üretilen GO nanokatmanların fiziksel özellikleri, X ışını kırınımı (XRD) ve Raman spektroskopisi ile teyit edilmiş ve likit dispersiyonlarının lif çekiminde solüsyon olarak kullanımının uygun olduğu görülmüştür. GO sentezini takip eden aşamada laboratuvar ölçeğinde ıslak lif çekim hattının oluşturulması ve bu kurgunun endüstriyel boyuta geçişe olanak sağlayabilecek şekilde olması yer alır. GO malzemesini sisteme basan kısım, pıhtılaşma banyosu, yıkama banyosu ve toplama silindirinden oluşan hattın optimizasyonu yapılmıştır. Yapılan deneysel çalışmalarda çeşitli konsantrasyonlardaki GO yapıları ve oluşturulan ıslak çekim hattında bu süspansiyonların sırasıyla geçtiği çeşitli konsantrasyonlarda pıhtılaşma banyoları ve yıkama banyoları denenmiştir. Lifin yapısal formunu koruyabildiği gözlemlenen konsantrasyonların 30 mg ml$^{-1}$ GO ve 40 mg ml$^{-1}$ GO olduğu görülmüştür.

% 3-5 NaOH / Etanol ve % 3-5 $CaCl_2$ / Etanol: Deionize su (3:1) kompozisyonlara sahip koagülasyon banyolarının, liflerin yapısal bütünlüğüne yardımcı olduğu iplik boyunca sürekli GO fiber eğirmeyi sağladı gözlemlenmiştir. Ek olarak akabinde bulunan yıkama banyosu olarak metanol kullanımının lif formunu korumaya yardımcı olduğu ve mekanik özelliklerine katkı sağladığı görülmüştür. Üretilen GO liflerinin mekanik özelliklerin analizi çekme testiyle gerçekleştirilmiştir. Buna ek olarak üretilen bu liflerin yüzey morfolojileri ve çekme testi sonrası lif uçlarının kırılma morfolojileri taramalı elektron mikroskobu (SEM) ile incelenmiştir. Üretilen GO liflerinin seçilen uygun kimyasal indirgenme metodu ile indirgenerek grafen liflerinin üretimi sağlanmıştır. Elektrik iletkenliği kazanmak için, GO indirgemesi, Hidroiyodik Asit (HI), Askorbik Asit (AA) ve Sodyum borohidrid ($NaBH_4$) kimyasalları kullanılarak gerçekleştirilmiştir. Sonuçlar, $NaBH_4$ kimyasal indirgeme işlemi, 214 $Scm^{-1}$ ile en yüksek elektrik iletkenliğine sahip grafen elyaflarını verdiğini göstermiştir. Son olarak tek aşamalı hat ile tamamlanacak şekilde oluşturulmuş ve üretilmiş multi-fonksiyonel grafen ve GO liflerinin mekanik özellikleri test edilmiştir. Sonuçlar, çekilen GO liflerinin özgül gerilme mukavemetinin 7 N/tex ve yüzde birim uzama değerinin (%) ise % 10 olduğunu ifade etmiştir. Literatürdeki çalışmalara kıyasla daha yüksek süneklik elde edilebilmiştir.

Bu tezin ikinci amacın da ise kuru eğirme yönteminin uygulanmasıyla dikey olarak hizalanmış karbon nanotüplerinden (DY-KNT) lif üretimi bulunur. KNT iplik üretimi ise öncelikle kimyasal buhar biriktirme (KBB) metoduyla kaplamalı silikon yonga üzerinde çok duvarlı karbon nanotüp (ÇDKNT) ormanını oluşturarak başlar. Bu yöntem yüksek saflıkta, büyük ölçekli üretim ve sistem prosedürünün kolay çeşitlendirilebilmesi gibi büyük avantajlar sağlar. Bu özelliklere ek olarak çekilebilir KNT ormanı formunda kaliteli üretim de yine bu üretim metodu ilemümkündür. Nano boyutlardaki bu ÇDKNT yapıların sonraki aşama için çekilebilir özellikler taşıması önemlidir. Bu aşama kaplama malzemesi, reçete parametreleri, üretim sıcaklığı ve süresi, karbon kaynağı, KNT uzunluğu gibi birçok parametreye bağlıdır ve bu parametreler bu tez kapsamında sistematik olarak incelenmiştir. Yapılan denemelerde temel olarak silikon yonga üzerine kaplama yapılan dört çeşit yonga üzerinde denemeler yapılmıştır. Bu yongalardan birincisi Fe (~ 2nm) kaplı, ikincisi $SiO_2$ (~ 300 nm), $Al_2O_3$ (~10 nm) ve Fe (~ 2nm) kaplı, üçüncüsü $Al_2O_3$ (~10 nm) ve Fe (~ 2nm) kaplı ve son olarak dördüncüsü $Al_2O_3$ (~10 nm) ve Fe (~ 6nm) kaplı yongalardır.

Tez kapsamında temel KBB protokolü üzerinden üç set deneme yapılmıştır. Buna ek olarak literatürde öne çıkan protokoller esas alınarak da deneysel çalışmalar yapılmıştır. Birinci set denemede su buharı beslenmeyen temel protokol üzerinden yukarda belirtilen üçüncü tip yonga kullanılarak çalışmalar yapılmıştır. İkinci set denemede ise aynı tip yonga kullanılarak KBB sistemine su buharının beslendiği çalışmalar yapılmıştır. Üçüncü set denemede ise dördüncü tip yonga kullanılarak çalışmalar yapılmıştır. Kullandığımız KBB sisteminde taşıyıcı gaz olarak helyum ve hidrojen, karbon kaynağı olarak ise etilen beslenmiştir. Her bir KNT dizisi boylarına ve çekilebilirliğine göre endekslenmiştir. Elyaf iplik çekimi kolaylığı dışında, D ve G tepe yoğunluğu ($I_D$ / $I_G$) Raman spektroskopisi ile incelenmiştir. KNT dizilerinin uzunluğu optik mikroskop görüntülerinden görüntü işleme ile ölçülmüştür. Ek olarak KNT lif morfolojileri SEM görüntüleri ile incelenmiştir.

KNT sentezini takip eden aşamada laboratuvar ölçeğinde kuru lif çekim hattının oluşturulması yer alır. Oluşturulan sisteme x ekseninde hareketi sağlayan motor ve büküm veren ikinci bir motor bağlanmıştır. Üretimi yapılan KNT ormanı bu konveyör bandın üstünde yer almaktadır. Sisteme bağlanan ikinci bir motor ise sivri uçlu bir

metale döndürme hareketi vererek KNT ormanından iplik çekimini sağlar. Kuru çekim hattı için en uygun KNT seçilerek üzerinde denemeler yapılmıştır. Çekim işlemi sırasında iplik çekiminin temelini oluşturan büküm üçgeni oluşumu gözlemlenmiştir. Yalnız üretilen lifler kısa boyutlarda ve düzensiz iplik morfolojisine sahiptir. Buna rağmen Z büküm verilmiş ve 40° büküm açısına sahip KNT ipliklerin üretimi gerçekleştirilmiştir.

# 1  INTRODUCTION

## 1.1  Carbon Nanomaterials

In nature, the carbon atom assemblies can be found in three allotropic forms, which are diamond, graphite and amorphous carbon. Among them, fullerene (buckyball), carbon nanotubes and graphene are called the artificial allotropes of carbon.

Linus Pauling first discovered the structure of allotropes in the 1950s. Pauling defined graphite as: 'Graphite today consists of giant molecular layers we have defined as graphene.' From this point of view, single layer of graphene can be interpreted as the building stone of all other allotropes given in Figure 1.1.
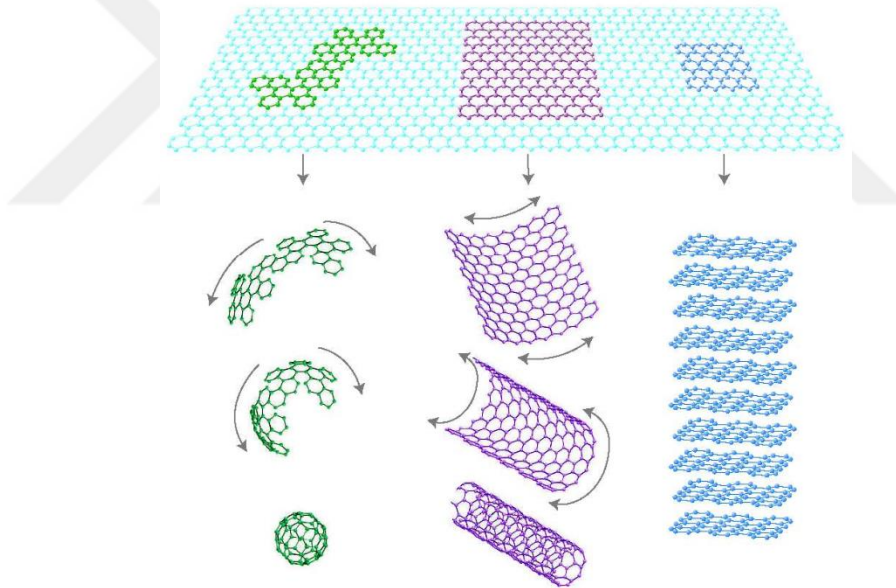


**Figure 1.1:** Schematic illustration of fullerene, CNTs, graphene and graphite nanomaterials [1]

Fullerene is a spherical molecule formed by the formed cage structure consisting 60 carbon atoms in the form of a soccer ball. H. Kroto *et al.* first discovered fullerene in 1985, in a study conducted at Rice University (U.S.A.). The discovery of this single molecule at the size of 1 nm, which was stronger in steel, lighter in plastic, electric and heat-permeable, brought him Nobel Prize for Chemistry in 1996.

Later on, S. Iijima experimentally discovered CNTs in 1991 during fullerene synthesis in Japan. CNTs are produced by dividing the $C_{60}$ molecule into halves and placing graphene sheet as body. CNTs consist honeycomb pattern of C atoms when each layer of carbon atoms is jointed, it is shaped as tubular structure. CNTs can be produced as cap open or closed, while length/diameter ratio can be increased by $10^6$ times. Their associated physical and chemical properties are changed accordingly. These structures have many excellent properties, such as low density, high strength and modulus, high electrical and thermal conductivity, stability at relatively high and low temperatures [2].

In fact, many electronic and structural features of these allotropes are derived from the properties of the graphene. Andre Geim *et al.* (2004) produced a single layer of graphene by mechanically stripping from graphite using the scotch tape method. The discovery of the graphene brought Nobel Prize in Physics in 2010 to Novoselov and Geim [1].

## 1.2    Problem Statement

Graphene and CNTs are still found to be promising carbon nanomaterials ever since they were discovered. The carbon atoms arranged in a hexagonal structure gives excellent electronic and mechanical properties to graphene and CNTs. The researchers have started to explore other macroscopic assemblies of CNTs and graphene including their fibers. Table 1.1 shows the mechanical and electrical conductivity properties of these carbon-based fibers compared to carbon fiber. Event still today, carbon fibers are more practical in large-scale applications. Transferring superior properties of CNTs and graphene to macro-scale applications has been focus of interest. Besides, carbon based fibers have been studied and developed intensively over the past few years to meet the demands in terms of flexibility and being lightweight.

The hypothesis of this thesis is that with a precise control on the production of CNTs and graphene, it would be possible to have continuous production of CNTs and graphene fibers, which exhibits superior properties of individual graphene sheets. Besides, each fiber manufacturing approach were stem from traditional fiber production methods such as wet spinning and dry spinning, and also eliminated the use of polymers and/or any binding agents. The inherent electrical properties of carbon

nanomaterials were combined with mechanical properties, which could be easily tuned by process optimization. Herein, this thesis focused on the production of flexible and strong graphene based fibers and CNTs fibers, with particular emphasis on mechanical properties. In addition, these emerging fibers, if combined with electronic systems could be used as sensors, super capacitors and light-weight cables, and also be promising candidates to power portable and flexible electronic devices. This work highlighted the structural design of spinning devices and nanomaterial synthesis with particular focus on the mechanical properties such as flexibility and strength.

**Table 1.1:** Comparison of Graphene-based fiber (GBFs), CNTs fiber and carbon fiber [3].

| Fiber | Year developed | Tensile strength [GPa] | Young's modulus [GPa] | Failure Strain | Flexible | Density [$gcm^{-3}$] | Electrical conductivity [$Scm^{-1}$] | Thermal conductivity [$Wm^{-1}K^{-1}$] |
|-------|----------------|------------------------|-----------------------|----------------|----------|----------------------|--------------------------------------|----------------------------------------|
| GBFs | 2011 | 0.1-0.5 | 10-50 | 4-10% | yes | 0.2-1.8 | $1\text{-}4 \times 10^2$ | 1435 |
| CNTs fiber | 2000 | 0.5-2 | 50-100 | 1-4% | yes | 0.2-1.3 | $10^2 \text{-} 10^3$ | 5-60 |
| Carbon fiber | 1960s | 2-7 | 200-820 | <2% | no | 1.75-2 | $10^2 \text{-} 10^4$ | ca. 500 |

## 2 LITERATURE REVIEW

### 2.1 Graphene

In 1930, Landau and Peierls described the formation of graphene by referring to thermodynamic governing laws that show the possibility of two-dimensional structures. In 1947, P. Wallace calculated the electronic band structure of graphite. Later, in 1957 Linus Pauling shed light on the electronic structure and properties of the individual graphene sheets. Until 1980, carbon was thought to be seen as of only 3 basic forms (diamond, graphite, amorphous carbon). After the discovery of fullerene and CNTs, in 2004, graphene was experimentally detected as a proof of high-quality 2-dimensional orders. In addition, Novoselov and Geim *et al.* have synthesized a single layer of graphene and have observed a range of electronic and physical properties [2].

#### 2.1.1 Graphene fundamentals and applications

The presence of graphene as in the form of 2D crystal was detected by using a simple principle proposed by Novelsov and Geim *et al.* [2]. After that, graphene became quite popular in nanomaterial world. Graphene exhibited tensile strength of 130 GPa and , elasticity modulus of 1.1 TPa and electrical conductivity of $\sim 108$ S/m [4].

Among diverse applications of graphene, the main uses could be listed as transparent conductive electrodes, reinforcement in composite materials fuel cells, integrated circuit components, catalyst support materials, thermal conductors, lithium-ion batteries and supercapacitors. Besides that, fibrous assembly of these structures provide lightweight, flexibility and better resistance particularly to cyclic loadings. Several examples of graphene fiber applications are shown in Figure 2.1.
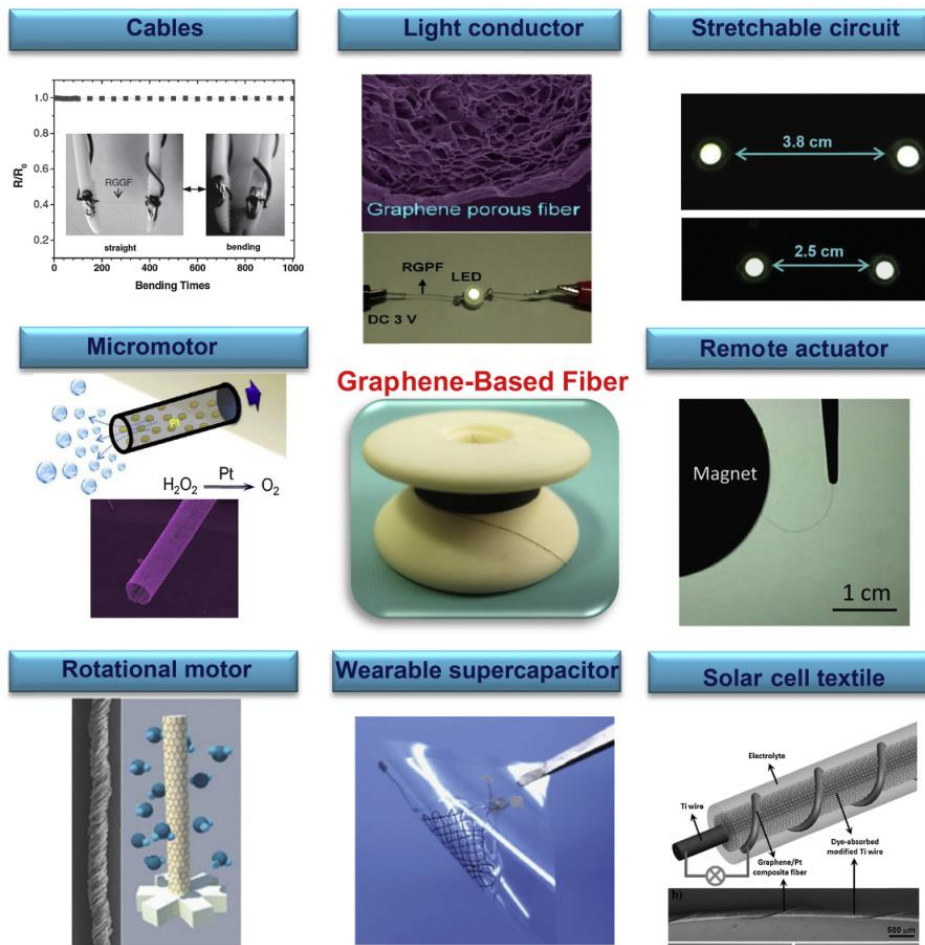
**Figure 2.1:** Examples of application areas of graphene-based fiber [4].

### 2.1.2 Chemical Structure

Graphene, graphite, CNTs and fullerenes, all have carbon fiber honeycomb structures with $sp^2$ hybridization, whereas diamonds are considered in a different category due to $sp^3$ hybridization and its quadrilateral mesh. Graphene is one of the examples of two-dimensional planar structures [5]. Carbon atoms are $sp^2$ hybridized at 120 degrees with the combination of 1s and 2p orbitals. The idle 2 $P_z$ orbitals form the pi bond in the graphene. The carbon-carbon bond distance in the graphene structure is approximately 1.42 Angstrom. This distance is slightly shorter than the C-C single bond (1.54 Å) and slightly longer than the C=C double bond (1.33 Å). The distance between carbon atoms in honeycomb structure shown as in Figure 2.2a and single-layered graphene sheet made of this structure are given in Figure 2.2b.[3]
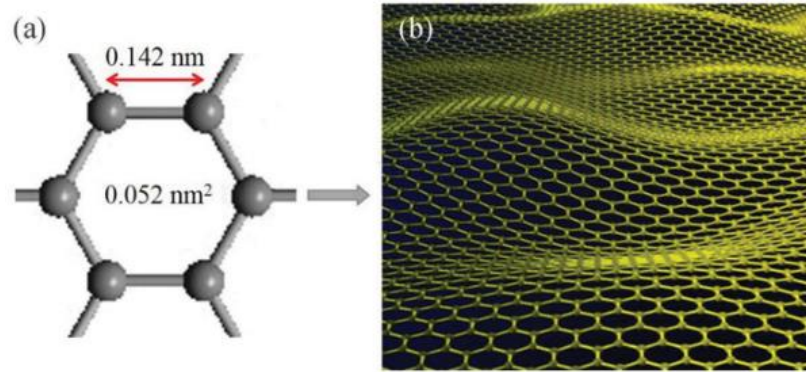
**Figure 2.2:** a) Schematic diagram of graphene and b) graphene sheet illustration [3].

### 2.1.3 Graphene synthesis methods

There are many methods proposed for the synthesis of graphene. Figure 2.3 shows these methods as categorized in two main approaches such as top-down and bottom up. Top-down approach produces graphene by separating the structure of graphite until the final form graphene. While bottom-up approach builds graphene from individual carbon atoms and blocks. So far, the most commonly used methods are mechanical exfoliation, chemical exfoliation, chemical synthesis and CVD method [6].
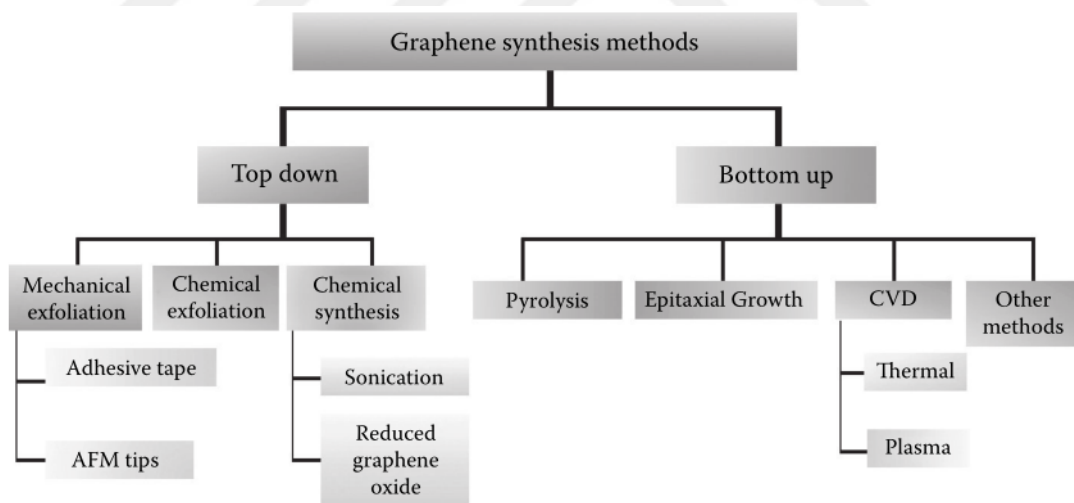


**Figure 2.3:** Graphene synthesis methods [6].

### 2.1.3.1 Exfoliation

The graphite is formed of stacked graphene sheets which are connected to each other by Van der Waals forces. Hence, pure graphene can be obtained by the separation of these weak bonding in graphite. Mechanical, thermal or chemical energies can be used to break these weak bonds.

In 2003, Viculis *et al.* mixed graphite and potassium in a stochastic ratio, which was treated at 200 °C in an inert atmosphere. The materials of potassium atoms between the graphene layers were synthesized. The synthesized material was put into ethanol. It was observed that the graphene sheets were separated from each other by the reaction between potash and ethanol. They produced graphene nanoscrolls as shown in Figure 2.4 after sonication [7].
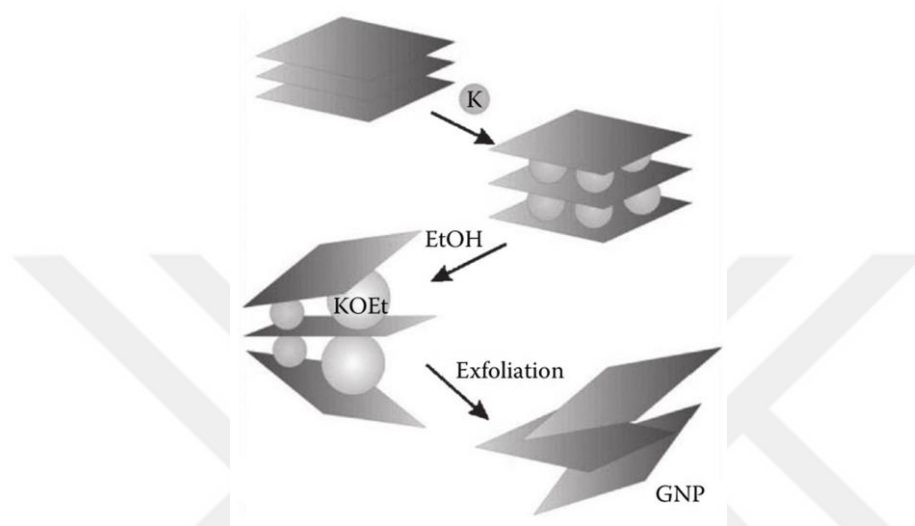


**Figure 2.4:** Graphene nanosheet production process as proposed by Viculis *et al.* [7].

Novoselev *et al.* used mechanical exfoliation method by using adhesive tape on graphite. Stacked graphene sheets are separated stepwise. Finally, they have succeeded in producing graphene at a few atoms thick [2]. With this method, it was also possible to produce graphene sheets with larger surface area and high quality of several atomic grains, whereas it did not allow large scale production. Moreover, the width and thickness of each layer could not be precisely controlled. [6].

### 2.1.3.2 Chemical synthesis

Chemical synthesis is another prominent method for the production of high amount of graphene. Firstly, GO layers are produced by chemical oxidation process from graphite. GO is a single layer of graphite sheets separated from each other by oxidation. C:O ratio which is changed by the presence of functional groups is typically three or less. GO structure can be shown in Figure 2.5. Consecutively, GO is reduced by various methods and reduced graphene can be achieved [6].
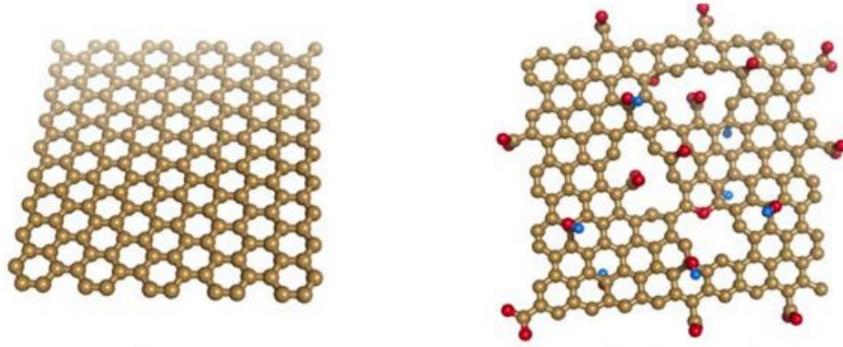
**Figure 2.5:** Schematic diagram of graphene (left) and GO (right) [8].

This method has two main advantages. First, it enables efficient production due to the use of cheap graphite raw material. Secondly, aqueous stabilized solutions can be prepared since GO has hydrophilic nature.

In 1958, Hummers and Offeman developed an approach to oxidize graphite, where today most of the chemical exfoliation methods stem from this approach. Potassium permanganate ($KMnO_4$) and concentrated sulfuric acid ($H_2SO_4$) were used for oxidation. Then subsequent reduction was followed to achieve the reduction of GO sheets. The process steps are also given in Figure 2.6. In 2013, Chen *et al*. unveiled the improved Hummers' Method, which consumed sulfuric acid / phosphoric acid mixture as more eco- friendly approach instead of using concentrated sulfuric acid [8].
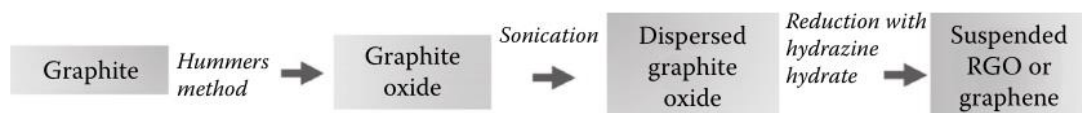


**Figure 2.6:** Process flow chart of graphene synthesis from graphite [6].

### 2.1.3.3 Epitaxial growth

The growth of graphene on silicon carbide (SiC) known as epitaxial growth requires heating up to temperatures 1150 and 2000 °C, depending on the growth conditions. The heating resulted in desorption of silicon atoms and the remaining carbon atoms epitaxially come together to form graphene sheet (Figure 2.7). Since the carbon source is the SiC layer, new layers are formed on top of first layer and multi-layered graphenes could be obtained. The number of graphene layers strongly depends on the thickness of SiC layer. However, the system is quite limited. After the first formed graphene layer, the desorbed Si atoms do not find escape routes and cannot get away from the stratum, which leads to the termination and the end of the growth [8].
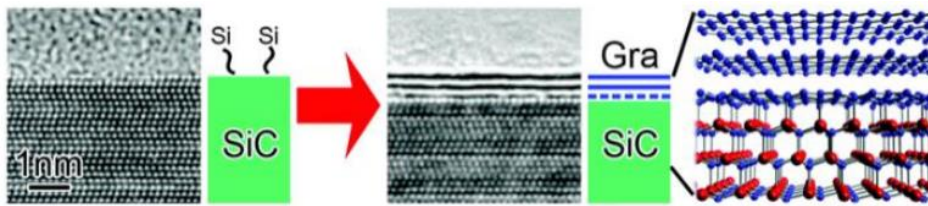
**Figure 2.7:** Schematic representation of the epitaxial graft enlargement method [8].

### 2.1.3.4 Chemical vapor deposition (CVD)

Thermal chemical vapor deposition (th-CVD) which is carried out by subjecting a substrate to thermal decomposition and depositing the product onto the substrate at high temperature can be used to produce graphene. The th-CVD chamber for graphene synthesis is shown in Figure 2.8a. Th-CVD has many advantages includes high quality and high purity of graphene. In addition, the system also allows large-scale production. On the other hand, th-CVD process has many variables, which may affect the morphology, crystallinity, shape and size. A wide range of nanomaterials and thin films can be produced using this process [6].

The plasma-enhanced chemical vapor deposition (PECVD) process works based on formed plasma in vacuum chamber, leading thin film deposition on the substrate surface. The PECVD chamber for graphene synthesis are shown in Figure 2.8b. Plasma state can be formed in PECVD system using RF, microwave and inductive coupling. PECVD has several advantages over th-CVD method such as reduced, process temperature and ease in industrial scale production. Furthermore, by controlling the process parameters and the catalyst-free growth of the graphene, the properties of the final graphene product can be tuned. However, this process is quite expensive and only gas phase materials can be consumed, limits the synthesis of industrial products [6].
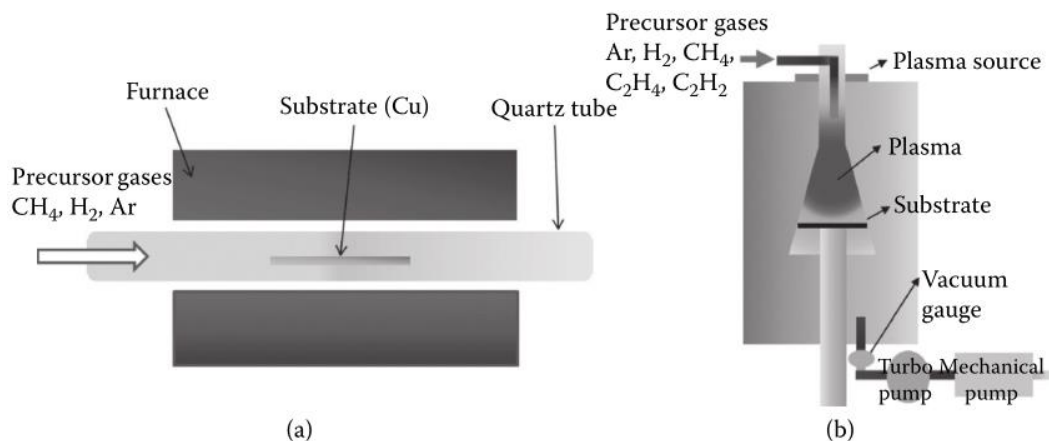
**Figure 2.8:** Schematic diagram of (a) th-CVD and (b) PECVD methods [6].

### 2.1.3.5 Pyrolysis of sodium ethoxide

There is one of the bottom up approach, is also called the solvothermal method. In this method, ethanol and sodium are used as the starting material in sodium ethoxide synthesis. Followed by pyrolysis, easily dispersed graphene sheets are produced by soft sonication. The resulting solid was sequentially pyrolysed, vacuum filtered and dried in a vacuum oven at 100 °C for 24 hours. The advantage of this process is that neat and functionalized graphene can be produced in a controlled manner. In addition, it is cost-effective, scalable, low-temperature process. However, the quality of graphene is still unsatisfactory due to inevitable defects.

### 2.1.4 GO Reduction methods

GO reduction term describes the transformation of solely carbon-containing form within the decomposition of oxygen-containing groups. GO basically can be reduced by four methods. These methods are thermal reduction, chemical reduction, microwave irradiation and flash reduction.

### 2.1.4.1 Thermal reduction

The GO-layer precipitates under heating at 220-230 °C during dry bending, which is essentially solvothermal process where the water is used as the solvent in the GO dispersion. For instance, the fibers reduced by this method, referred as reduced GO (rGO) fibers. 27% of the oxygen can be removed from GO at 180 °C. Most of the hydroxyl, epoxy and carboxyl groups start to separate at 200 °C [9, 10].

Thermal annealing is an effective method for the reduction of GO. However, there are several disadvantages such as high energy and production costs due to the operation at high temperature. Associated to high process temperature, GO layers can be damaged [8].

**Table 2.1:** The effect of different reduction methods on GO structure [11].

| Ref. | Reduction method | Form | C/O ratio | $\sigma$ (S/cm) |
|------|------------------|------|-----------|-----------------|
| [12] | Hydrazine hydrate | Powder | 10.3 | 2 |
| [13] | Hydrazine reduction in colloid state | Film | NA | 72 |
| [14] | 150 mM NaBH$_4$ solution, 2 h | TCF | 8.6 | 0.045 |
| [15] | Hydrazine vapor | Film | ~8.8 | NG |
|  | Thermal annealing at 900 °C, UHV |  | ~14.1 | NG |
| [16] | Thermal annealing at 1100 °C, UHV | TCF | NA | ~$10^3$ |
| [17] | Thermal annealing at 1100 °C in Ar/H$_2$ | TCF | NA | 727 |
| [18] | Multi-step treatment: |  |  |  |
|  | (I) NaBH$_4$ solution | Powder | (I) 4.78 | (I) 0.823 |
|  | (II) Concentrated H$_2$SO$_4$ 180 °C, 12 h |  | (II) 8.57 | (II) 16.6 |
|  | (III) Thermal annealing at 1100 °C in Ar/H$_2$ |  | (III) >246 | (III) 202 |
| [19] | Vitamin C | Film | 12.5 | 77 |
|  | Hydrazine monohydrate |  | 12.5 | 99.6 |
|  | Pyrogallol |  | NA | 4.8 |
|  | KOH |  | NA | $1.9 \times 10^{-3}$ |
| [20] | 55% HI reduction | Film | >14.9 | 298 |

\* UHV: ultra-high vacuum.
\*\* NA: not available.

### 2.1.4.2 Chemical reduction

Many reducing agents can be used to reduce GO sheets, among them, The most common reduction agents in literature are hydrazine, borohydrides, aluminium hydrides, reducing agents containing sulphur, and more environmentally friendly approaches such as ascorbic acid [8]. Through the reduction of GO, graphene oxide changes its brown color to gray due to the removal of oxygen-containing groups. In other words, the change in the solution color, also pointed out the reduction of the oxygen ratio and the increase of the conductivity.

Table 2.1 summarizes the prominent reports in the literature on the reduction of GO. The electrical conductivity and the C/O ratio of the GO in different forms are addressed [11].

### 2.1.4.3   Microwave irradiation

Microwave-assisted reduction enables reduction with uniform and rapid heating effect. The reduction was conducted in a microwave oven for 1 minute in room conditions [21].

### 2.1.4.4   Flash reduction

Flash reduction has been widely used for GO filament reduction. The GO's laser reduction process is actually a thermal reduction. A laser beam focused on the top surface of the GO fiber is shown in Figure 2.9. The irradiated region is heated to temperature higher than 500 °C by laser source. Due to non-uniform thickness, the reduction efficiency is much lower than the chemical and thermal reduction methods. However, the prominent feature of the laser reduction process is the realization of area selective reduction, which is quite unique for production of functional graphene fibers and actuators [22, 23].
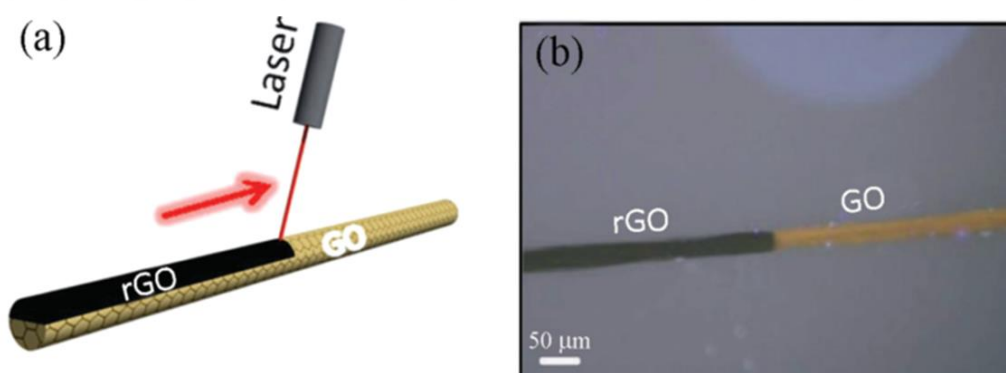


**Figure 2.9:** a) GO filament reduced by laser scanning the upper surface of the GO lane. b) Digital photograph of a graphene /GO asymmetric fiber produced by laser reduction [22].

### 2.1.5   Production of graphene fibers

Due to thermal stability and high melting temperature around 4900K, melt spinning method cannot be used to produce graphene fibers. There have been three different methods widely used for graphene fiber production, which are dry spinning, dry-jet wet spinning and wet spinning.

### 2.1.5.1 Dry spinning

In this method, the graphene material as in the form of GO dispersion was used. Mostly GO was dispersed in water and this GO spinning fluid was injected into a tube and sealed. Then chemical reduction or heating was applied at high temperature. Gel-form GO converted into the fibers by drawing and twisting. GO layers precipitated during heating at 220-230 °C through dry bending. The fibers produced by this method were called reduced GO fibers, while thermal reduction were occurred simultanously. Some amount of oxygen presence in the GO could be removed at 180 °C. Hydroxyl, epoxy and carboxyl groups started to separate at 200 °C. Hence, graphene fibers synthesized by the hydrothermal process had the electrical conductivity about 10 S cm$^{-1}$. After drying, around 80-95 % reduction in fiber diameter was observed due to the loss of water accumulated on the fiber caused fiber shrinkage [9, 10, 24, 25].

### 2.1.5.2 Dry-jet wet spinning

In this method, GO/Chlorosulfonic acid solution was used as the liquid crystal dispersion. This solution was injected into diethyl ether to coagulate GO fiber. The air gap between the injector and the bathroom level was intentionally kept for better mechanical properties. This distance was 12 cm, and reduced the velocity gradient between the injector and GO thread. Gravitational forces were apparent for stretching and was thought to improve fiber alignment. Next, thermal annealing followed to reduce GO fiber. Dry jet wet-bending method produced smooth GBFs with circular cross section. These produced fibers and the production setup are shown in Figure 2.10 [3].
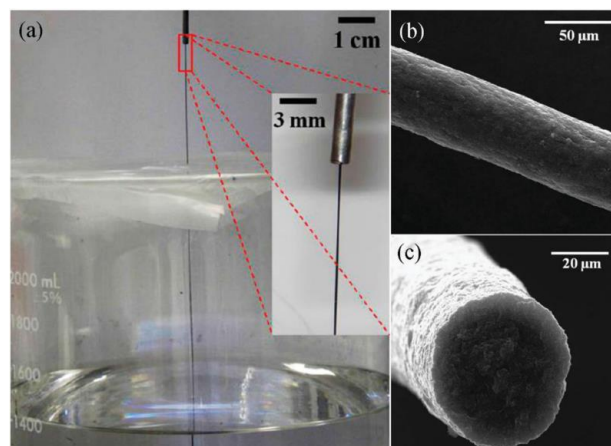


**Figure 2.10:** (a) Set-up photograph for dry-jet wet-spinning of GO fiber, (b and c) Smooth surface and nearly circular cross-section images of GO fiber [3]

### 2.1.5.3 Wet spinning

In wet spinning method, the GO sheets were dispersed in aqueous solution, and then was injected into the coagulation bath to form the fiber while keeping in the coagulation bath for a while. Then GO-fiber in this gel state was dried. In order to form the GO fibers smoothly and continuously, a certain speed of movement must be given by rotating the coagulation bath or pulling it with the collection unit [3].
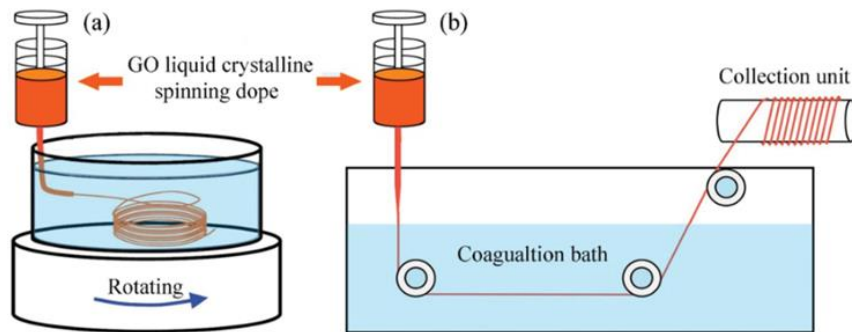


**Figure 2.11:** Schematic illustrations displaying graphene fiber production of wet spinning set-ups a) by rotating coagulation bath and b) by collection unit [26]

Figure 2.11 shows that proposed two types set-up with a rotating coagulation bath and a collection unit for graphene wet spinning method. Although stronger reduced GO fibers were manufactured by the first collecting approach (Figure 2.11a), which were subjected to slight bending Nevertheless, this method was not convenient for precise control of fiber movement. It was seen that the frictional forces between the fiber surface and the coagulation was interrelated, whereas it was not proportional to the movement speed and bath rotation speed. The proposed second system (Figure 2.11b) was developed considering the shortcomings of the first system. A constant pulling force was applied and the fiber was pulled at a certain speed of movement. At this stage, the scalable fiber production can be done with optimum draw ratio [26].

Table 2.2 summarizes studies used these three spinning methods. Table 2.2 also addresses structural properties of fiber, mechanical properties in terms of Tensile strength, Young's modulus and Failure strain and electrical conductivity. Among all methods, wet-spinning approach provided the most convenient mechanical performance for GO fibers.

**Table 2.2:** Mechanical and physical properties of developed graphene based fibers [3].

| Spinning Technique | Ref. | GO Diameter [µm] | Fiber Composition | Fiber Diameter [µm] | Tensile Strength [MPa] | Young's Modulus [GPa] | Failure Strain [%] | Electrical Conductivity [Scm$^{-1}$] |
|---|---|---|---|---|---|---|---|---|
| **Wet-spinning** | | | | | | | | |
| | [27] | 0.91 | GO | 50–100 | 102 | 5.4 | 6.8–10.1 | – |
| 5% NaOH/methanol bath, HI reduced | | | rGO | – | 104 | 7.7 | 5.8 | 250 |
| 5% CaCl$_2$ /H$_2$O bath, HI reduced | [26] | 18.5 | GO | ≥6 | 364.4 | 6.3 | 6.4 | – |
| | | | rGO | – | 501.5 | 11.2 | 6.7 | 410 |
| Ethyl acetate bath, HI reduced | [28] | 22.6 | rGO | – | 360 | – | 10 | 280 |
| | | | rGO/Ag | 10 | 305 | – | 5.5 | 910~930 |
| 0.05% CTAB/H O bath, HI reduced | [29] | – | GO | 53 | 145 | 4.2 | – | – |
| | | | rGO | 43 | 182 | 8.7 | – | 35 |
| | [30] | 9 | GO | – | 214 ± 38 | 47 ± 8.1 | 0.61 ± 0.1 | – |
| Ethyl acetate bath, 1000 °C annealed | | | rGO | ca. 26 | – | – | – | 294 |
| 1% chitosan bath | [31] | 37 | GO | – | 442 ± 18 | 22.6 ± 1.9 | 3.6 ± 0.7 | – |
| 1 M NaOH bath 220 °C | | | rGO | – | 115 ± 19 | 9 ± 2.1 | – | 2.8 |
| Ethanol bath, HI reduced | [32] | – | rGO | – | 238 | – | 2.2 | 308 |
| 0.4% CTAB/H O bath, HI reduced | [33] | 30 | GO | – | 267 | 14 | – | – |
| | | | rGO | – | 365 | 21 | – | 270 |
| Liquid nitrogen bath, HI reduced | [34] | – | GO | – | 6.9 | 0.27 | 4.6 | – |
| | | | rGO | – | 11.1 | 0.35 | 6.2 | 20 |
| Methanol bath | [35] | – | GO/PAN | ca. 25 | 452 | 8.31 | 5.44 | – |
| 5% CaCl $_2$ /H$_2$O bath, HI reduced | [36] | – | GO/HPG | – | 555 | 15.9 | 5.6 | – |
| | | | rGO/HPG | – | 443 | 10.8 | 5.6 | 32.09 |
| 5% CaCl$_2$/H$_2$O bath, HI reduced | [37] | – | GO/GMA | 15 | 500 | 18.8 | – | – |
| | | | rGO/GMA | – | – | – | – | 1.86 |
| **Dry spinning** | | | | | | | | |
| Glass pipeline, 230 °C/2 h | [25] | – | rGO | ca. 33 | 180 | – | 4.2 | ca. 10 |
| Glass pipeline, 230 °C/2 h | [38] | – | rGO | >30 | ca. 156 | – | 2.1 | 10–20 |
| Glass pipeline, 230 °C/2 h, grow CNTs | [39] | – | rGO/CNTs | ca.100 | 24.5 | – | – | ca. 12 |
| Glass pipeline, 230 °C/2 h | [40] | – | rGO | 30–35 | – | – | – | ca. 10 |
| Silica capillary column, 220 °C/6 h | [24] | – | rGO | 40 ± 2 | 197 | – | 4.2 | 12 |
| | | | rGO/CNTs | 60 ± 3 | 84 | – | 3.3 | 102 |
| PP tube, VC reduced 80 °C/6 h | [41] | – | rGO | ca. 200 | 150 | ca. 1.9 | ca. 20 | ca. 8 |
| **Dry-jet wet-spinning** | | | | | | | | |
| Dry-jet wet-spinning, 1050 °C annealed | [42] | 0.71 | GO | 54 | 33.2 | 3.2 | 1.64 | – |
| | | | rGO | 29.5 ± 0.6 | 383 | 39.9 | 0.97 | 285 |

## 2.2 Carbon Nanotube (CNTs)

### 2.2.1 CNTs fundamentals and applications

CNTs with seamless hollow cylindrical structure consist carbon hexagons. There two general types of CNTs: single-wall carbon nanotubes (SWCNTs) and multi-wall carbon nanotubes (MWCNTs) consisting of several coaxial cylinders [43].

In the 1970s, the synthesis of carbon fibers was conducted by the vapor deposition method, which was prepared by lysis of benzene in the presence of Fe catalyst particles at 1100 °C. In one of the first detailed systematic study in carbon assemblies, took place in 1991 by Iijima. The presence of CNTs were noted by high-resolution transmission electron microscopy (HRTEM) images [44].

CNTs have excellent mechanical, electrical and thermal properties, in addition to being lightweight. Hence, they offered various application starting from small electronic devices to large load bearing structural components. CNTs-related trade volume has grown significantly in the last decade. Since 2006, the worldwide production capacity of CNTs have increased at least 10 times. In addition, as shown in Figure 2.12 the annual number of CNTs-related journal publications and published patents has been increasing [45].
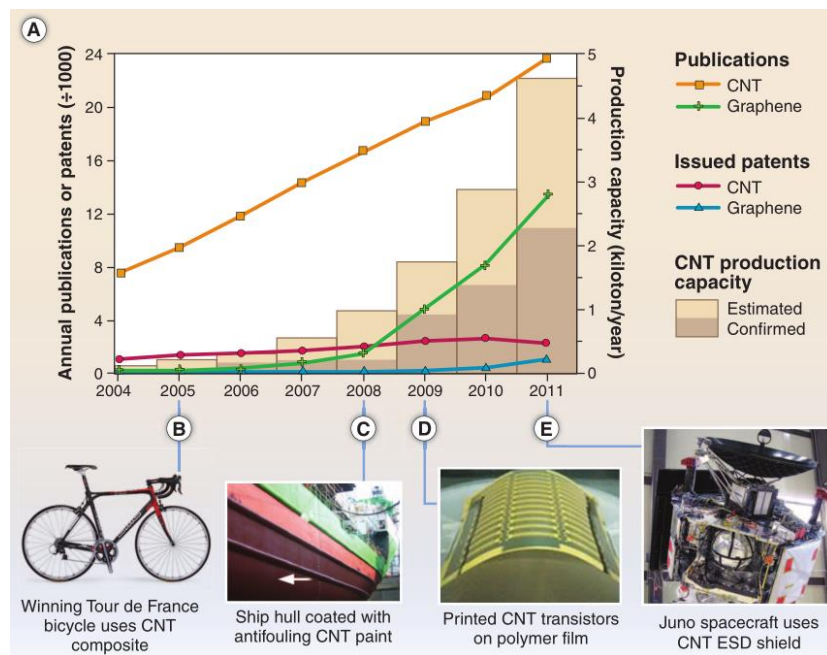


**Figure 2.12:** Publications, published patents and production capacities of CNTs and graphene, b to e) several products of CNTs related materials [45]

## 2.2.2   Chemical structure

In CNTs, there are four electrons in the outer valence shell of carbon; the ground state configuration is $2s^2 2p^2$. The graphene sheet which is 2-dimensional hexagonal (honeycomb) lattice of the $sp^2$ group, are rolled to form CNTs [5].

CNTs are considered as almost one-dimensional due to their high length/diameter ratio. The atomic order, the diameter and length of the tubes and their morphology determine the physical and electrical properties of CNTs. As shown in Figure 2.13, CNTs are classified as a single walled (SW-), double walled (DW-) and multiple walled (MW-) CNTs according to the number of walls. SWCNTs are single cylinder with only one rolled graphene sheet while MWCNTs have more than one concentrically rolled graphene sheets [46]. The diameter of MWCNTs are ranged from 1.4 to 100 nm, while the diameter of SWCNTs are in the range of 0.4 to 3 nm [43]. The distance between layers in MWCNTs varies from 0.34 to 0.39 nm [47].
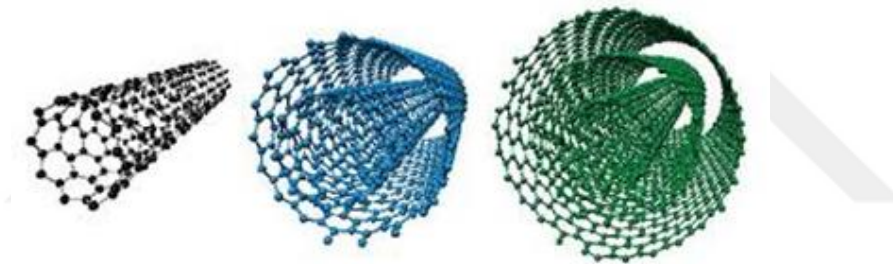


**Figure 2.13:** SWCNTs, DWCNTs and MWCNTs [48]

SWCNTs can be also categorized according to the diameter and the chirality angle of the bending angle respect to the normal axis. These are called as armchair, zigzag and intermediate. Figure 2.14 shows the chirality angle and the associated three different CNTs types. The chiral angle plays an important role in the electrical conductivity. When CNTs in the form of zigzags and intermediates exhibit semi-conductor behavior, while the ones in the armchair have metallic characteristic with higher electrical conductivity [43].
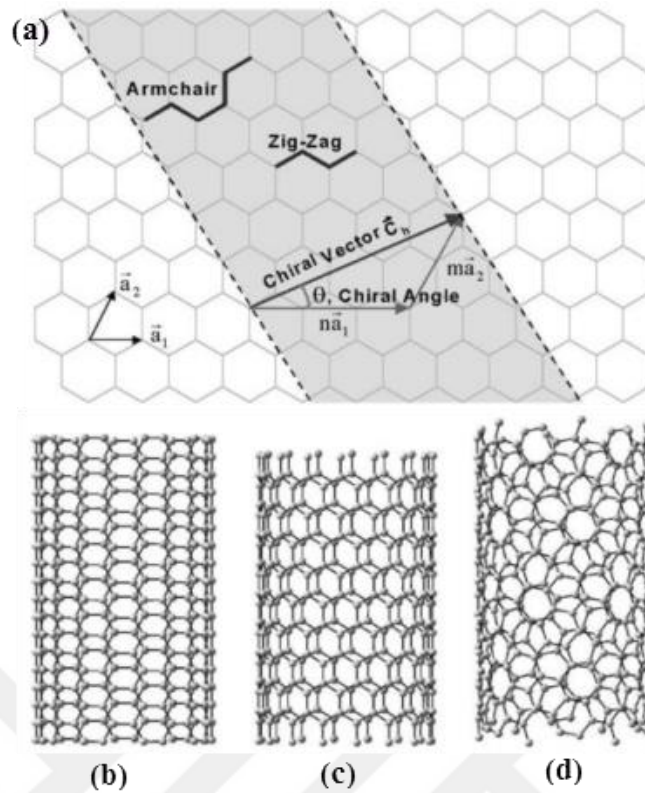
**Figure 2.14:** (a) A schematic diagram showing the directionality how the graphene material was rolled while forming CNTs [46]. (b) armchair tube, (c) zigzag tube, (d) chiral tube [49].

### 2.2.3 Synthesis methods of CNTs

CNTs can be synthesized by a variety of methods and most of the time they involve gas phase processes. There are three commonly used techniques for CNTs growth:

- Arc discharge
- Laser ablation
- Chemical vapor deposition (CVD) [47]

### 2.2.3.1 Arc-discharge

The arc discharge method for synthesis of CNTs were first proposed by Iijima, and at the end MWCNTs were achieved. Afterwards, SWCNTs synthesis also had been succeeded by arc-discharge method [44, 50]. Arc discharge method is one of the most widely used CNTs production methods today also was approved as the first method developed for CNTs synthesis [51].

The arc-discharge method relied on the application of electrical current to the graphite electrodes in an inert gas environment and the evaporation of the C atoms by arc

formation between the electrodes. Inert gases such as argon and helium were used. Electrodes applied with a low voltage (10 - 25 V) and high current (50 - 120 A) were kept at 1-2 mm distance to each other and arc formation was enabled [52]. The anode graphite, which sublimed at high temperature, was condensed in the cold reactor wall. There were fullerenes and/or CNTs depending on the experimental parameters applied in these particles rising with smoke. Part of the anode electrode formed precipitates on the cathode and these precipitates consisted high amount of MWCNTs. Transition metal catalysts such as iron, nickel and cobalt were needed to synthesize SWCNTs by argon discharge [44, 50, 53].

The crystal structures of CNTs were almost defect free due to high temperature up to 5000 K in the arc discharge method One of the disadvantages of this method is intermittent run of process where the system must be shut down after the electrodes were consumed. Even in this approach, selective directionality was not under control. Thus, it required additional purification process which increased the cost [52].

### 2.2.3.2 Laser ablation

This method proposed by Smalley *et al.* has similarities with arc discharge method. In this system, reactors were placed in heated furnace at 1000-1200 °C. Inside the reactor, graphite was put as a carbon source. The catalyst mixture was required as in the arc discharge system for SWCNTs synthesis. Laser waves were sent to the graphite resulted in breakages. These removed pieces evaporated in the reaction zone, which was heated to the temperature of 5000-10000 K by aid of laser beam. Then, when they were reacted with the catalyst, CNTs were formed. Carrier gases were inert helium (He) and nitrogen ($N_2$) gases as in arc discharge system. Finally, formed CNTs in the reaction zone were collapsed with the carrier gases in the relatively cold furnace walls or in the refrigerated sample collectors [52].

### 2.2.3.3 Chemical vapor deposition (CVD)

Thermal decomposition of hydrocarbon vapor in the presence of metal catalyst is the governing mechanism in CVD system. In this process, the hydrocarbon vapor was passed through a tubular reactor while the catalyst material broke down to hydrocarbon atoms at high temperature. This process took around 15-60 minutes. In the first step, decomposition of hydrocarbon vapor led to carbon and hydrogen derivatives when contacted with hot metal nanoparticles. Hydrogen residues evaporated and carbon

atoms settled on the metal surface. In the second step, the free carbon atoms precipitated at same temperature of carbon atoms in the metal catalyst, and crystallized in the form of cylindrical web. The cylindrical web was energetically balanced, as there were no dangling bonds. Hydrocarbon decomposition caused metal exposure, while the carbon crystallization absorbed some heat from the precipitated metal. Hence, it preserved the thermal balance within the metal particle [54]. Figure 2.15 shows the schematic of a simple CVD system.
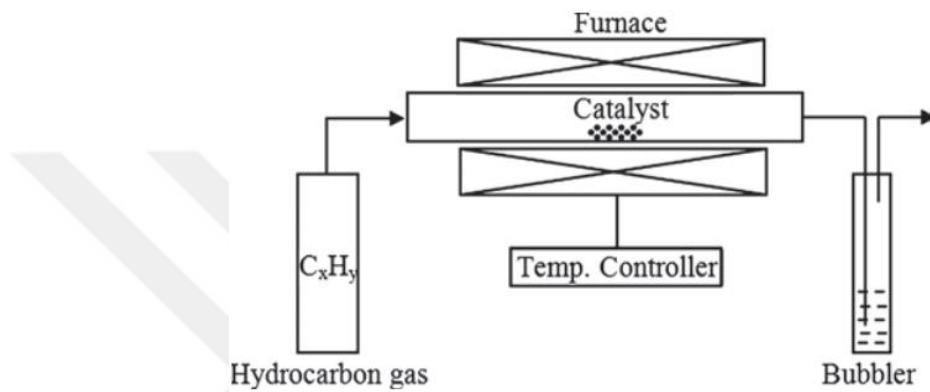


**Figure 2.15:** Schematic diagram of simplest CVD system [54]

There are two different principles for the CVD process; (i) the tip growth and (ii) the base growth (Figure 2.16). In the tip growth model, the catalyst-substrate interaction was weak and decomposed on the surface of hydrocarbon metal. The carbon was spread down from the metal and CNTs separated the metal particles from the undercoat and collapsed under metal. CNTs continued to grow until it was covered with carbon in excess of metal. Growth ceased when the catalytic metal activity terminated. In the base growth model, the catalyst-substrate interaction was stronger. For this reason, the CNTs precipitates could not elevate the metal particle. The first hydrocarbon caused decomposition and carbon diffusion, which was forced out of the metal apex. The first carbon crystallized in a semi-spherical state and began to extend in a cylindrical form [54].
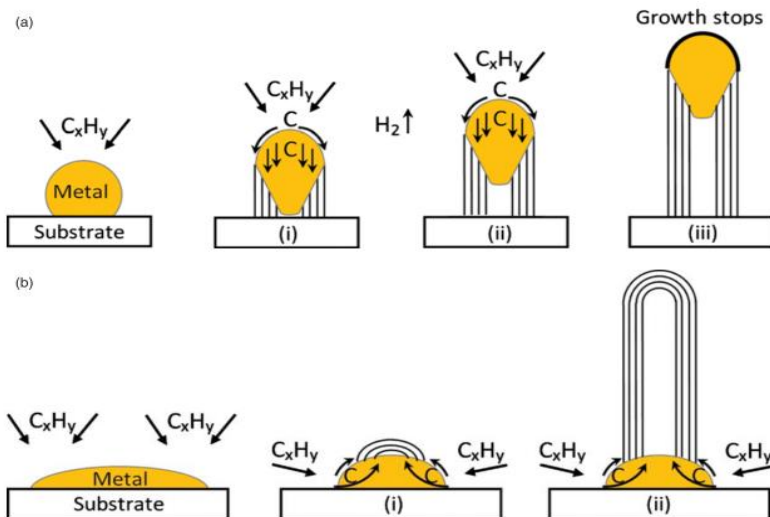
**Figure 2.16:** (a) Tip growth model, (b) Base growth model [54]

The diameter of CNTs are strongly dependent on the diameter of the metal nanoparticles. Large diameter CNTs can be synthesized in large metal nanoparticles while small diameter CNTs are produced by small-sized metal catalysts (Figure 2.17) [55]. In addition, the size of the catalyst particles also determined the number of CNTs walls. For example, SWCNTs are grown when the particle size is just a few nm, whereas MWCNTs are produced when the particle size is much larger [54]. Table.2.3 gives the summary and comparison of most common CNTs synthesis methods, which also shows the superior properties of CVD grown CNTs.
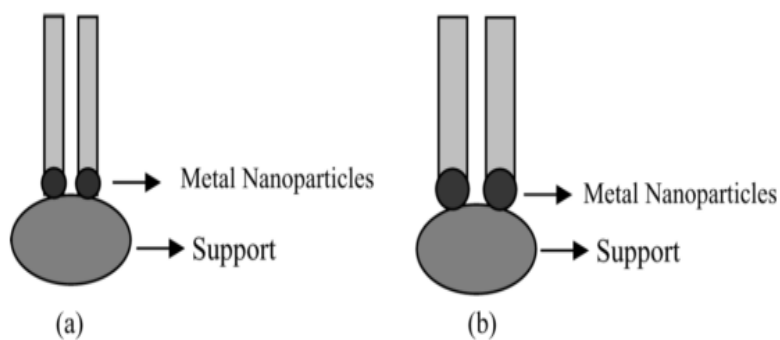


**Figure 2.17:** a) CNTs growth on small metal nanoparticles, b) CNTs growth on large metal nanoparticles [55]

22

**Table 2.3:** Summary and comparison of CNTs synthesis methods [47]

| Method | Arc discharge | Laser ablation | CVD |
|---|---|---|---|
| Yield rate | >75% | >75% | >75% |
| SWCNTs or MWCNTs | Both | Both | Both |
| Operating Temperature | > 3000ºC | > 3000ºC | < 1200ºC |
| Advantage | Simple, inexpensive, high-quality nanotubes | Relatively high purity | Simple, low temperature, high purity, large-scale production, aligned growth |
| Disadvantage | Purification required, tangled nanotubes | Method limited to the lab scale, purification required | Synthesized CNTs are usually MWCNTs |

### 2.2.4 Spinning of CNTs fibers

CNTs have high aspect ratio and specific surface area, which is an important factor also for yarn formation. In addition, they have offered a wide range of applications due to its properties such as high tensile strength, low density, high elastic modulus, high electrical and thermal conductivity [56]. Bulk synthesis with high purity and uniform diameter distribution is still challenging in CNTs synthesis. Spinning of CNTs based yarns is another issue that required attention. There are basically three approved methodologies today; these are wet spinning, direct spinning and dry spinning. Due to their simplicity and easiness in control of yarn characteristics, these methods has been widely preferred. [57].

### 2.2.4.1 Wet spinning

CNTs yarn production without using any surfactant and binding polymer was first reported by Smalley *et al*. at Rice University in 2004. In this study, 8% wt. SWCNTs were dispersed in 102% sulfuric acid. The solution was placed in stainless steel syringes and pressed by piston. The fiber with diameter ~ 125μm was wound on a Teflon cylinder. A schematic diagram of the production method was given in Figure 2.18. Process temperature, coagulants (diethyl ether, 5% aqueous sulfuric acid or water) and coagulation bath temperature (0 °C and 100 °C) were changed and system was optimized. Then the fibers were dried in the oven at 100 ºC and were annealed at 1100 °C in $H_2$/He atmosphere [58].
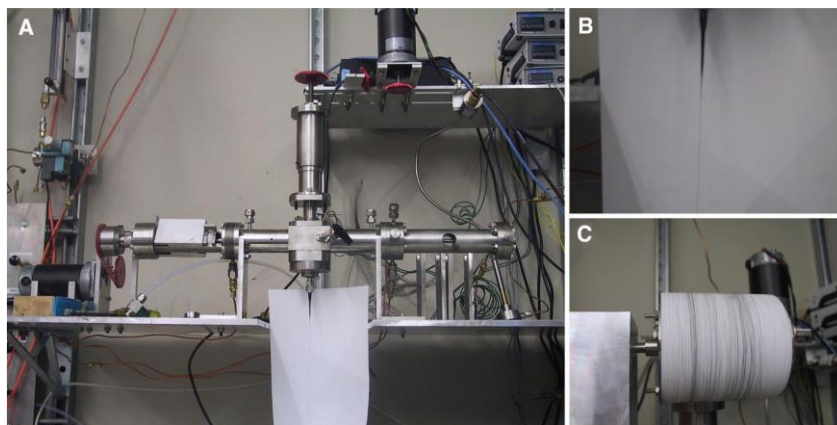
**Figure 2.18:** a) SWCNTs fiber production line, b) spinneret and CNTs fiber, c) CNTs collected on Teflon cylinder [58]

### 2.2.4.2 Direct spinning by CVD

In the wet spinning method, CNTs were exposed to strong acids for a long time, which caused protonation. Apart form this, ununiformed orientation of CNTs and coagulation problems have raised in wet spinning, which also limits the large-scale production. Furthermore, due to the use of strong acid, the method is harmful to health and the environment.

Hence, researchers have focused on yarn spinning from CNTs production without using any acid or similar agents. In direct spinning, CNTs production took place in vertical tube and carbon source (hexane, ethanol), catalysis source (ferrocene), sulfur (thiophene) for increased efficiency and $H_2$ gas were all sent through this tube. Water tank underneath the tube was placed to densify CNTs to form yarn. Then, collected yarns were washed in an acetone bath and resized and dried at about 100 °C. A schematic diagram of direct spinning production method is given in Figure 2.19 [56].
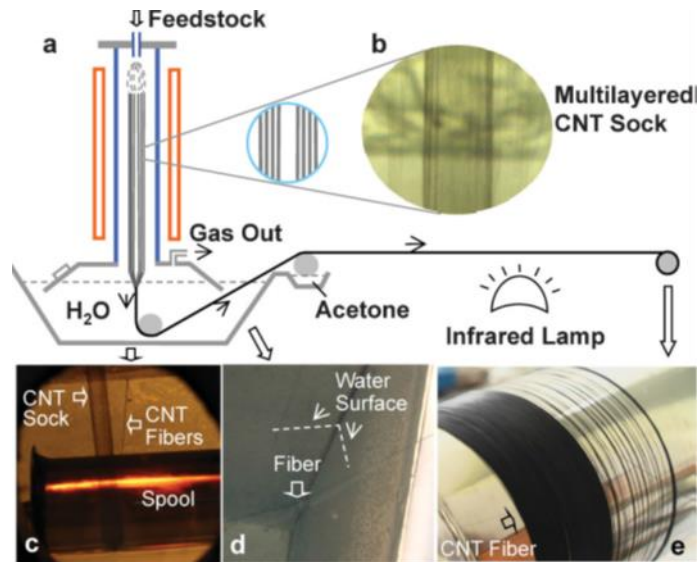
**Figure 2.19:** a) Schematic diagram of CNTs production on CVD system, b) Stacked CNTs layers, c) Spinning of CNTs yarn and collected on roller, d) densification process using water, e) Rolled and densified CNTs yarn [56]

### 2.2.4.3 Dry spinning

This method consists several consecutive including vertically oriented CNTs enlargement, drawing, bending and winding. CNTs growth was carried out on surface oxidized Si wafer using chemical vapor deposition method. Fe particles were used as catalysts on the surface. Acetylene or ethylene was used as carbon sources. The mechanical properties of CNTs were improved by twisting. The greatest advantage of this method is the production of CNTs yarn without using any chemical additives, and enables the production of pure CNTs yarns. However, there are restrictions on the drawing speed and twisting rate. Even still, it provides easy production in the laboratory environment. The schematic line of the CNTs yarn production system is shown in Figure 2.20 [57].
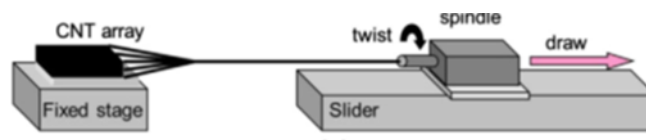


**Figure 2.20:** Schematic illustration of dry spinning CNTs yarn line [57].

CNTs drawing is not possible for all CNTs forests/arrays. Experimental results indicated that the spinnability was strongly dependent on the interspacing between individual CNTs in the forest and their connected network. By the aid of Van der Waals forces, the nanotubes were stacked to each other. If there was slight lateral

connection in the forest, the forest could not be towed. When the forest was pulled from the side wall, a few nanotubes might break apart instead of the separation of continuous layer. Also, the tortuosity of CNTs forest was essential. SEM micrographs of spinnable CNTs is seen in Figure 2.21a and non-spinnable CNTs in Figure 2.21b exhibits tortuous features. Hence, physical properties of CNTs is critical in dry spinning. There are many material and process parameters that affected spinnability. For instance, material variables such as substrate and supporting materials, catalyst materials and their relative amount, carbon sources and process parameters such as partial pressure (feedstock), carrier gas and gas as an etching agent, total flow rate (gas residual time) have play a role in spinnability. In addition process temperature, temperature ramp-up rate and cool-down rate, process pressure, process steps, process time, and many other details, such as the history of the reaction chamber, contamination, size of chamber and substrate, are other factors that affect the nucleation and growth of CNTs forests [59].
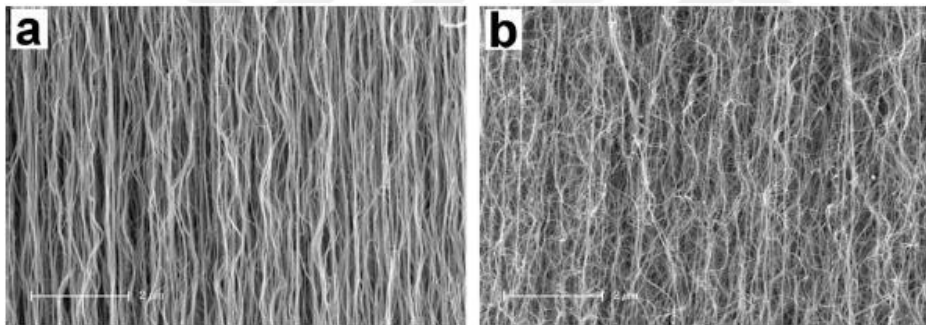


**Figure 2.21:** SEM images of a) high degree of alignment of CNTs grown in 20 min, b) CNTs are grown in 30 min [60].

26

# 3 MATERIALS AND METHODS

## 3.1 Wet Spun Graphene Fibers

### 3.1.1 Materials

In the present work, graphite flakes (particle size +100 mesh ($\geq$75 % min)), potassium permanganate ($KMnO_4$), sulfuric acid ($H_2SO_4$), phosphoric acid ($H_3PO_4$), hydrogen peroxide ($H_2O_2$) and hydrochloric acid (HCl) were obtained from Sigma-Aldrich Chemistry and used for the production of GO synthesis. Deionized water (DI water), Calcium chloride ($CaCl_2$), Sodium hydroxide (NaOH), Ethanol and Methanol purchased from Sigma-Aldrich. Sodium borohydride ($NaBH_4$), hydroiodic acid (HI), ascorbic acid (AA) bought from Sigma-Aldrich and used for GO fiber reduction.

### 3.1.2 Method

#### 3.1.2.1 Graphene oxide (GO) synthesis

In this thesis, modified Hummer's method of synthesis was used for the production of GO. In this method, $H_3PO_4$ was used instead of nitric acid ($HNO_3$) and enabled more environmental conditions [61]. First, $KMnO_4$ and graphite flakes were mixed in a mass ratio of 6:1. Then placed in a glass bottle placed in the oil bath. $KMnO_4$ and graphite flakes mixtures were mechanically stirred. Then, with respect to the graphite flake mass fraction, the initial solid mixing ratio of 9:1 and 1:1 mass ratios $H_2SO_4$ and $H_3PO_4$ were slowly added. The mixture was kept for 24 hours and then cooled with an ice bath. At the end, brownish slurry was obtained. 20:1 (v:v) ice-$H_2O_2$ mixture was added for neutralization. The resulting GO slurry was washed several times with DI water and ethanol aqueous solution. GO nanosheets were dried and conditioned at 70° C for 48 hours.

### 3.1.2.2 GOLCs formation by high-energy sonication method

Due to presence of functional oxide groups GO can be easily dispersed in aqueous solutions when subjected to mild ultrasonic treatment. Graphene oxide liquid crystals (GOLCs) were prepared at four different concentrations of GO in DI water, such as 20, 25, 30 and 40 mg ml$^{-1}$. Each sample was first kept in the sonication bath (4 hours with cooling intervals) (Power: 340 Watts). Then subjected to high-power sonication probe (Power: 650 Watts) as detailed in Table 3.1. It was observed that at higher GO concentrations slightly, higher energy was required.

**Table 3.1:** Time and energy consumption details during ultrasonic treatment of GOLCs.

| Sample Concentration (mg mL$^{-1}$) | Bath Sonication | | Probe Sonication | | Total |
| --- | --- | --- | --- | --- | --- |
| | (Hours) | Energy (MJ) | (Minutes) | Energy (MJ) | Energy (MJ) |
| 20 | 21 | 25.7 | 32 | 0.349 | 26.1 |
| 25 | 30 | 36.7 | 35 | 0.382 | 37.1 |
| 30 | 36 | 44.1 | 39 | 0.425 | 44.5 |
| 40 | 45 | 55.1 | 45 | 0.491 | 55.6 |

### 3.1.2.3 Wet spinning of GO fiber

**Coagulation and washing baths**

In this thesis, various GO concentrations were prepared and tested in various coagulation baths. GO concentrations were set at 20, 25, 30 and 40 mg ml$^{-1}$. Used coagulation baths were listed in Table 3.2.

GO fibers produced in coagulation baths of CTAB were discontinuous and did not reached the desired strength. It was observed that GO fibers could not maintain their structural integrity at low concentrations. Therefore, the preliminary results showed that 20 and 25 mg ml$^{-1}$ GO dispersions were not convenient for fiber production. 30 and 40 mg ml$^{-1}$ GO dispersions were quite available for spinning. Among several coagulation baths, CaCl$_2$ and NaOH were selected for further experiments.

In first trials, the fiber was held with tweezers, and then it was cleaned in DI water and dried. Later, methanol was used as the washing bath. Washing step aimed to neutralize the residues in the coagulation bath. $H_2O$ molecules interacting with GO were partially cleaned by dehydration of fibers. Besides, methanol removed NaOH and $CaCl_2$ residues remaining on the fiber with the aid of hydroxide groups. The results showed that compared to water-washed fibers which $H_2O$ molecules were present even after three days, methanol washed fibers were fully dried in a few minutes [62].

There was no tension in this first trial. Hence, there were strong variations both in fiber cross-section and in diameter due to manual control. In this thesis, custom-made spinning line was also designed for spinning of GO fibers. Table 3.3 summarizes GO concentration, coagulation and washing bath composition and as-spun GO fiber codes for use, which were tested.

**Table 3.2:** Coagulation baths

| Coagulation Baths | |
| --- | --- |
| CTAB (0.5 mg/mL) | DI water |
| | Ethanol |
| | Methanol |
| | Ethanol/ DI water (3:1) |
| | Acetone |
| | 2-Propanol |
| | Ethylene Glycol |
| NaOH (3 wt. %) | Methanol |
| | Ethanol |
| NaOH (5 wt. %) | Methanol |
| | Ethanol |
| CaCl_2 (3 wt. %) | DI water |
| | Methanol |
| | Ethanol |
| | Methanol/ DI water (1:3) |
| | Methanol/ DI water (3:1) |
| | Ethanol/ DI water (1:3) |
| | Ethanol/ DI water (3:1) |
| CaCl_2 (5 wt. %) | DI water |
| | Methanol |
| | Ethanol |
| | Methanol/ DI water (1:3) |
| | Methanol/ DI water (3:1) |
| | Ethanol/ DI water (1:3) |
| | Ethanol/ DI water (3:1) |

**Table 3.3:** GO concentration, coagulation and washing bath composition and sample coding of as-spun GO fiber

| GO Fiber | GO Concentration (mg mL$^{-1}$) | Coagulation Bath Concentration (wt. %) | Coagulation Bath Composition | Washing Bath Composition |
|---|---|---|---|---|
| G30N3 | 30 | NaOH (3) | Ethanol | Methanol |
| G30N5 | 30 | NaOH (5) | Ethanol | Methanol |
| G30C3 | 30 | CaCl$_2$ (3) | Ethanol: DI water (3:1) | Methanol |
| G30C5 | 30 | CaCl$_2$ (5) | Ethanol: DI water (3:1) | Methanol |
| G40N3 | 40 | NaOH (3) | Ethanol | Methanol |
| G40N5 | 40 | NaOH (5) | Ethanol | Methanol |
| G40C3 | 40 | CaCl$_2$ (3) | Ethanol: DI water (3:1) | Methanol |
| G40C5 | 40 | CaCl$_2$ (5) | Ethanol: DI water (3:1) | Methanol |

**<u>Wet spinning system</u>**

This thesis embraces the design and installation of the spinning line for multi-functional graphene fibers, steaming from the conventional wet-spinning systems. In this method, the polymer used is dissolved in solvent and the solution is injected through spinneret to the coagulation bath. These polymers are precipitated in the coagulation bath, immediately solidified and then collected onto take-up cylinder.

Instead of polymers, in graphene fiber production, GO nanosheets dispersed in aqueous medium formed ordered liquid crystals were injected. Crystallographic order of GOLCs can be controlled by varying GO concentration, this order also affect the macroscopic properties of fibers. GOLCs were fed in a controlled manner via syringe pump. Glass syringes were intentionally used to eliminate irregularities on the fiber due to inevitable variations during feeding. In addition, longer needles with L/d >150 was preferred for further GOLCs alignment in the flow direction. This also assisted to achieve higher packing of GO leading better mechanical properties.

The custom-designed spinning line had two consecutive baths. The first bath was the coagulation bath (Figure 3.1a) where GOLCs were precipitated and formed GO fibers. At this point, the relative position of the syringe needle to the coagulation bath was investigated. If the spinneret was totally immersed in the bath, regardless of the depth, continuous fiber production had been succeeded. The second bath was placed to remove chemical residual including salts by methanol washing (Figure 3.1a). Along spinning direction pre-tension were applied by mounted teflon rollers. PVC collection

cylinder was also mounted and take-up speed was controlled by motor. The lateral velocity of take-up cylinder was measured by tuning applied voltage as given in Table 3.4.

GO fiber reached to washing bath about 3 seconds, longer settling times caused brittleness of fibers. Hence, it was precisely controlled. In later versions of spinning device, instead of Teflon guide rollers, circulation pump was mounted for methanol washing. Figure 3.1b shows the latest custom-made wet spinning system.
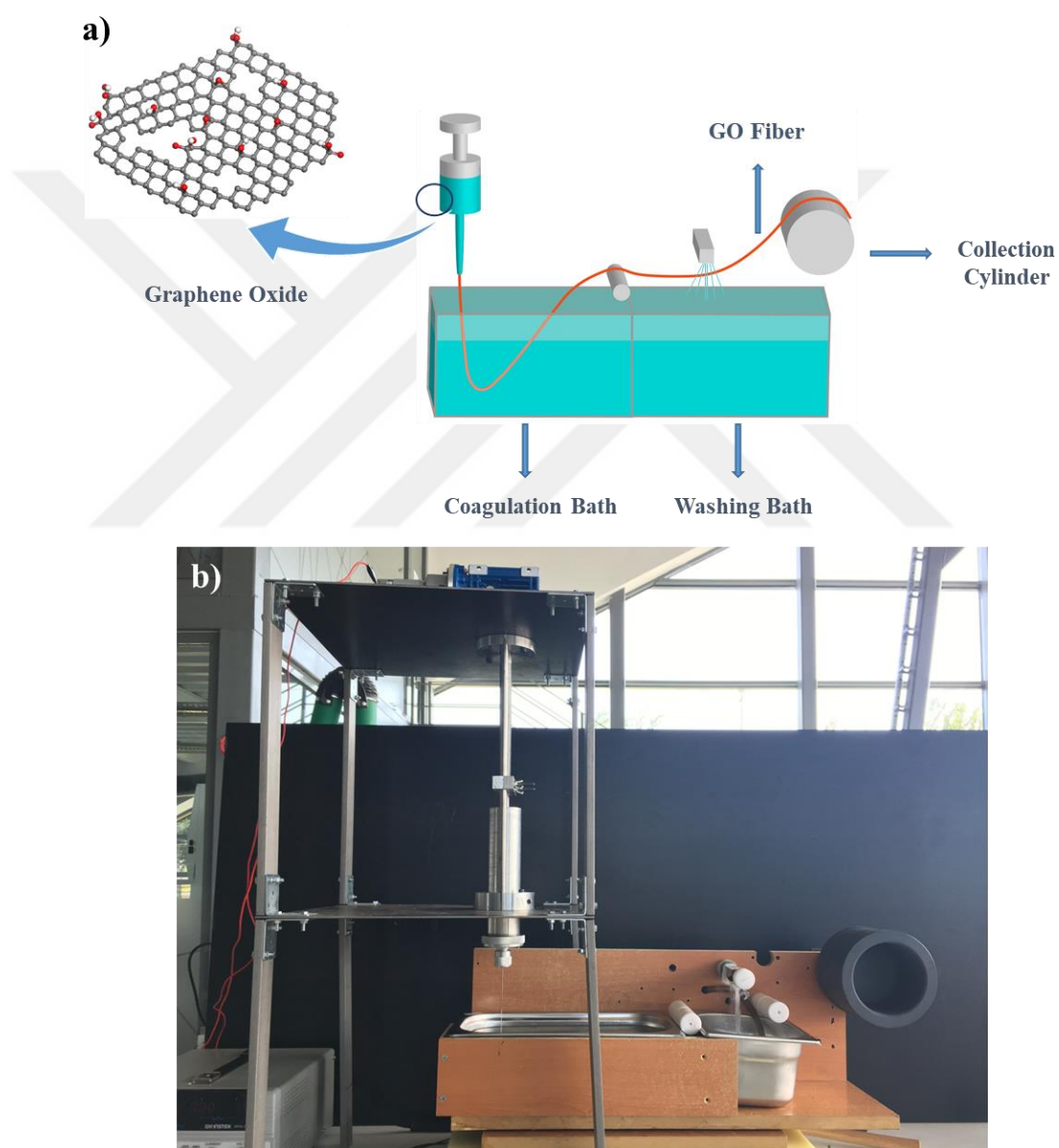


**Figure 3.1:** a) Schematic illustration of wet spinning line for graphene fiber production, b) The real image of latest version of wet spinning device

**Table 3.4:** Collecting cylinder latera velocity depending on applied voltage

| Voltage (V) | Time (s) | Velocity (cm/s) |
|---|---|---|
| 9.9 | 34 | 1.27 |
| 10.4 | 32 | 1.35 |
| 10.9 | 31 | 1.39 |
| 11.3 | 29.4 | 1.46 |
| 11.7 | 28.2 | 1.53 |
| 12 | 27.2 | 1.58 |
| 15 | 21.73 | 1.98 |
| 17.6 | 19.6 | 2.2 |
| 20 | 18.56 | 2.32 |

**Chemical reduction of GO fibers**

As next step, when electrical conductivity is promised, elimination of functional groups in graphene oxide sheets are required to conduct. There are different reduction methods such as thermal reduction, microwave irradiation, chemical reduction and flash reduction, as discussed in introduction. Chemical reduction methods so far gave the most reliable data without sacrificing mechanical performance. In this thesis, three different chemical reduction methods were used:

- 55 wt.% Hydrogen iodide (HI) aqueous solution at 100 °C [63]
- 2 mM Ascorbic acid (AA) solution in DI water at 60 °C [19]
- 2.4 M Sodium borohydride ($NaBH_4$) aqueous solution [14]

The reduced fibers were then washed with DI water and dried at 60 °C overnight. Electrically conductive, strong and flexible reduced graphene fibers,in other words graphene fibers, were produced as shown in Figure 3.2.



**Figure 3.2:** Graphene fiber

## 3.2    Dry Spun CNTs Fiber

### 3.2.1    Materials

P-type <100> Si wafers were obtained from Uniwafer Company. Iron (Fe) Pellets Evaporation Materials (99.95% purity) were purchased from Kurt J. Lesker Company and used for silicon coating  in Electron Beam (E-beam) $H_2$, $C_2H_4$ and He gases were used for VA-CNTs production within the scope of the project. Gases were supplied from Air Liquide Company in 50-liter tubing. $H_2$ gas is 99.999% pure, colorless, odorless, flammable and much lighter than air. He gas is 99.999% pure, colorless, odorless, compressed and much lighter than air. $C_2H_4$ gas is 99.999% pure, colorless, light to air, liquefied, slightly flammable gas with slightly sweet odor.

### 3.2.2    Method

In this thesis, th-CVD system used for the production of vertical aligned CNTs forests/arrays, where the system was easy to operate and had precise control. First, coated wafers were prepared, and then CNTs were grown on top of these substrates.

### 3.2.2.1    Wafer preparation

Vertically aligned carbon nanotube (VA-CNTs) were synthesized by th-CVD with high yield and high quality. First, p-type silicon wafer was oxidized to the approximately 300 nm by plasma enhanced chemical vapor deposition (PE-CVD) to grow highly dense CNTs (Figure 3.3a). Buffer layer/catalyst particle as $Al_2O_3$/Fe with a thickness of 10:2 nm were coated Si/$SiO_2$ wafer by E-beam evaporation technique (Figure 3.3b). The combination He and $H_2$ were introduced into 2-inches quartz tube to nucleate catalyst particle at 750°C for 15 min. $C_2H_4$ at a rate of 400 sccm was allowed to achieve the growth of VA-CNTs with high yield for 15 min. After growth stage finished, He was purged into a quartz tube to. Figure 3.4 shows an illustration of the coated wafer, which describes VA-CNTs synthesis.
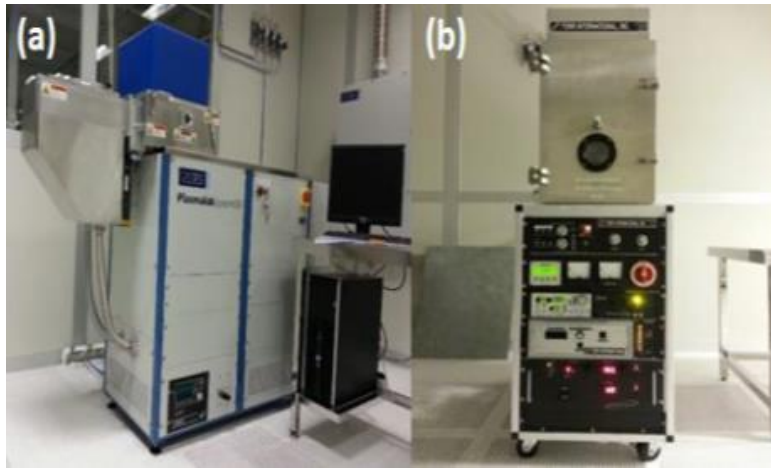
**Figure 3.3:** a) Plasma-enhanced chemical vapor deposition, b) Electron beam processing (E-beam).

In this thesis, four different types of wafers were used as substrate to monitor its effect on spinnability. Figure 3.4 depicts 1st wafer type which had 4-layered system coated with 1) P type <100> Si wafer, 2) $SiO_2$ ~300 nm, 3) $Al_2O_3$ ~10 nm, 4) Fe ~2nm . 2nd type of wafer had lack of $SiO_2$ layer, only coated with P-type <100> Si wafer, $Al_2O_3$ ~10 nm and Fe ~2nm. 3rd type wafers did not have any support material and only consisted wafers and catalysts as P-type <100> Si wafer and Fe ~ 2nm,as reported in ref study [59]. 4th type had thicker Fe coating to increase CNTs diameter, and coated with P-type <100> Si wafer, $Al_2O_3$ ~10 nm and Fe ~ 6nm [64].
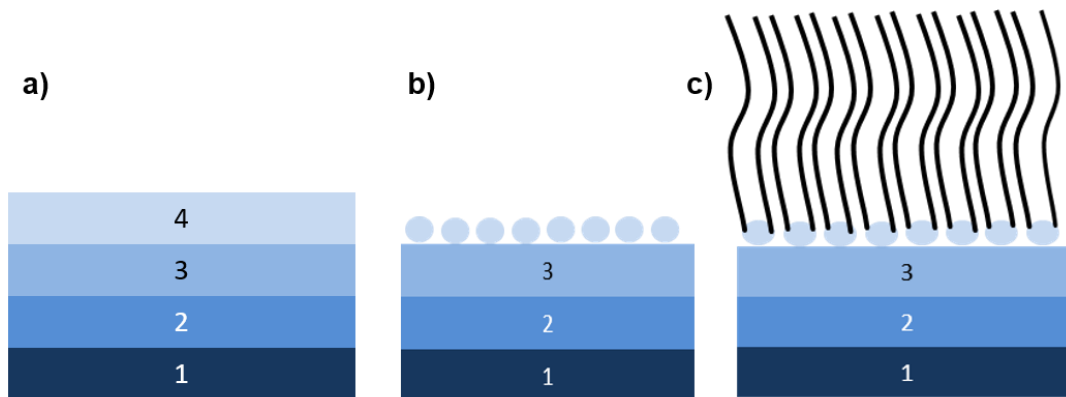


**Figure 3.4:** a) Coated wafer to grow CNTs [1) P type <100> Si wafer, 2) $SiO_2$ ~300 nm, 3) $Al_2O_3$ ~10 nm, 4) Fe ~2nm], b) Nucleation step, c) Growth step and CNTs synthesis

### 3.2.2.2 VA-CNTs forest preparation

The schematic representation of th-CVD is shown in Figure 3.5. This system, located in ITU Aerospace Research Center (ITUARC), can be fed with He, $H_2$, $C_2H_4$ and water vapor ($H_2O$). Th-CVD process with Linberg / Blue M tube furnace used 2-inch quartz tube. Figure 3.6 shows th-CVD equipments in ITU Aerospace Research Center. The software designed by Assist Prof A. F. Ergenç controlled gas flow rate, time and furnace temperature.
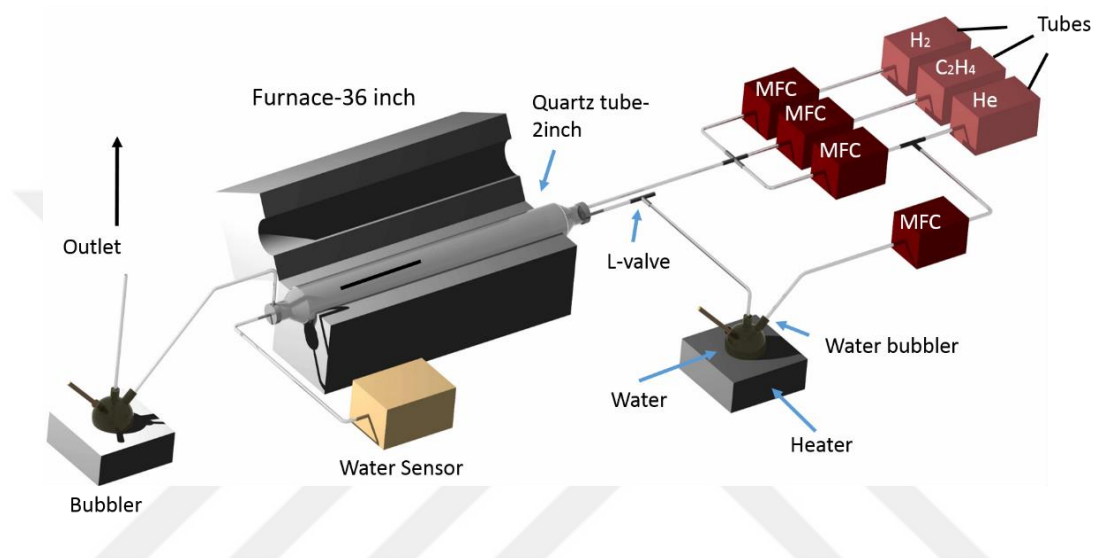


**Figure 3.5:** Schematic representation of VA-CVD at ITUARC.
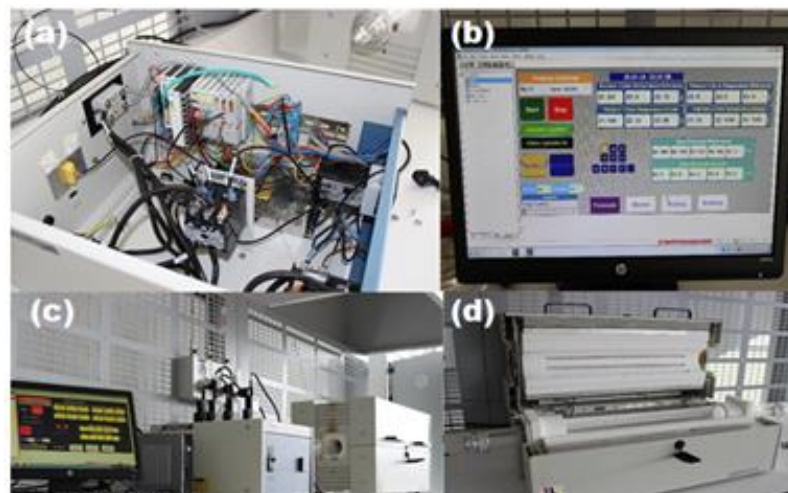


**Figure 3.6:** Th-CVD equipments; a) Heater, b) PLC c) Flow meters of He, $H_2$ and $C_2H_4$, d) Furnace

CNTs growth mechanism in the CVD system can be varied by the system and used protocol. The CNTs growth protocol basically consisted these five consecutive steps.

1. Purging: Gases includes He, Ar were purged to remove the gases in the environment like $O_2$ from the quartz tube.

2. Nucleation: This step included heating the tube for nucleation of the catalyst particles He and $H_2$ gases are fed inside reaction zone. (Figure 3.4b)

3. Growth: $C_2H_4$ gas was fed to the system as hydrocarbon source. CNTs growth initiated at this step. (Figure 3.4c)

4. Easy delamination: Once the growth was completed, $H_2$ gas was sent for one minute to easily separate the CNTs from the surface.

5. Cool down: He gas was fed until the system was cooled down to room temperature.

$H_2$ gas in the easy delamination step broke bonds between the surface and the CNTs as well as disrupting weak bonds between CNTs. In fact, van der Waals interactions have played an important role in the continuity of dry spinning. Contrary to well-establish protocol in ITUARC, in this thesis, easy delamination step was eliminated.

**Table 3.5:** Standard ITUARC protocol for the synthesis of VA-CNTS by th-CVD

| | He (sscm) | H$_2$ (sscm) | C$_2$H$_4$ (sscm) | Time (min) | Temperature (°C) |
|---|---|---|---|---|---|
| | 2000 | 0 | 0 | 1 | RT |
| **Purge** | 2000 | 500 | 0 | 1 | RT |
| | 2000 | 500 | 500 | 1 | RT |
| **Nucleation** | 1600 | 1000 | 0 | 15 | 750 |
| **Growth** | 1000 | 600 | 400 | 15 | 750 |
| **Easy-delamination** | 1000 | 500 | 0 | 1 | 750 |
| **Cool-Down** | 2000 | 0 | 0 | 0 | 650 |
| | 300 | 0 | 0 | 0 | 250 |

Within the scope of this thesis, as noted in Table 3.6, a variety of protocols and substrates for growth was tested. It is important to address that $SiO_2$ named wafer term in Table 3.6, referred to P-type <100> Si wafer, $SiO_2$ ~300 nm, $Al_2O_3$ ~10 nm and Fe ~2nm whereas $SiO_2$ free named wafer consisted P-type <100> Si wafer, $Al_2O_3$ ~10 nm and Fe ~2nm.

**Table 3.6:** Details of CNTs synthesis set codes used in this thesis

| Set Codes | Description | Used Wafer Type |
|-----------|-------------|-----------------|
| C | Synthesis uses standard protocol. | $SiO_2$ Free |
| W | Protocol includes by feeding water vapor. | $SiO_2$ Free |
| T | Protocol uses thicker iron layer on a silicon wafer. | $SiO_2$ Free (Fe ~6nm) |
| Z | Protocol proposed by Zhang *et al.* (2009). | $SiO_2$ $SiO_2$ Free |
| J | Protocol proposed by Jayasinghe and Chakrabarti (2011). | $SiO_2$ $SiO_2$ Free |
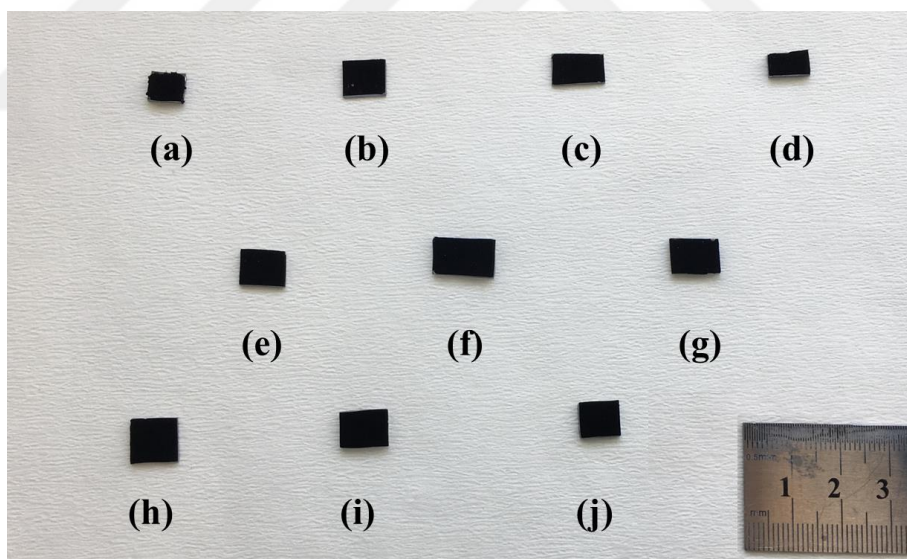


**Figure 3.7:** Photo images of synthesized C set CNTs forests (top view) (a) C-1, (b) C-2, (c) C-3, (d) C-4, (e) C-5, (f) C-6, (g) C-7, (h) C-8, (i) C-9, (j) C-10.
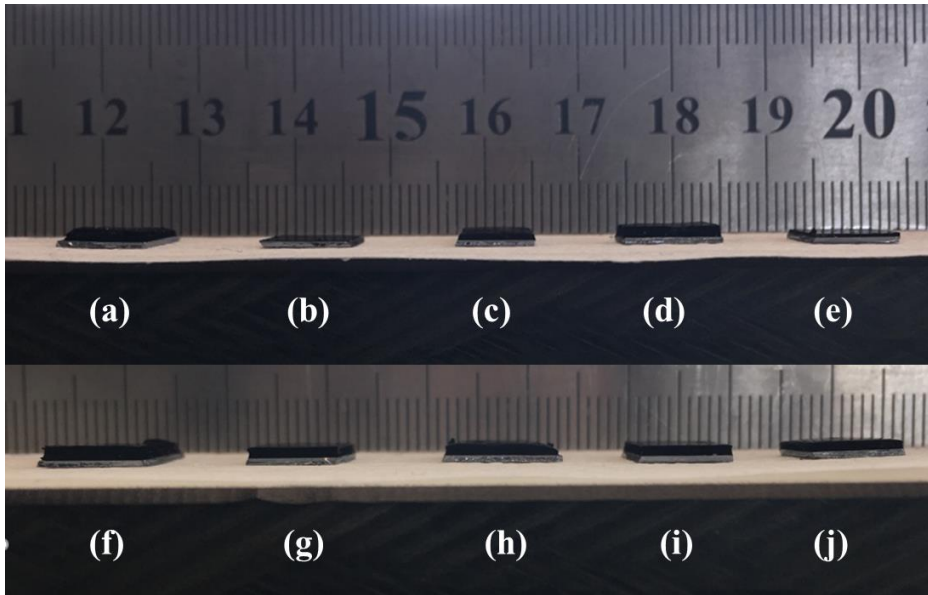
**Figure 3.8:** Images of synthesized C set CNTs forests (front view). (a) C-1, (b) C-2, (c) C-3, (d) C-4, (e) C-5, (f) C-6, (g) C-7, (h) C-8, (i) C-9, (j) C-10.

Earlier studies demonstrated that only $C_2H_2$/Ar (without $H_2$, $H_2O$ or other gases) and thin Fe film (without buffer layers such as $SiO_2$ and $Al_2O_3$) on the Si substrate were assisted to produce attractable CNTs forests [59]. Fe ~ 2nm coated P-type <100> Si wafer was tried in the standard ITUARC protocol as detailed in Table 3.5. Unfortunately, growth process did not undergo This could be associated to the disappearance of Fe atoms in the nucleation step. Hence, this type of chips was not used for further studies.

Several changes were made stemming from standard ITUARC protocol to achieve spinnable CNTs forests. First, the optimum growth time was investigated by decreasing the growth stage. Then, the changes in the feeding rates of $H_2$ and $C_2H_4$ had done. Nucleation time was kept constant in all data sets, which was optimized 15 minutes earlier. All changes done in standard ITUARC protocol are given in Table 3.7. At standard ITUARC protocol, the wafer without $SiO_2$ buffer layer ($SiO_2$ free wafer) resulted in better CNTs forests compared to earlier studies. After decision on the use of $SiO_2$ free wafer, standard protocol was tuned by growth time and gas fluxes as in the Table 3.7 shows. In addition, the photography of C set CNTs forests are provided in Figure 3.7 and Figure 3.8. In the next section, the Raman and image processing of these images will be discussed.

**Table 3.7:** Optimization of the growth time and gas fluxes in standard ITUARC protocol.

| Sample Name | Wafer Type | Nucleation Time (min) | Growth Time (min) | He (sccm) | $H_2$ (sccm) | $C_2H_4$ (sccm) |
|---|---|---|---|---|---|---|
| C-1 | $SiO_2$ free | 15 | 15 | 1000 | 600 | 400 |
| C-2 | $SiO_2$ free | 15 | 12 | 1000 | 600 | 400 |
| C-3 | $SiO_2$ free | 15 | 9 | 1000 | 600 | 400 |
| C-4 | $SiO_2$ free | 15 | 6 | 1000 | 600 | 400 |
| C-5 | $SiO_2$ free | 15 | 3 | 1000 | 600 | 400 |
| C-6 | $SiO_2$ free | 15 | 9 | 1000 | 400 | 400 |
| C-7 | $SiO_2$ free | 15 | 9 | 1000 | 200 | 400 |
| C-8 | $SiO_2$ free | 15 | 9 | 1000 | 0 | 400 |
| C-9 | $SiO_2$ free | 15 | 9 | 1000 | 200 | 200 |
| C-10 | $SiO_2$ free | 15 | 9 | 1000 | 200 | 600 |

The growth period plays an important role on the CNTs length and quality. The amorphous carbons that went up in the growth phase settled on the CNTs and ceased to grow. There would also affect the production quality due to the accumulation of amorphous carbon with increased growth period. Water vapor might help to sweep amorphous carbons. Therefore, longer and higher quality CNTs could be synthesized [65].

In this thesis, CNTs forest production was also carried out with fed water vapor into th-CVD system. As shown in Figure 3.5, He used in CVD was passed through two MFCs and one of them was moved through the water vapor, and quartz pulp transport of water vapor was provided. Water vapor was fed only at the growth stage, by dividing the 1000 sccm He used in the standard protocol. These were sent to 500-500, 750-250, 950-50 and 990-10 sccm (The first value was directly sent to the inside of the tube, and the second represented the water vapor). It was not well tracked how much water vapor was sent into the tube; the necessary of a hydrometer in the tube inlet was noted. In addition, the valve that allowed water vapor entry was used manually. This valve was opened during CNTs growth step and closed at the end of this stage.

Water assisted (W) protocol was designed by inspired from standard ITUARC protocol as shown in Table 3.8. First, He passing through the water vapor on the standard recipe was optimized. As shown in Table 3.8, fluxes in the range of 500-500,

750-250, 950-50 and 990-10 were set. When high amount of He passed through the water vapor, the structure showed more fringed and irregular image, that surface morphologies are critical for spinnability. In terms of surface features, He flux of 950-50 sccm was optimum. Afterwards, the growth time was increased, starting from 15 minutes to 2.5 hours. Then $H_2$ and $C_2H_4$ fluxes were changed. The effect of reduced nucleation time was also investigated. The images of W set CNTs forests are shown in Figure 3.9 and Figure 3.10. In the next section, the Raman and image processing of these W sets will be discussed

**Table 3.8:** Optimization of the nucleation time, the growth time and gas fluxes in water assisted protocol.

| Sample Name | Wafer Type | Nucleation Time (min) | Growth Time (min) | He (sccm) | He in Water (sccm) | $H_2$ (sccm) | $C_2H_4$ (sccm) |
|---|---|---|---|---|---|---|---|
| W-1* | $SiO_2$ free | 15 | 15 | 500 | 500 | 600 | 400 |
| W-2* | $SiO_2$ free | 15 | 15 | 750 | 250 | 600 | 400 |
| W-3* | $SiO_2$ free | 15 | 15 | 950 | 50 | 600 | 400 |
| W-4 | $SiO_2$ free | 15 | 15 | 950 | 50 | 600 | 400 |
| W-5 | $SiO_2$ free | 15 | 15 | 990 | 10 | 600 | 400 |
| W-6 | $SiO_2$ free | 15 | 15 | 950 | 50 | 400 | 400 |
| W-7 | $SiO_2$ free | 15 | 30 | 950 | 50 | 600 | 400 |
| W-8 | $SiO_2$ free | 15 | 60 | 950 | 50 | 600 | 400 |
| W-9 | $SiO_2$ free | 15 | 30 | 950 | 50 | 400 | 400 |
| W-10 | $SiO_2$ free | 15 | 90 | 950 | 50 | 600 | 400 |
| W-11 | $SiO_2$ free | 15 | 120 | 950 | 50 | 600 | 400 |
| W-12 | $SiO_2$ free | 15 | 150 | 950 | 50 | 600 | 400 |
| W-13 | $SiO_2$ free | 15 | 60 | 950 | 50 | 400 | 400 |
| W-14 | $SiO_2$ free | 10 | 15 | 1000 | - | 600 | 400 |
| W-15 | $SiO_2$ free | 10 | 30 | 1000 | - | 600 | 400 |
| W-16 | $SiO_2$ free | 10 | 60 | 1000 | - | 600 | 400 |
| W-17 | $SiO_2$ free | 10 | 15 | 950 | 50 | 400 | 400 |
| W-18 | $SiO_2$ free | 15 | 30 | 1000 | | 600 | 400 |

*There is easy delamination step in protocol.
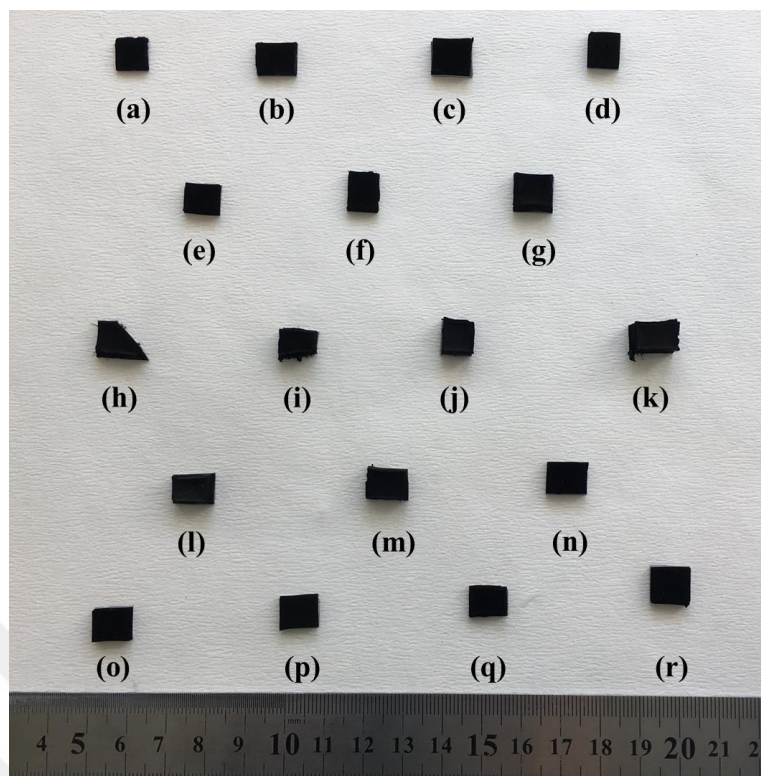
**Figure 3.9:** Images of synthesized W set CNTs forests (top view). (a) W-1, (b) W-2, (c) W-3, (d) W-4, (e) W-5, (f) W-6, (g) W-7, (h) W-8, (i) W-9, (j) W-10, (k) W-11, (l) W-12, (m) W-13, (n) W-14, (o) W-15, (p) W-16, (q) W-17, (r) W-18.
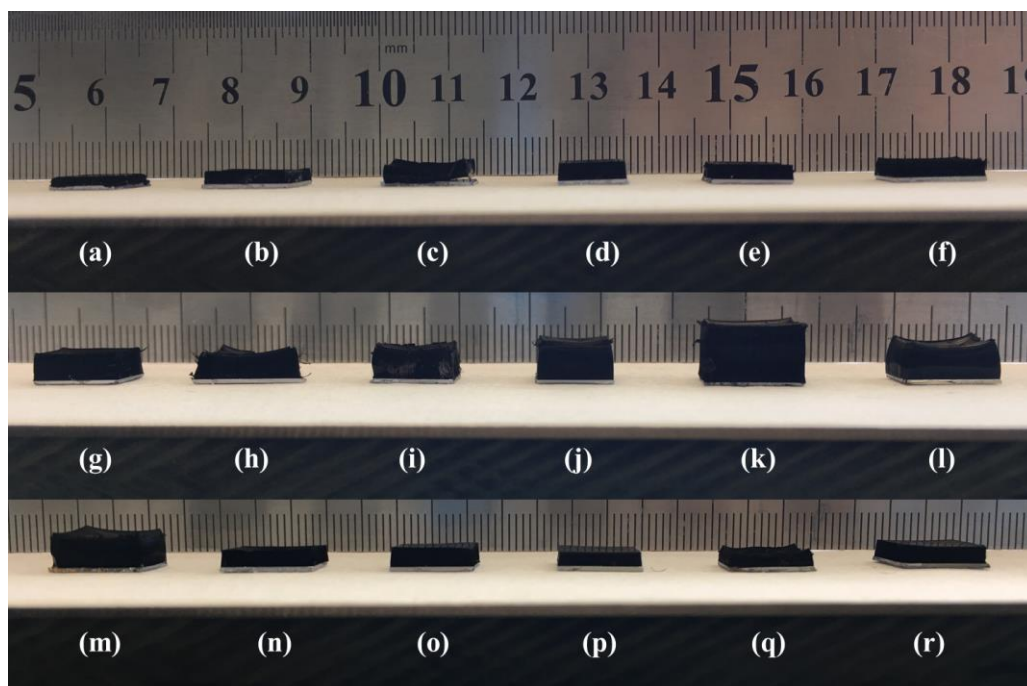


**Figure 3.10:** Images of synthesized W set CNTs forests (front view). (a) W-1, (b) W-2, (c) W-3, (d) W-4, (e) W-5, (f) W-6, (g) W-7, (h) W-8, (i) W-9, (j) W-10, (k) W-11, (l) W-12, (m) W-13, (n) W-14, (o) W-15, (p) W-16, (q) W-17, (r) W-18.

If CNTs were well aligned and almost parallel to each other with high density, they could be spinnable. Moreover, if CNTs nucleation density (or high density of catalyst nanoparticle sites) was high, super-aligned CNTs could be synthesized [64].

From this point of view, 6nm Fe coated wafer (P-type <100> Si wafer, $Al_2O_3$ ~10 nm and Fe ~6nm) was tested. First, as shown in Table 3.9, standard ITUARC protocol was tried., but CNTs growth on the surface could not be achieved. We thought that the 15 min nucleation period, ideal for 2 nm Fe coating, was not enough for 6 nm Fe coating. Thus, the duration of nucleation was increased. Nucleation time of 25 minutes were used for further experiments. The growth period was increased for longer CNTs but the expected forest length did not be seen. In addition, the water vapor rate was also changed to experiment. The images of the T set CNTs forests are shown in Figure 3.11 and Figure 3.12. In the next section, the Raman and image processing of these T sets will be discussed

**Table 3.9:** CNTs synthesis optimizations of the nucleation time, growth time and gas values on 6 nm Fe coated wafer.

| Sample Name | Wafer Type | Nucleation Time (min) | Growth Time (min) | He (sccm) | He in Water (sccm) | $H_2$ (sccm) | $C_2H_4$ (sccm) |
|---|---|---|---|---|---|---|---|
| T-1 | $SiO_2$ free | 15 | 15 | 950 | 50 | 600 | 400 |
| T-2 | $SiO_2$ free | 20 | 15 | 950 | 50 | 600 | 400 |
| T-3 | $SiO_2$ free | 25 | 15 | 950 | 50 | 600 | 400 |
| T-4 | $SiO_2$ free | 30 | 15 | 950 | 50 | 600 | 400 |
| T-5 | $SiO_2$ free | 25 | 30 | 950 | 50 | 600 | 400 |
| T-6 | $SiO_2$ free | 25 | 10 | 950 | 50 | 600 | 400 |
| T-7 | $SiO_2$ free | 25 | 15 | 750 | 250 | 600 | 400 |
| T-8 | $SiO_2$ free | 25 | 15 | 500 | 500 | 600 | 400 |
| T-9 | $SiO_2$ free | 25 | 30 | 750 | 250 | 600 | 400 |
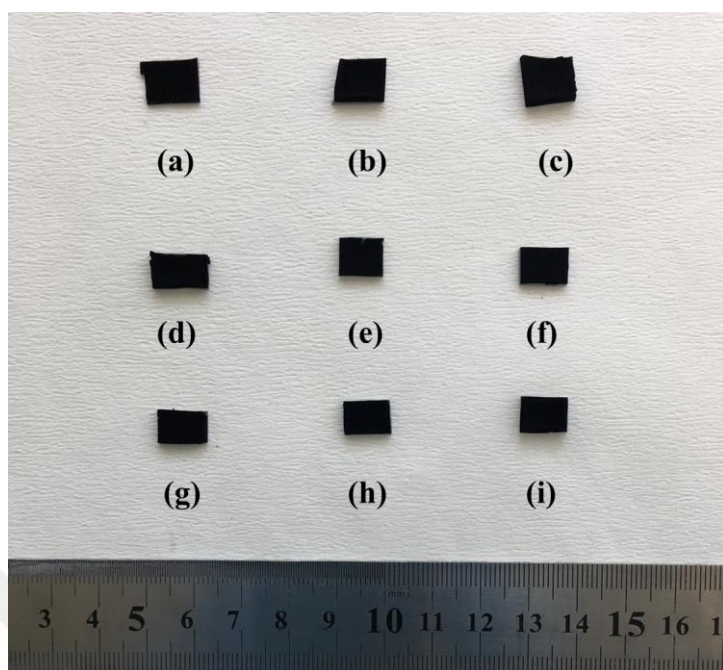
**Figure 3.11:** Images of synthesized T set CNTs forests (top view). (a) T-1, (b) T-2, (c) T-3, (d) T-4, (e) T-5, (f) T-6, (g) T-7, (h) T-8 and (i) T-9
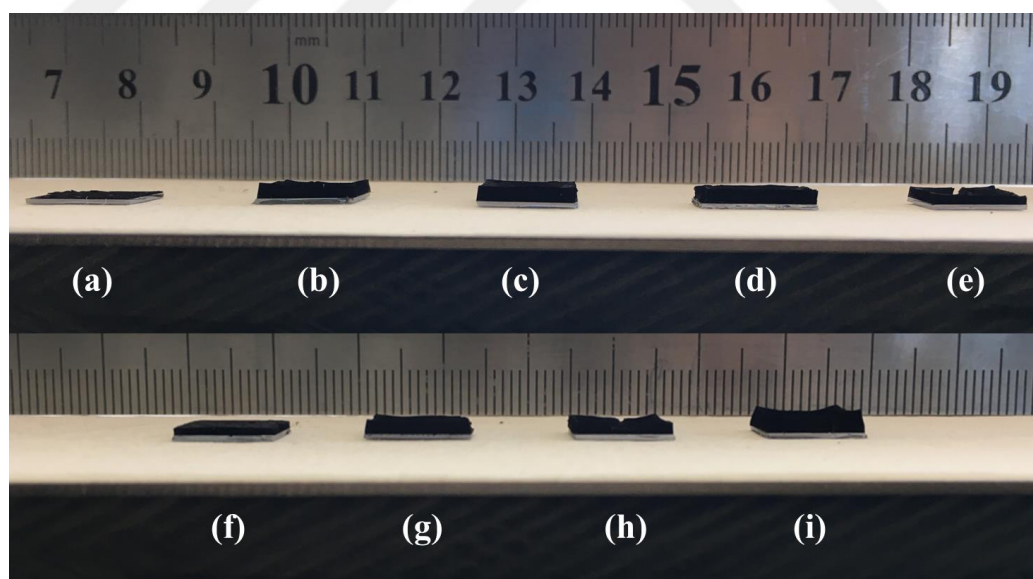


**Figure 3.12:** Images of synthesized K set CNTs forests (front view). (a) T-2, (b) T-3, (c) T-4, (d) T-5, (e) T-6, (f) T-7, (g) T-8, (h) T-9

Zhang *et al.* (2009) pointed out that short-term nucleation time allowed the growth of the best spinnable CNTs forest, while long-term nucleation time resulted in irregular CNTs and the spinnability was reduced. Figure 3.13a shows the proposed CNTs synthesized steps. S1 was the step where the temperature was increased and set as 10 minutes. S2 was the catalyst pretreatment step, S3 was the CNTs growth step and S4 was the cooling steps. In this respect, overall the studies suggested short S2 step and emphasizing that 0 min was the best. The reason for this shown schematically in Figure 3.13b. The small catalyst particles formed in the nucleation processing process recuperated into larger particles. Due to the formation of coalesced catalyst particles, the distance between the particles increased and became irregular. This led to the growth of CNTs with a large diameter and low areal density. These catalyst particles also resulted in poorly aligned growth of the CNTs sequences. According to the literature, CNTs should have smaller diameters and more uniform alignment. The synthesis of CNTs via proposed way would be more densely packed than other samples and the spinnability would be increased.

Based on this assumption, new set of experiments were conducted. The prescription gas rates applied in the literature were excluded and iterated according to our system on the recipe (Z-1, Z-2, Z-3, Z-4, Z-5, Z-6 and Z-7). These experiments are shown in Table 3.10. Our CVD system does not allow controlled temperature increase for S1 step. However, the observed increase in temperature from 30 °C to 750 °C was calculated as 10 minutes.

Another detailed study on spinnable CNTs protocol belongs to Jayasinghe *et al* (2011). The literature, in general, indicated that the CNTs growth rate increased with increasing partial pressure of $C_2H_4$. However, the high partial pressure of $C_2H_4$ caused drastically increased amorphous carbon deposits on CNTs. As a result, the spinnability of the CNTs forest was reduced [65]. Ideal gas fluxes for long, high quality and spinnable CNTs forest were also studied. These optimum rates were given as $H_2O$-to-$C_2H_4$ ratio of 1.2 and $H_2$-to-$C_2H_4$ ratio of 0.8. The synthesized CNTs were derived from there reference studies from the literature. These set of experiment is shown in Table 3.10 (J-1). In the next section, the Raman and image processing of these J set will be discussed
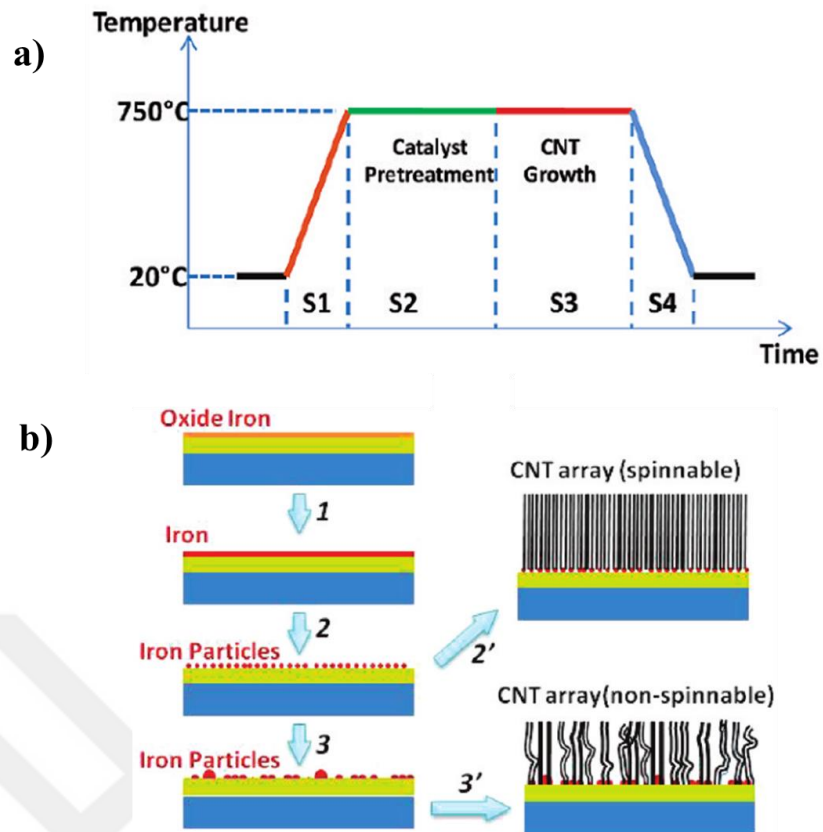
**Figure 3.13:** (a) CNTs synthesis in four steps by CVD. S1, ramping up the temperature; S2, catalyst pretreatment; S3, CNTs growth; S4, cooling down. (b) Schematic illustration of the formation of catalyst film and resulting CNTs array [66].

**Table 3.10:** CNTs synthesis optimizations of the nucleation time, growth time and gas values by inspired from the studies in literature.

| Sample Name | Wafer Type | Nucleation Time (min) | Growth Time (min) | Nucleation Step | | Growth Step | | | |
|---|---|---|---|---|---|---|---|---|---|
| | | | | He (sccm) | $H_2$ (sccm) | He (sccm) | He in Water (sccm) | $H_2$ (sccm) | $C_2H_4$ (sccm) |
| Z-1 | $SiO_2$ free | 10 | 15 | 2340 | 260 | 950 | 50 | 600 | 400 |
| | $SiO_2$ | 10 | 15 | 2340 | 260 | 950 | 50 | 600 | 400 |
| Z-2 | $SiO_2$ free | 5 | 15 | 2340 | 260 | 950 | 50 | 600 | 400 |
| | $SiO_2$ | 5 | 15 | 2340 | 260 | 950 | 50 | 600 | 400 |
| Z-3 | $SiO_2$ free | 0 | 15 | 2340 | 260 | 950 | 50 | 600 | 400 |
| | $SiO_2$ | 0 | 15 | 2340 | 260 | 950 | 50 | 600 | 400 |
| Z-4 | $SiO_2$ free | 15 | 15 | 2340 | 260 | 950 | 50 | 600 | 400 |
| | $SiO_2$ | 15 | 15 | 2340 | 260 | 950 | 50 | 600 | 400 |
| Z-5 | $SiO_2$ free | 0 | 10 | 1600 | 100 | 1600 | - | 100 | 300 |
| | $SiO_2$ | 0 | 10 | 1600 | 100 | 1600 | - | 100 | 300 |
| Z-6 | $SiO_2$ free | 10 | 10 | 1600 | 100 | 1600 | - | 100 | 300 |
| | $SiO_2$ | 10 | 10 | 1600 | 100 | 1600 | - | 100 | 300 |
| Z-7 | $SiO_2$ free | 10 | 10 | 1000 | 60 | 1000 | - | 60 | 240 |
| | $SiO_2$ | 10 | 10 | 1000 | 60 | 1000 | - | 60 | 240 |
| J-1 | $SiO_2$ free | 15 | 15 | 1000 | 600 | 520 | 480 | 320 | 400 |
| | $SiO_2$ | 15 | 15 | 1000 | 600 | 520 | 480 | 320 | 400 |

### 3.2.2.3 Design of dry spinning device

After the successful synthesis of spinnable CNTs on the silicon wafer, dry spinning takes place to form CNTs yarns. The system in Figure 3.14 was inspired from the literature studies. This system has sliding system consisting of two motors. A motor hitch gave pivoting motion to the pointer spindle and enabled twisting motion while operating at maximum of 7V at 700 rpm. Approximately every 1V increase corresponds to 100 rpm and the spindle speed was set accordingly. While the second step motor gave pullback motion, via an algorithm, maximum speed was obtained by waiting 1 millisecond whereas minimum speed was possible by waiting 10 milliseconds between each step. The angular velocity ($\omega$) was calculated from equation (3.1). $\Delta\theta$ and $\Delta t$ equations refers angular displacement and time, respectively. The maximum speed was calculated as 31.4 rad/s and the minimum speed was 3.14 rad/s. In addition, 12 V was supplied to the motor from the power supply.

$$\omega = \frac{\Delta\theta}{\Delta t} \ (rad/s) \tag{3.1}$$

The silicon wafer was fixed onto the retractable plate. Before CNTs yarn was produced, a spinning triangle was formed with tweezers. The tip of the pulling triangle was twisted and then connected to the pointed tip of the first motor. When the second motor pulled the wafer back, the first motor span CNTs yarn and the process was completed. Speed optimization of the motors was completed during process.
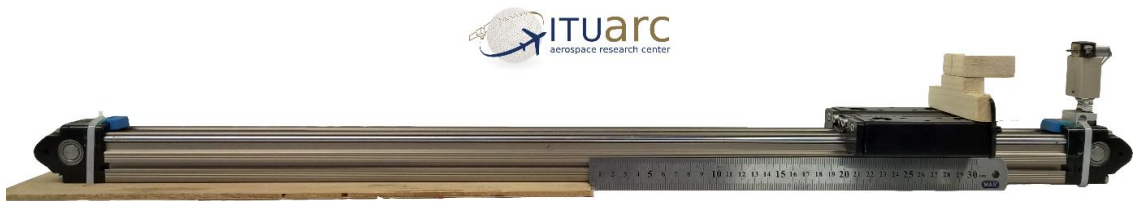


**Figure 3.14:** Dry spinning line for CNTs yarn production

### 3.3 Characterization Analysis

### 3.3.1 Raman spectroscopy

In Raman Spectroscopy method, laser beams with certain wavelengths are sent over the examined specimens. The laser beams interact with the bonds the sample structure and radiate (e.g., C-C, C-C, C-O, C-O bonds, etc.). As a result, it is possible to determine the which type of bonding present in the specimen [60, 67].

Raman spectroscopy studies were performed with a laser excitation line at 532 nm with Renishaw Raman spectrometer at a spectral range of 100-3200 cm$^{-1}$.

### 3.3.2 X-Ray diffraction (XRD)

X-ray diffraction method (XRD) is based on the principle of sending X-rays at certain angles, depending on the specific atomic sequences of each crystal planes. For each crystal plane, these diffraction patterns define the fingerprint of crystal.

XRD measurements of GO nanosheets, GO fibers, and graphene fibers were performed in the study. Bruker D-8 Advance X-ray diffractometer was used. The irradiation wavelength of Cu K$\alpha$ was 0.154 nm. The scanning speed was 2.4° min$^{-1}$ with 40 kV operating voltage and 40 mA current. XRD measurements were performed at $2\theta$ in the range of 5° to 90°.

### 3.3.3 Morphological characterization of materials

Scanning electron microscope (SEM) images were taken at 5 kV acceleration voltage on a scanning electron microscope (ZEISS LEO Supra 35 VP) to observe the orientation and packing degree of the GO fibers the morphology of CNTs array and yarns. In addition, the fracture surfaces of fibers subjected to tensile testing was studied by SEM. The morphologies of CNTs forests and volume fraction of aligned CNTs was quantitatively investigated by QAUNTA FEG 250 SEM at 15 kV acceleration voltage.

Stereomicroscope (ZEISS Stemi 2000-C) was used to measure CNTs forests lengths on wafer and graphene fibers diameter in ITU ARC Laboratory. Axiocam 105 color microscope camera with 5 megapixels and 2.0x Lens were used on this Stereomicroscope.

### 3.3.4 Mechanical testing

Uniaxial tensile tests were performed by universal testing machine (UTM), Shimadzu AG-X plus with 1 kN load cell. In this research ASTM D 3379-75 [68] standard was followed and single fibers were tested. As shown in Figure 3.15, test specimens were prepared.

At least 8 tests were made from each sample set as shown in Figure 3.16. Later, these data were processed to calculate strain to failure %, specific stress (MPa/g.cm$^{-3}$) specific module (MPa/g.cm$^{-3}$). The mechanical properties of the produced graphene fibers were obtained.

NaOH coagulated samples became wavy structure after drying. The CaCl$_2$ samples were more linear and uniform structure. For this reason, pre-loading was applied in each test.
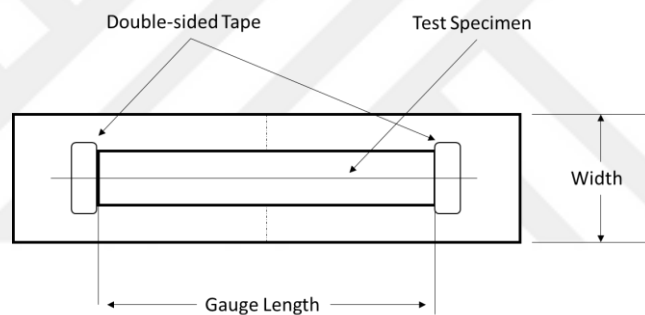


**Figure 3.15:** Schematic diagram of sample preparation for single fiber
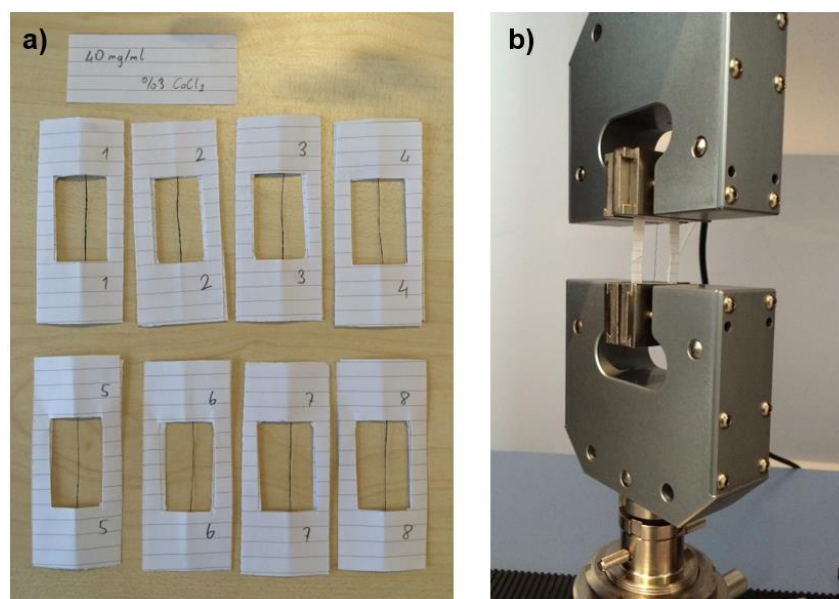


**Figure 3.16:** a) Sample set and b) Sample implementation during tensile testing

### 3.3.5 Electrical conductivity measurements

The electrical conductivity of the graphene fibers was measured with CR Cascade Microtech CP 4-point probe conductivity meter. The probe distance was 1 mm. The electric conductivity ($\sigma$) is calculated from equation (3.2). $\rho$, t, V and $i$ in the equation are resistance, thickness, voltage and current, respectively.

$$\rho = \frac{\left(\frac{\pi t}{ln2}\right) V}{i} = \frac{1}{\sigma} \tag{3.2}$$

# 4    RESULT AND DISCUSSION

## 4.1    GO Fiber

Flexible, strong and electrically conductive graphene fibers with scalable production aimed at this thesis, which are emerging materials in electronic textiles and sensors.

First, XRD analysis provides information on the crystallinity of the material, the degree of amorphousness and the crystallographic information. Figure 4.1 shows the XRD results of the graphite material and produced GO. In the red graphite spectrum, two $2\theta$ peaks were detected. These were sharp (002) peak at 23°and (004) peak. From these peaks, it was proved that the material was graphite [27]. The carbon atoms in the graphite structure were arranged in hexagonal form. In the graphene structures, carbon atoms are in the form of 2-dimensional sheet. The interlayer spacing was increased by chemical oxidation of the graphite structure layers and GO nanosheets were obtained. The addition of oxygen-containing groups increased the defect density on the graphite layer structure and degraded the packaging form of the graphite. This caused graphene oxide and different XRD spectra than graphite. Blue line pointed out $2\theta$ peak at 9° [61], as in GO.
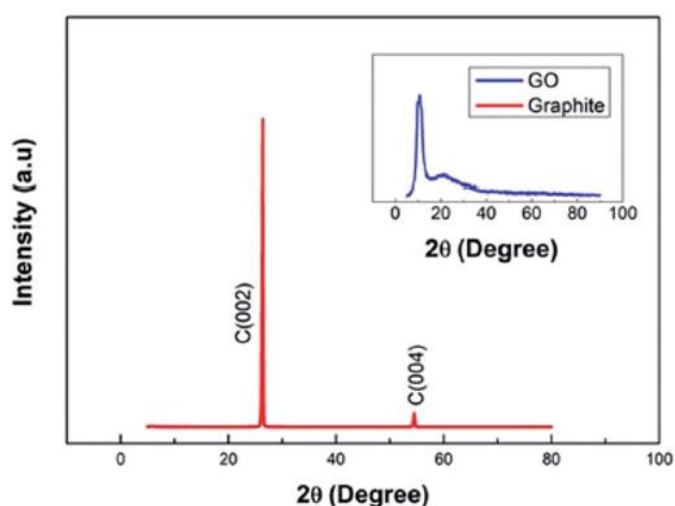


**Figure 4.1:** XRD analysis of graphite revealing (002) and (004) *hkl* planes and also GO showing $2\theta$ peaks of hydroxyl and carboxylic pendant groups at around 9° and graphene nanosheets at 23° [62].

The Raman analysis is done in Graphite and GO materials and is shown in Figure 4.2. Their peaks characterize graphite and GO when the Raman characterization is done. At 1350 cm$^{-1}$ D peak is found only in GO structure and not in graphite. $E_{2g}$ peak indicates the graphite layers. G peaks, for graphite and GO respectively, were seen at 1600 and 1650 cm$^{-1}$. The D and G peak intensities were calculated as ($I_D/I_G$) 0.8 and 1.04, respectively. Although the graphite peak at 2750 cm was completely removed from the GO spectrum, when compared graphite and GO, $I_D/I_G$ reveals that the density of functional defects is higher in GO. The reason for this is the increase in interlayer spacing. The increase in the distance between the layers and peaks are proof that we can produce graphene material from graphite material.
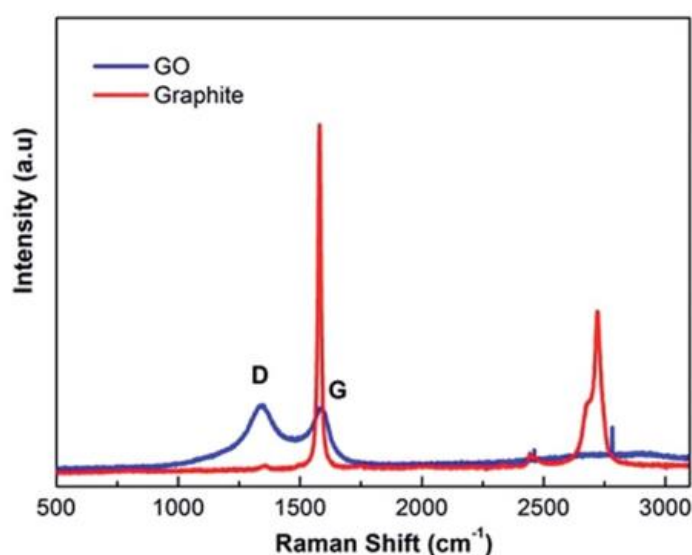


**Figure 4.2:** Raman spectra of graphite (G peak at 1550 cm$^{-1}$ and 2D peak at 2750 cm$^{-1}$) and GO (D peak at 1370 cm$^{-1}$ and G peak at 1550 cm$^{-1}$) [62].

The effect of different coagulation compositions and different GO concentrations on the structural and mechanical properties of the fibers were investigated by SEM. Coagulated GO fibers in the CaCl$_2$ coagulation bath (Figure 4.3a to d) showed higher packing density than GO fibers coagulated in NaOH (Figures 4.3f to h). On the other hand, as in the case of G40C5 and G40N5 fibers (Figures 4.3d and h), it was observed that increasing the GO content also increased the packing density. At such high GOLCs concentrations, metal ions in the coagulation bath played a role in GO layer alignment [25]. As expected, the surface topologies of low GO concentration fibers were significantly different from the fibers with high GO concentration. GO fibers produced from 20 mg mL$^{-1}$ (Figures 4.3a and e) and 25 mg mL$^{-1}$ suspensions (Figures 4.3b and f) exhibited wrinkles and irregularities. When GO concentration raised to 30

mg mL$^{-1}$ (Figures 3.4c and g) and 40 mg mL$^{-1}$ (Figures 4.3d and h), these loose and irregular features converted into full and highly aligned constructions. These densely packed fibers, as will be described in the next section, exhibited higher tensile strength and withstood tension and other stresses during the spinning. For this reason, successful fiber formation was observed even up to several meters in the higher GOLCs concentration.
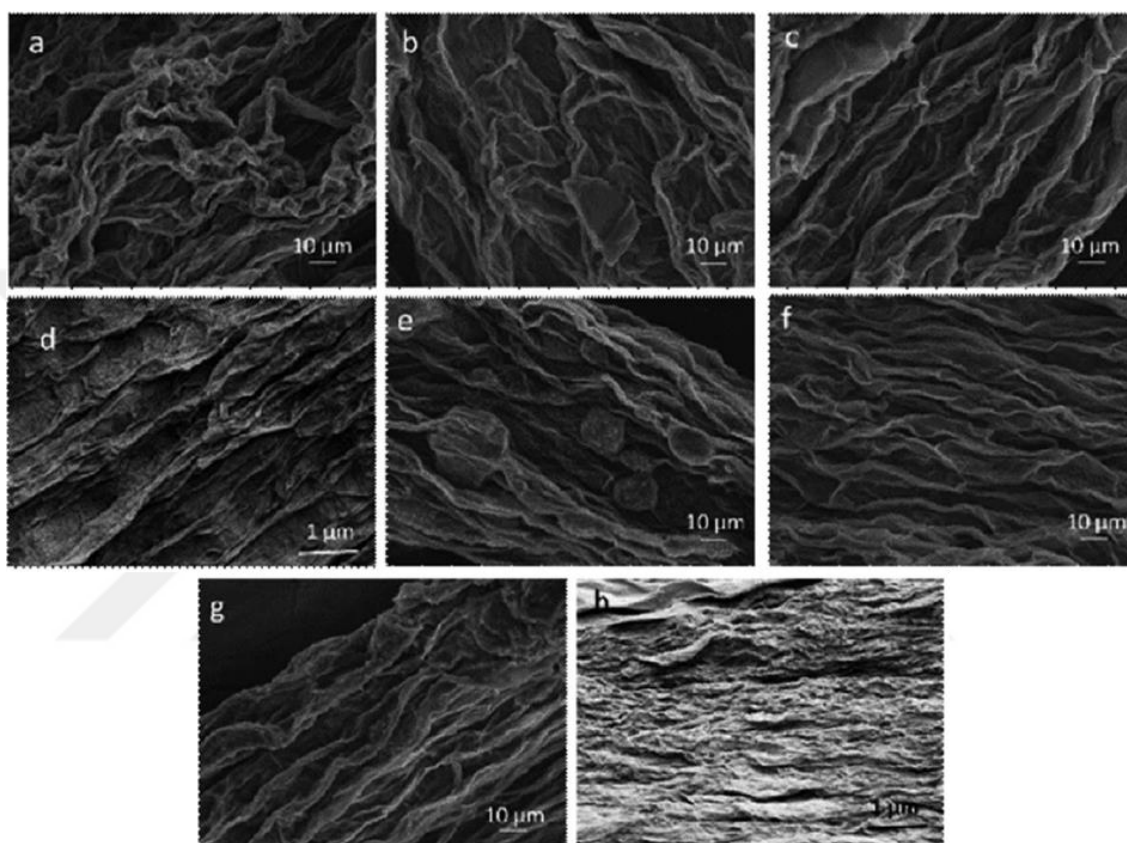


**Figure 4.3:** SEM images of as-spun (a) G20C5, (b) G25C5, (c) G30C5, (d) G40C5, (e) G20N5, (f) G25N5, (g) G30N5, (h) G40N5 coded GO fibers taken from their surfaces [62].

Figure 4.4 a and b show the fracture surfaces of G30C5 and G40C5 after tensile test respectively; wherein the G40C5 fibers have lower ductility than the G30C5 fibers. The GO concentration had no major effect on the tensile properties. The mechanical properties of the fibers significantly were affected by the packing density and hydrogen bonds formed during the coagulation process. The higher GO content per specific area reduced the plasticization and increased the fiber brittleness. These could be related to restricted void formation and stress concentration sites, that increase the strength while trading the ductility off.
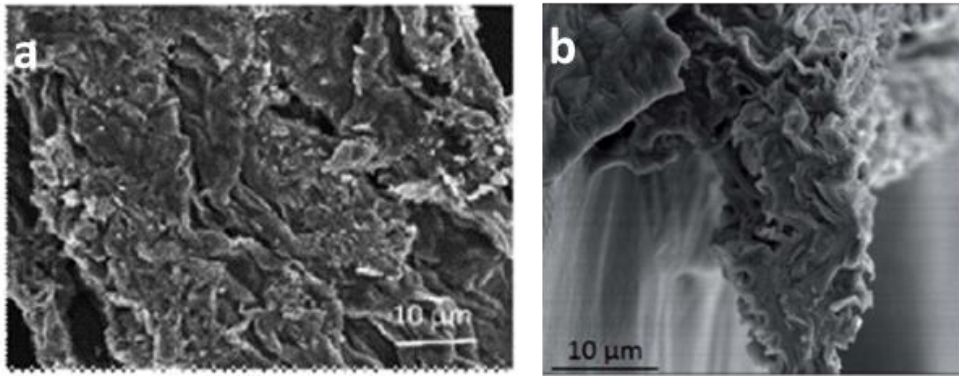
**Figure 4.4:** Fracture surface of as-spun (a) G30C5, (b) G40C5 fibers after tensile testing [62].

GO concentration, coagulation bath and applied tension in the yarn spinning step have a great influence on the properties of the yarn. Figure 4.5 and Figure 4.6 shows the tensile properties of 40 mg mL$^{-1}$ GO fibers and 30 mg mL$^{-1}$ GO fibers coagulated in CaCl$_2$ and NaOH baths at different concentrations. Table 4.1 shows the results of mechanical properties of GO fibers. Strain to failure, specific ultimate strength (N/tex) and specific modulus (N/tex) were calculated for each GO fiber. In addition to the Table 4.1, fiber diameters measured by an optical microscope are provided. Due to the crumbled structure, the fiber cross-section may differ in different fiber sets. For each fiber, the specific strength (N/tex) was calculated to eliminate this diameter effect seen due to different ion diffusion mechanism.

Tensile properties of CaCl$_2$ and NaOH coagulated GO fibers showed that CaCl$_2$ coagulated GO fibers had strain to failure of 10%. Fibers coagulated in 5% CaCl$_2$ bath exhibited higher specific strength than the ones coagulated in 3% CaCl$_2$ bath. Specific strength of G40C5 fibers was 4 times higher than G40C3 fibers while specific strength of G30C5 fibers was 2 times higher than G30C3 fibers. G30C5 had best strain to failure (%) values. In comparison with the 5% and 3% concentrations of the fibers coagulated in NaOH bath, there was no clear difference in terms of specific strength. When GO fibers coagulated in 5% and 3% NaOH concentrations were compared, specific strength values seemed similar. Moreover, the concentration of 3% NaOH coagulation bath provided results better strain to failure (%) while G40N5 became prominent in terms of their strength.
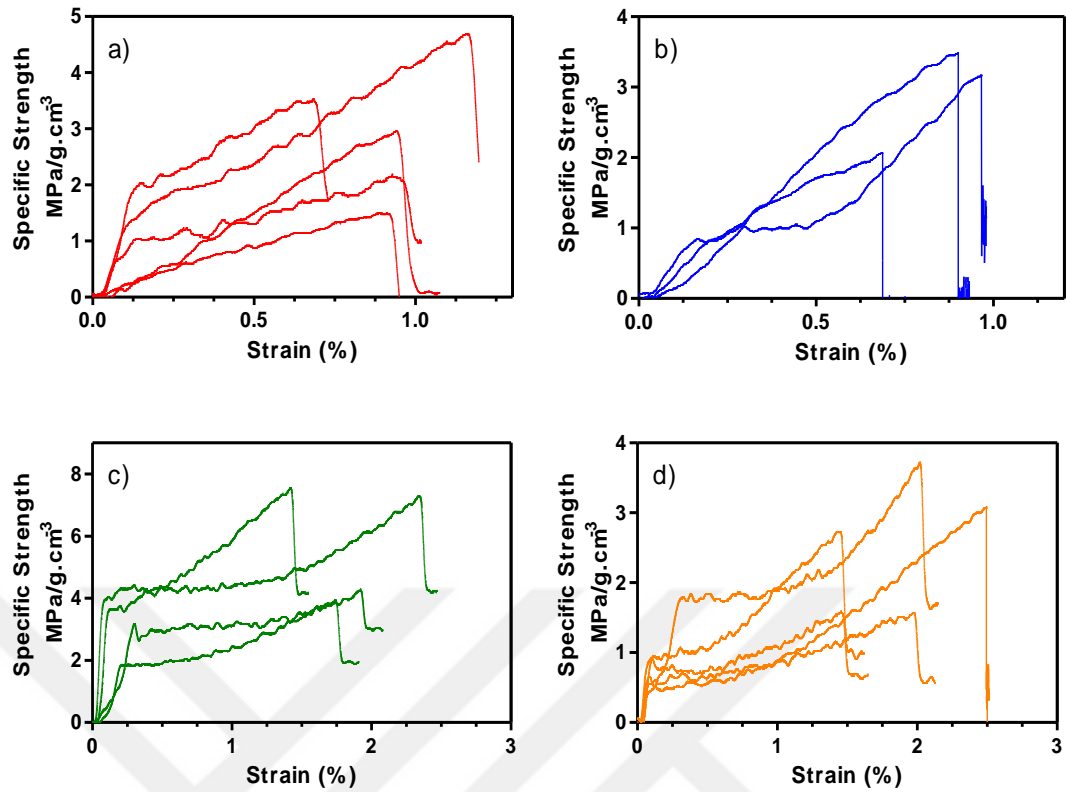
**Figure 4.5:** Specific Strength (N/tex) - Strain to failure (%) curve of (a) G30N5, (b)G40N5, (c) G30N3 and (d) G40N3 GO coded fibers.

Fiber diameters were varied by coagulation bath and GO concentration due to the changes in packing density. Hence, cross-sectional area of each fiber set was changed. In order to provide clear comparison, specific strength and modulus data was calculated by yarn count (tex). This approach also enabled us make comparison to the reported values in literature. Table 4.1 shows the specific modulus (N/tex) data of the GO fibers in the literature and GO fibers in this thesis. Xiang et al. investigated the tensile properties of GO fiber produced at different drawing ratio applied during wet spinning stage [30]. Drawing ratio contributed to the mechanical properties, especially the specific modulus of GO fiber. In this thesis, GO fibers exhibited super strain to failure (%) and specific strength, whereas specific modulus of these fiber was lower than the ones in reference studies. It should be noted that in ref [30], fiber diameters were much finer than the ones in this thesis. Applying controlled drawing also assisted reducing fiber diameter. Nevertheless, this thesis did not aim to produce super-fine GO fibers.
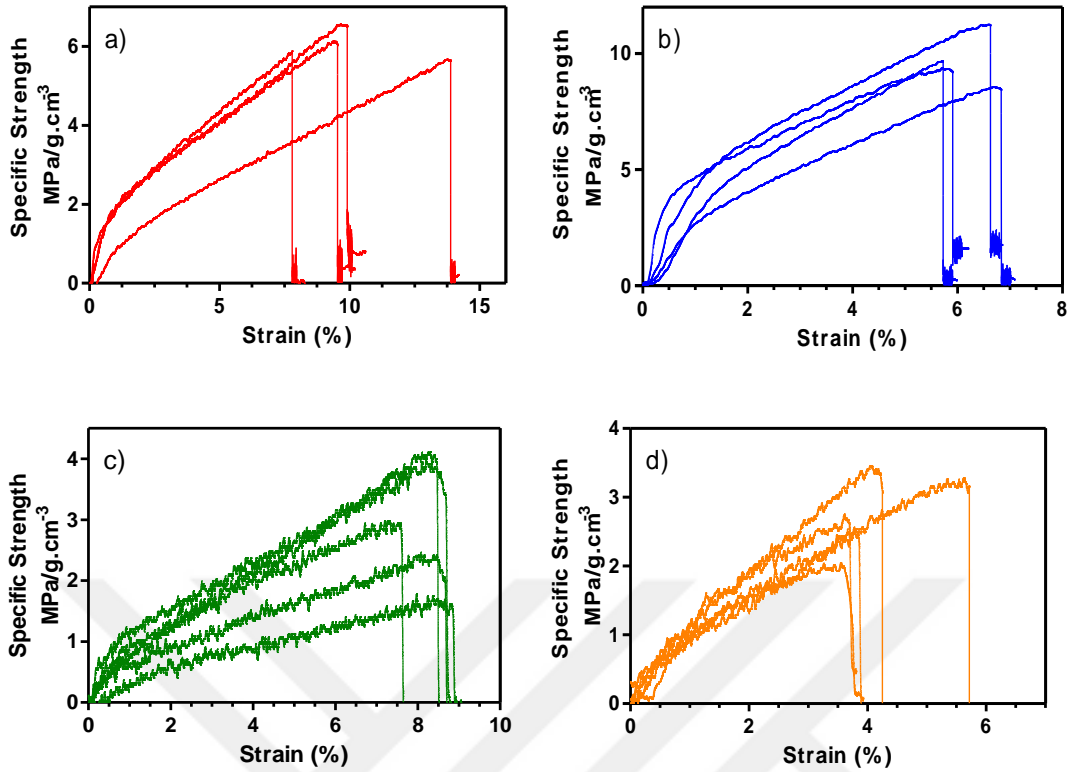
**Figure 4.6:** Specific Strength (N/tex) - Strain to failure (%) curve of (a) G30C5, (b)G40C5, (c) G30C3 and (d) G40C3 GO coded fibers.

**Table 4.1:** Comparison of the mechanical properties of the produced graphene and GO fibers with the literature.

| GO Fiber | Diameter (µm) | Strain to Failure (%) | Specific Ultimate Strength (N/tex) | Specific Modulus (N/tex) |
|---|---|---|---|---|
| G30C5 | 130 | 10±2.1 | 7±0.5 | 5.7±2.8 |
| G40C5 | 130 | 6.7±0.5 | 5.9±1.3 | 4.3±0.8 |
| reduced G30C5 | 229 | 4.7±0.5 | 4.5±2 | 8.3±2.2 |
| reduced G40C5 | 271 | 2.8±1.7 | 14.5±0.4 | 20±2.2 |
| G30N5 | 189 | 1.3±0.2 | 5.8±1.5 | 12.2±8.5 |
| G40N5 | 203 | 0.9±0.1 | 6.4±0.7 | 4.8±2.5 |
| GO fiber (draw ratio 1.09) [30] | 26 | 1.64±0.12 | 1.04±0.006 | 10±1.6 |
| GO fiber (draw ratio 1.27) [30] | 26 | 0.84±0.08 | 1.26±0.013 | 20±0.6 |
| GO fiber (draw ratio 1.45) [30] | 26 | 0.61±0.10 | 1.56±0.022 | 41±3.5 |
| Reduced GO fiber [69] | 240 | 1.5 ±0.1 | 1.02±0.03 | 50.8±1.9 |

Overall, as seen in Figure 4.7, higher GO concentration increased the tensile strength of GO fibers due to stacking. For further examination, fibers coagulated in $CaCl_2$ coagulation bath was preferred due to superior strain to failure (%) and ultimate strength. For instance, if we compared G40C5 and G40N5 fibers, G40C5 fibers had 2 times higher ultimate strength and 5 times higher strain to failure (%) than G40N5 fibers. $CaCl_2$ coagulation bath due to bivalent $Ca^{2+}$ ions provided better stacking and finer fibers. These mostly based on the interaction between the divalent metal ions ($Ca^{2+}$) and the carboxylic groups of the GO nanosheets. The divalent ions were easily penetrated into the fibers, thus reacting with the functional domains in the GO layers. As a result, the toughness of fibers were developed [70]. The presence of $Ca^{2+}$ ions in GO layers caused compact but crumbly intrinsic morphologies and eventually finer fibers were formed. As the number density of the contact points between each nanosheet was increased, it led to higher ultimate strain (%) and assisted the plastic deformation mechanism. However, NaOH coagulation also promoted the reduction of the possibility of hydrogen bonding between the functional groups of the GO layers to partial reduction [10, 71].
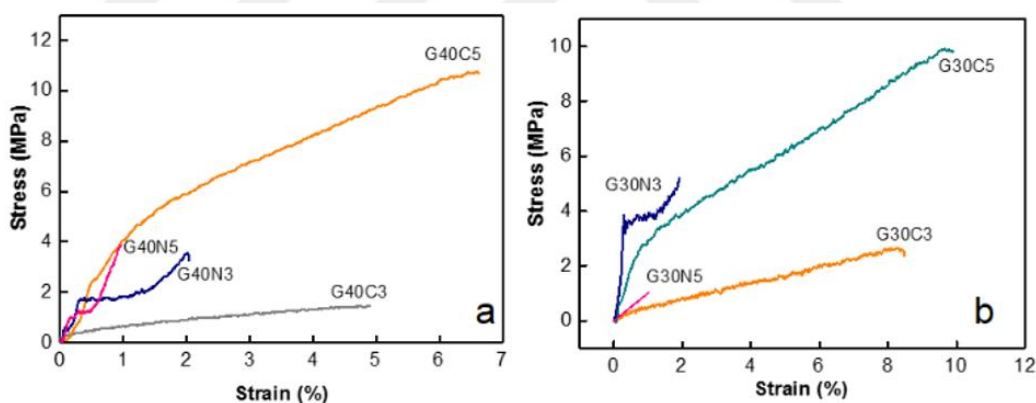


**Figure 4.7:** a) Stress($\sigma$)-strain ($\varepsilon$) curve of 40 mg mL$^{-1}$ GO coded fibers and b) Stress($\sigma$) - strain ($\varepsilon$) curve of 30 mg mL$^{-1}$ GO coded fibers [62].

## 4.2 Graphene Fiber

GO fibers are not electrically conductive; hence reduction of GO is required to conduct electrons. In this thesis, NaBH4, AA and HI reduction agents were investigated in terms of their effect on mechanical properties. First, the success of chemical reduction was examined by Raman analysis. The results showed that D peak was found at 1350 cm$^{-1}$ at GO structure while G peaks exhibited at 1650 cm$^{-1}$. Structural defects and the

degree of reduction could be detected also by Raman spectroscopy. $I_D/I_G$ ratio of GO fiber and reduced graphene fibers were given in Figure 4.8. When $I_D/I_G$ ratio of GO and reduced GO fibers were compared, it is clear that functional groups in graphene sheets were eliminated. As suggested in Figure 4.8, NaBH$_4$ reduction agent ($I_D/I_G$=0.53) is the most successful chemical to eliminate these oxide groups as structural defects.
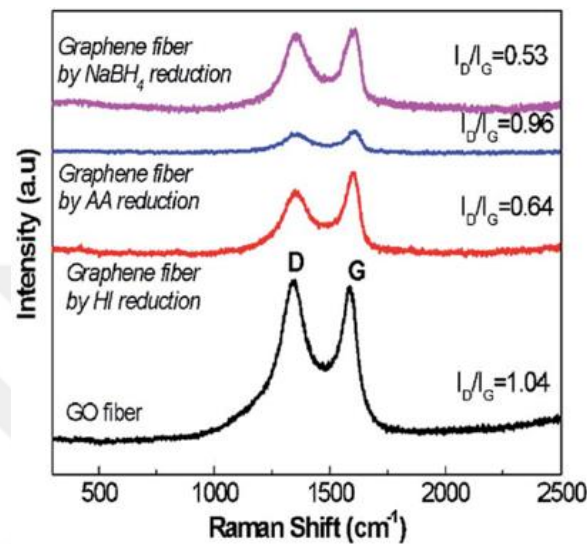


**Figure 4.8:** Raman spectra of GO and graphene fibers reduced by NaBH$_4$, AA and HI agents revealing D peak at 1370 cm$^{-1}$ and G peak at 1550 cm$^{-1}$ [62].

Herein, this thesis also aimed to reach possible highest electrical conductivity by NaBH$_4$ reduction. First, the changes in electrical conductivity depending on the reaction time was investigated. Different time intervals for reduction were tested as shown in Figure 4.9a. It was decided that the 24 hour reduction period would be sufficient for optimum electrical conductivity [72]. However, the highest electrical conductivity was reached by NaBH$_4$ reduction (73 S/cm) after 72 hours.

Next, the effect of reduction temperature on electrical conductivity was investigated. The conductivity results of the reduced fibers by NaBH$_4$ at 30, 60 and 90 °C were measured in Figure 4.9b. The reduction at 90 °C provides about 3 times higher electrical conductivity compared to reduction at 30 °C and 60 °C. Also, the highest conductivity value was 255 S/cm with NaBH$_4$ reduction at 90 °C for 72 hours. The graphene fibers exhibited semiconductor characteristics as shown in Figure 4.9b. As the temperature increased, the conductivity increased while the resistance decreased. The valence band electrons passed through the conductivity band when the

temperature increased, which was associated to the temperature-induced excitation of electrons.

Finally, the effect of the NaBH$_4$ concentration on the conductivity was examined. The experiment was carried out at the optimum value of 24 hours at 90 °C. The NaBH$_4$ concentration range from 0.3 M to 2.4 M was studied. Figure 4.9c gave the highest electrical conductivity along the fiber axis to the 2.4M NaBH$_4$ concentration (214 S/cm). It was noted that the high conductivity in graphene fibers is due to the increase in reduced sites. In addition, this effect minimized contact resistance while maintaining fiber structure. Due to well combination of properties including good flexibility, high tensile strength and conductive properties of the graphene fibers are emerging materials for wearable functional textile products. In the next section, tensile properties of G30C5 and G40C5 fibers reduced at 24 hours at 90 °C with 2.4 M NaBH$_4$ was investigated.
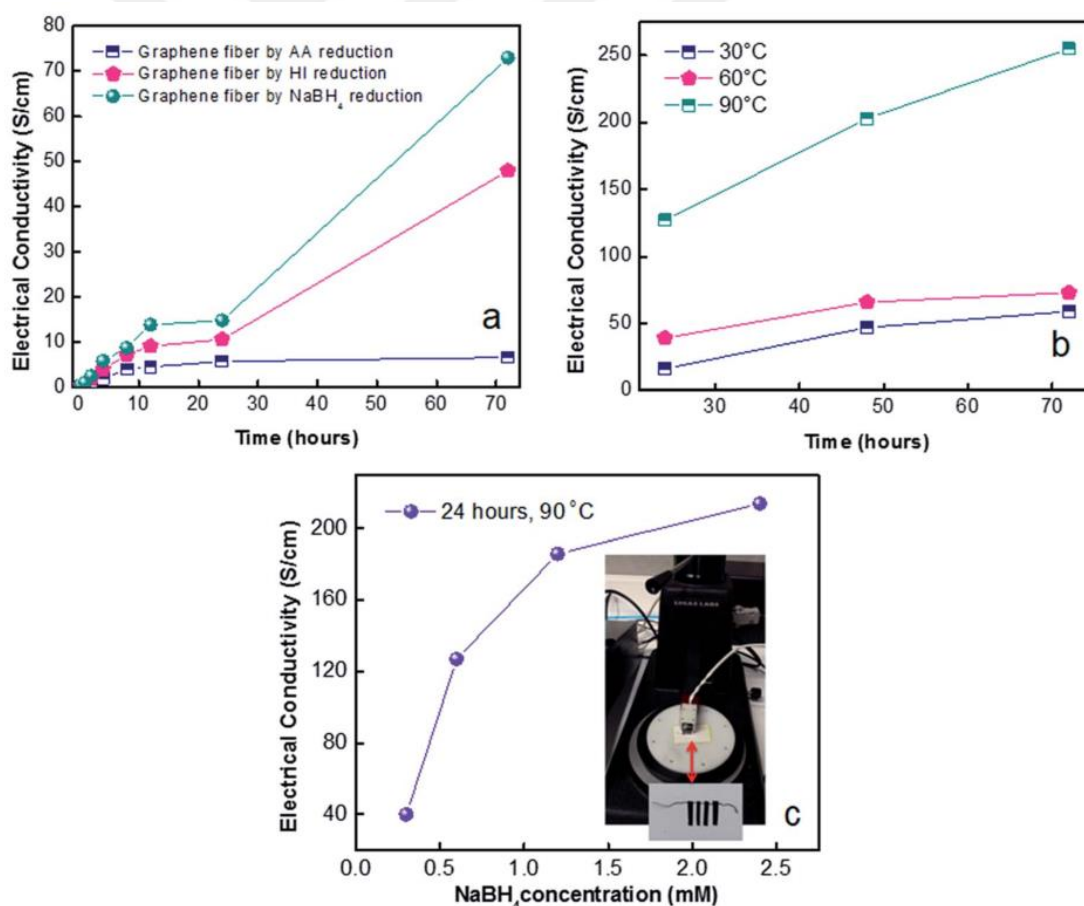


**Figure 4.9**: Investigation of the electrical conductivity of graphene fibers (a) the reducing agent and the reaction time, (b) Effect of NaBH$_4$ (1.2 M) reduction temperature on electrical conductivity, (c) Effect of NaBH$_4$ concentration on electrical conductivity [62].

Tensile testing was performed to observe the effect of the reduction process on mechanical behavior in reduced graphene fibers. Figure 4.10 and Figure 4.11 shows the results of the tensile properties of GO fibers such as G30C5 and G40C5 fibers and their reduced graphene fibers. Table 4.1 also shows that these reduced fibers' ultimate tensile strength and strain to failure (%). First, we examined the effect of the reduction process on the change of strain to failure (%). $NaBH_4$ reduction led to swelling in the fibers, while also formed brittle fibers. After the reduction process, poor network structure that prevented graphene layers from slipping may occur. This structure described the change in ductility of the fiber. The specific strength could be increased or decreased depending on the GO density. The reduced G40C5 graphene fiber ultimate strength was observed to be greatly affected by reduction process. However, a slight decrease in the reduced G30C5 graphene fibers was observed. The presence of larger number of reduction domains resulted in structural differences in the fibers. In addition, the specific stress of reduced G30C5 graphene fibers was higher than G30C5 fiber. The mechanical properties of reduced GO fibers were also studied by Chen *et al*. [69] and these data are provided in Table 4.1. Among the literature, this thesis's results on reduced GO fibers gave better results. However, the specific modulus value was lower than the reported values in literature.
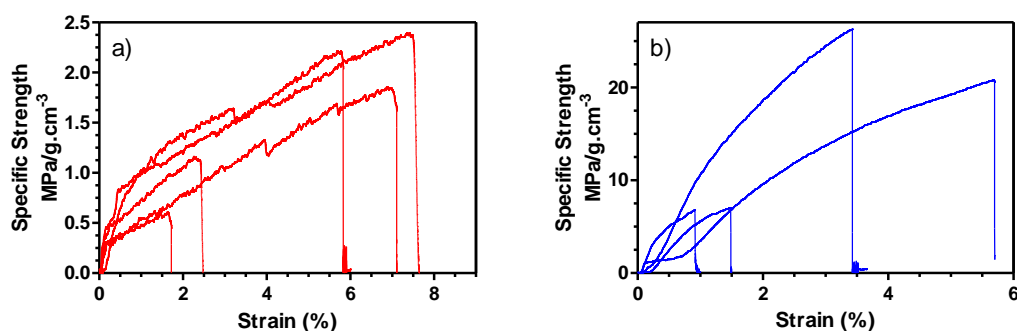


**Figure 4.10:** Specific Strength (N/tex) - Strain to failure (%) curve of (a) G30C5 and (b) G40C5 graphene fibers.
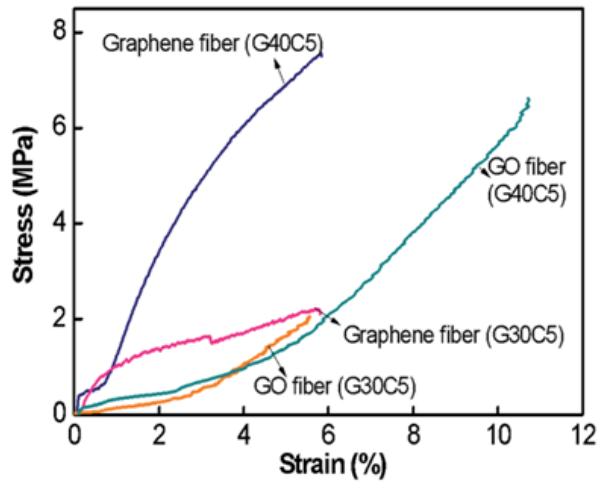
**Figure 4.11:** Stress ($\sigma$)–strain ($\varepsilon$) curves of G30C5, G40C5 GO fibers and reduced G30C5 and G40C5 graphene fibers [62].

## 4.3 CNTs Fiber

CNTs fibers are another type of carbon nanomaterial based fibrous structures, that mechanical properties are strongly dependent on fabrication methods. For dry spun CNTs fibers, spinnability changes with the height, morphology and growth conditions of CNTs forest. The spinnability standard ranging from 0 to 10 was created to describe dry yarn spinning [73]. Table 4.2 explains this standardization. Synthesized CNTs forests and fibers were compared according to this table. The first goal of the thesis is reach the ranking of 3 or higher value to spin CNTs fiber.

In the earlier studies, more promising growth was obtained with the $SiO_2$ free wafers (P-type <100> Si wafer, $Al_2O_3$ ~10 nm and Fe ~2nm). Thus, CNTs synthesis protocol optimizations were done as explained in the previous section Chapter 3.2.2.2. Table 4.3 describes the characterization of CNTs arrays based on this protocol. First, the length of the CNTs forests were measured by the stereomicroscope as shown in Figure 4.12. The changes in length of CNTs were monitored by gradually reducing the growth time. The C-3 (9 min growth) seemed to be available, but it was not enough when spinning with the tweezers. Then $H_2$ and $C_2H_4$ gases were optimized. C-6 became prominent. During spinning, short fiber could be pulled unfortunately they were separated into chunks. Thus, these arrays were not enough for spinning. The quality of CNTs forests were also examined by Raman spectroscopy, besides defining their spinnability index.

**Table 4.2:** Description and ranking of CNTs array spinnability [74].

| Rank of Spinnability | Description |
|:---:|:---:|
| 10 | Fiber can be spun continuously and uniform |
| 9 | Fiber length>1 m, and spinning success rate is high |
| 8 | Fiber length>1 m, but spinning success rate is low |
| 7 | Fiber length: 50-100 cm |
| 6 | Fiber length: 20-50 cm |
| 5 | Fiber length: 10-20 cm |
| 4 | Fiber length: 5-10 cm |
| 3 | Can spin fibers, but fiber length <5 cm |
| 2 | Cannot spin fiber, but could pull out small ribbons |
| 1 | Cannot spin fibers, soft array |
| 0 | Cannot spin fibers, hard array |

The presence of defects as indicator of CNTs quality can be measured by Raman spectroscopy. The defects in CNTs structure called 'D-band' gave its peak at around $1331 cm^{-1}$. The graphitization of CNTs had the fingerprint peak around $1584 cm^{-1}$, which is called 'G-band' [75]. These peaks and their intensities varied with the graphene form in the structure. The higher ratio of $I_G/I_D$ indicated less defects so better synthesis quality since amorphous carbon deposition was another parameter for growth yield. Shorter growth time reduced the amount of amorphous carbon as interpreted by high $I_G/I_D$ ratio in Raman analysis. Overall, CNTs with less defects were synthesized by using the proposed protocols as shown in Table 4.3.

SEM micrographs were examined to understand the inner morphological structure of CNTs forests. Figure 4.13 demonstrates the morphologies of C-6 CNTs forests, which pointed out waviness in CNTs arrays. Areal density, CNTs waviness and van der Waals forces were well-known factors which affected the spinnability of CNTs fibers. Moreover, addition to intrinsic waviness of CNTs, non-linear intermediate CNTs fibers were also detected. To conclude, C-set CNTs forests were not fully uniform at mesoscale, so the spinnability was quite low for yarn production.

**Table 4.3:** $I_G/I_D$, spinnability index and length of C-sets of CNTs forests.

| Sample Name | $I_G/I_D$ | Length (μm) | Rank of Spinnability |
|---|---|---|---|
| C-1 | 2.43 | 1234.6 ± 8.9 | 1 |
| C-2 | 3.22 | 71.4 ± 6.5 | 1 |
| C-3 | 2.02 | 553.5 ± 18.4 | 2 |
| C-4 | 1.94 | 483.5 ± 13.2 | 1 |
| C-5 | 2.71 | 342.1 ± 7.4 | 1 |
| C-6 | 2.57 | 758.5 ± 17.4 | 2 |
| C-7 | 2.52 | 812.8 ± 3.4 | 1 |
| C-8 | 2.62 | 612.3 ± 11.8 | 1 |
| C-9 | 2.27 | 757.4 ± 9 | 0 |
| C-10 | 1.89 | 602.2 ± 12.2 | 0 |
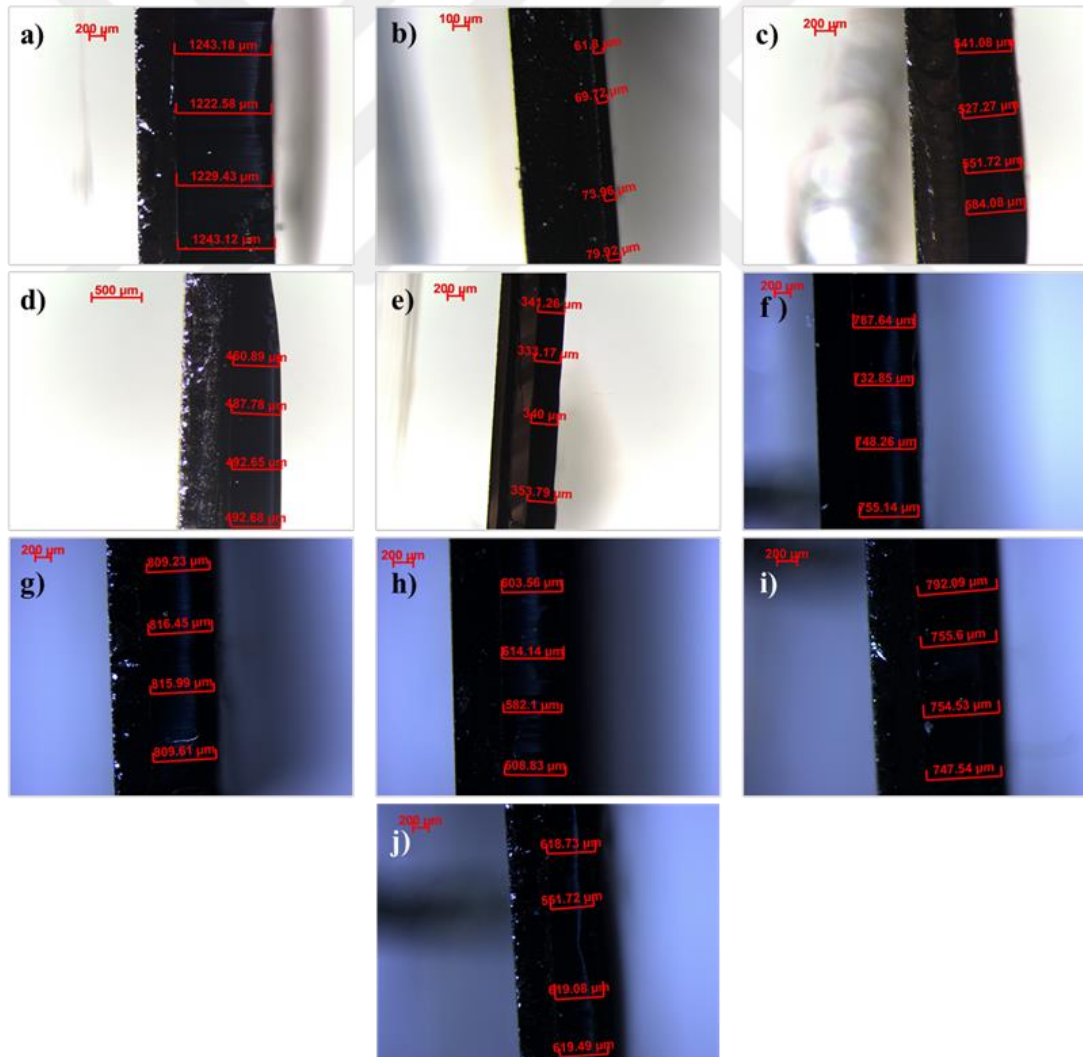


**Figure 4.12:** Stereomicroscope images of C set of CNTs forests. (a) C-1, (b) C-2, (c) C-3, (d) C-4, (e) C-5, (f) C-6, (g) C-7, (h) C-8, (i) C-9, (j) C-10.
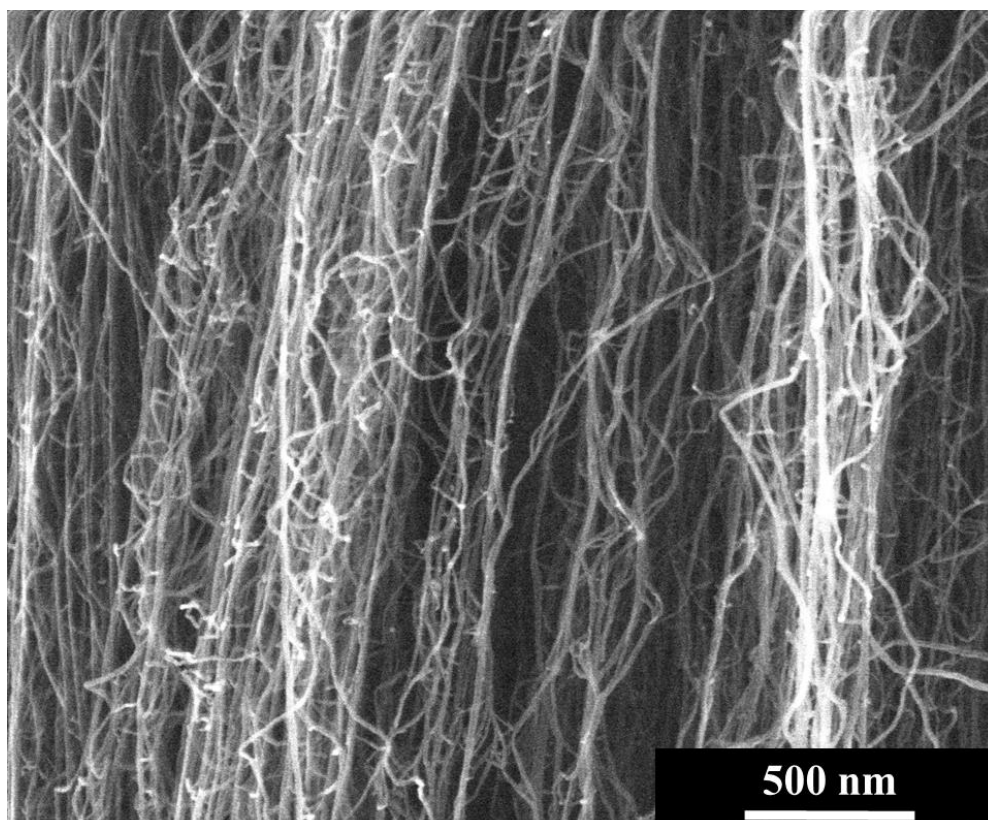
**Figure 4.13:** SEM images of C-6 CNTs forest.

Recent studies showed that as in small quantities, the presence of controlled oxygen significantly increased the reaction efficiency. The oxygen swept the amorphous carbon from the system and assisted to produce longer CNTs [65]. For this set of materials, CNTs synthesis protocol optimizations were done as explained in the previous section Chapter 3.2.2.2. Table 4.4 describes the characterization of CNTs arrays based on this protocol. First, the length of the CNTs forests were measured by the stereomicroscope as shown in Figure 4.15. The growth time was gradually increased. The growth rate was calculated to determine the optimum duration time as shown in Table 4.4. CNTs longer than 7 cm could be synthesized but the growth rate was started to fall in growth time longer than 60 minutes (see W-4, W-7, W-8, W-10, W-11 and W-12 protocols). Whereas the spinnability of CNTs was still low with longer growth periods. Synthesized CNTs forests had lost their flexibility and were converted into hard blocks as in the case of W-11 and W-12. Spinnable optimum growth was only seen in W-7 and W-8 samples. After the optimization of $H_2$ and $C_2H_4$, W-9 and W-10, were used for spinning with tweezers. Unfortunately, spinnability was still low for W-9 and W-10.

Studies showed that shorter nucleation step resulted in the best spinnability index in CNTs synthesis. As well as longer nucleation led to irregular CNTs [66]. The reason of this, after the nucleation was completed, when waited longer, the catalyst Fe materials recombined and formed a uniform nucleation sites. Table 4.4 also shows the changes in nucleation step and their effect on physical properties. No clear effect was observed on the spinning index when nucleation was reduced from 15 min to 10 minutes. It was seen that the 15-min nucleation step for the used wafer was ideal.

In addition, Figure 4.14 showed the spinning of the W-7 with tweezers. Short fibers could be spun and twisted. However, the fibers were bundled and not good enough for the implementation in dry spinning device.

Raman analysis was performed to determine $I_G/I_D$, which indicated the quality of synthesis. Generally, synthesized CNTs were in good quality when $I_G/I_D$ ratio was examined. The reduction of $H_2$ ratio in the system did not significantly change the quality, such as sample W-4 and W-6 or W-7 and W-9. Nevertheless, the quality decreased ($I_G/I_D$ ratio) as the growth time increased as seen in samples W-11 and W-12 due to increased amorphous carbon in the structure.

SEM micrographs were examined to understand the inner morphological structure of W-CNTs forests in Figure 4.16. W-7, W-8 and W-10 are specimens in which the growth time was higher. In W-7 and W-8, CNTs forests were regular and linearly oriented structures. These two structures were more promising for CNTs yarn spinning. However, W-8 had fewer small bundles. According to W-10 SEM images, CNTs waviness was higher than W-7 and W-8. For this reason, these samples could not be used for spinning. These deteriorated morphologies due to the accumulation of amorphous carbon was seen in synthesis with longer growth periods [76]. . Compared to W-7 and W-9, both of them were quite regular and linearly oriented but W-9 had fewer capillary CNTs. The only difference between them was the amount of $H_2$. In the CNTs synthesis, $H_2$ gas assisted catalyzation process. $H_2$ atoms combined with $H_2$ of the $C_2H_4$ structure and carbon atoms were released. If the amount of $H_2$ given to the system decreased, the amount of free carbon was reduced. As a result of this, the system efficiency was reduced. This phenomenon could be associated to the observed decrease in the small bundles as in W-9 production.

**Table 4.4:** $I_G/I_D$, spinnability index and length of W-sets of CNTs forests.

| Sample Name | $I_G/I_D$ | Length (μm) | Growth Rate (mm/min) | Rank of spinnability |
|---|---|---|---|---|
| W-1* | - | 1195.1 ± 16 | 0.0797 | 1 |
| W-2* | - | 1533.3 ± 30.1 | 0.1022 | 1 |
| W-3* | - | 2088.4 ± 5 | 0.1392 | 1 |
| W-4 | 2.23 | 1894.4 ± 11.8 | 0.1263 | 1 |
| W-5 | 2.08 | 2017.3 ± 1.3 | 0.1345 | 1 |
| W-6 | 2.23 | 1719.4 ± 15.8 | 0.1146 | 2 |
| W-7 | 1.79 | 3534.9 ± 287.1 | 0.1178 | 2 |
| W-8 | 1.51 | 4718 ± 129.1 | 0.0786 | 2 |
| W-9 | 1.64 | 3842.6± 81.8 | 0.1281 | 1 |
| W-10 | - | 4796 ± 47.2 | 0.0533 | 1 |
| W-11 | 1.71 | 7667.9 ± 11.2 | 0.0639 | 0 |
| W-12 | 1.31 | 5236.7 ± 139.2 | 0.0349 | 0 |
| W-13 | - | 3550.7 ± 74.4 | 0.0592 | 1 |
| W-14 | - | 1754.3 ± 23.2 | 0.1170 | 1 |
| W-15 | - | 2232.3 ± 20 | 0.0744 | 1 |
| W-16 | - | 1723.2 ± 19.6 | 0.0287 | 1 |
| W-17 | - | 1645.4 ± 52.5 | 0.1097 | 1 |
| W-18 | - | 1889.3 ± 65.2 | 0.0630 | 1 |

* There is easy delamination step in the protocol.
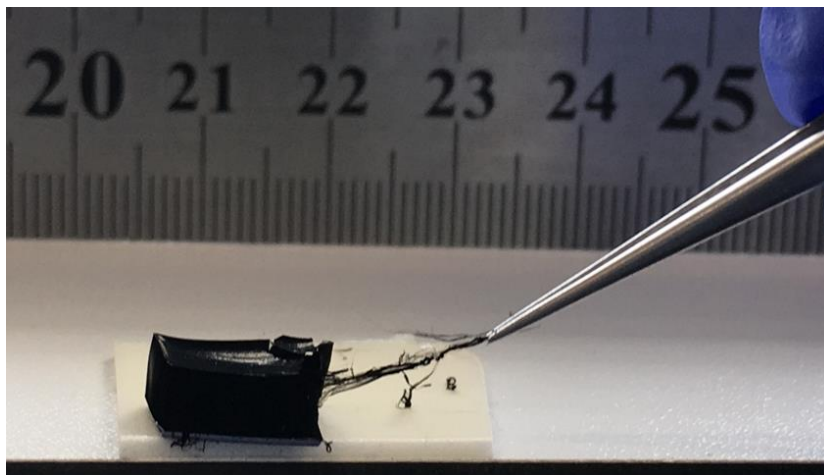


**Figure 4.14:** The spinning of the W-7 set with tweezers.
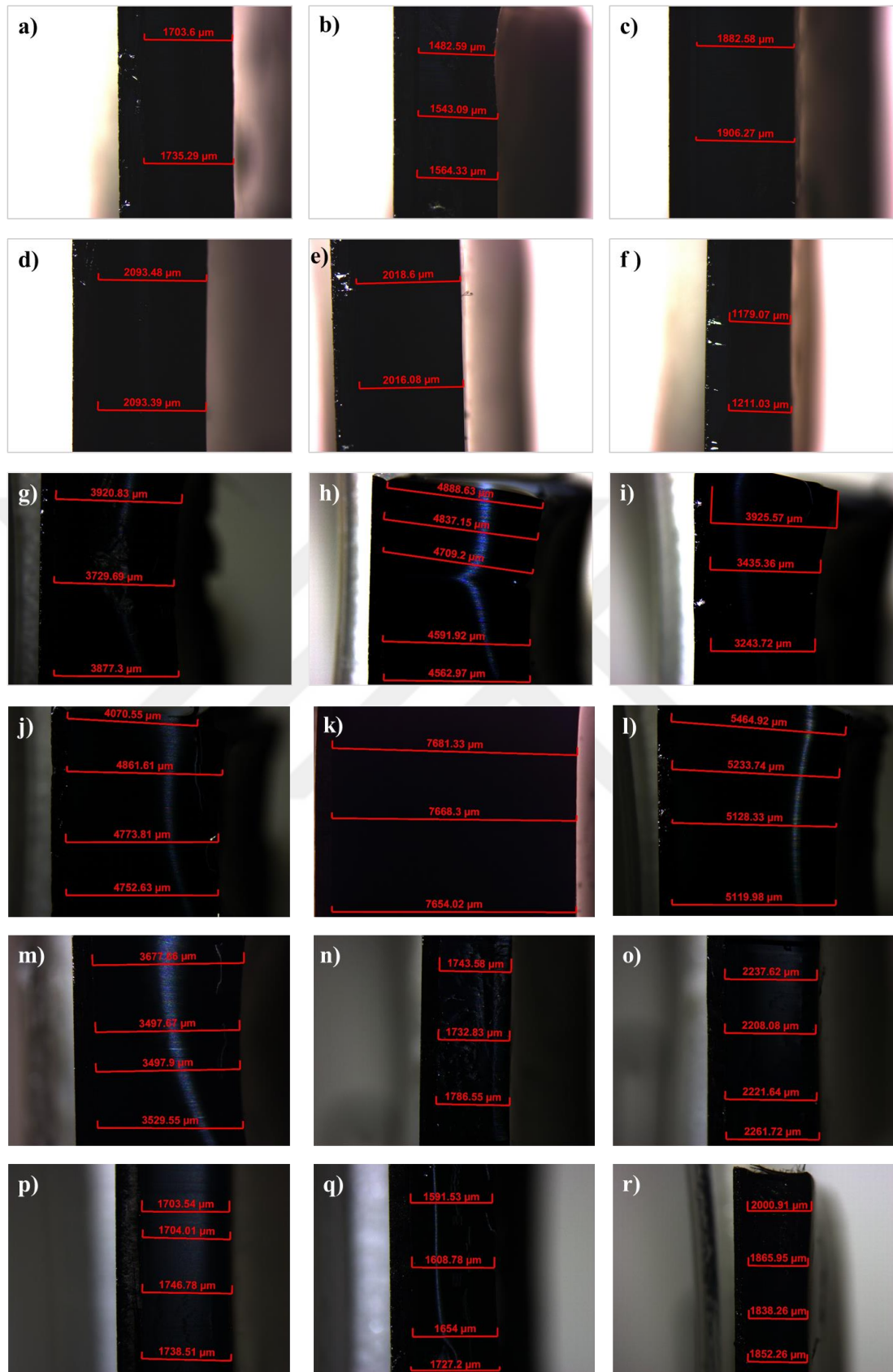
**Figure 4.15:** Stereomicroscope images of W set of CNTs forests. (a) W-1, (b) W-2, (c) W-3, (d) W-4, (e) W-5, (f) W-6, (g) W-7, (h) W-8, (i) W-9, (j) W-10, (k) W-11, (l) W-12, (m) W-13, (n) W-14, (o) W-15, (p) W-16, (q) W-17, (r) W-18.
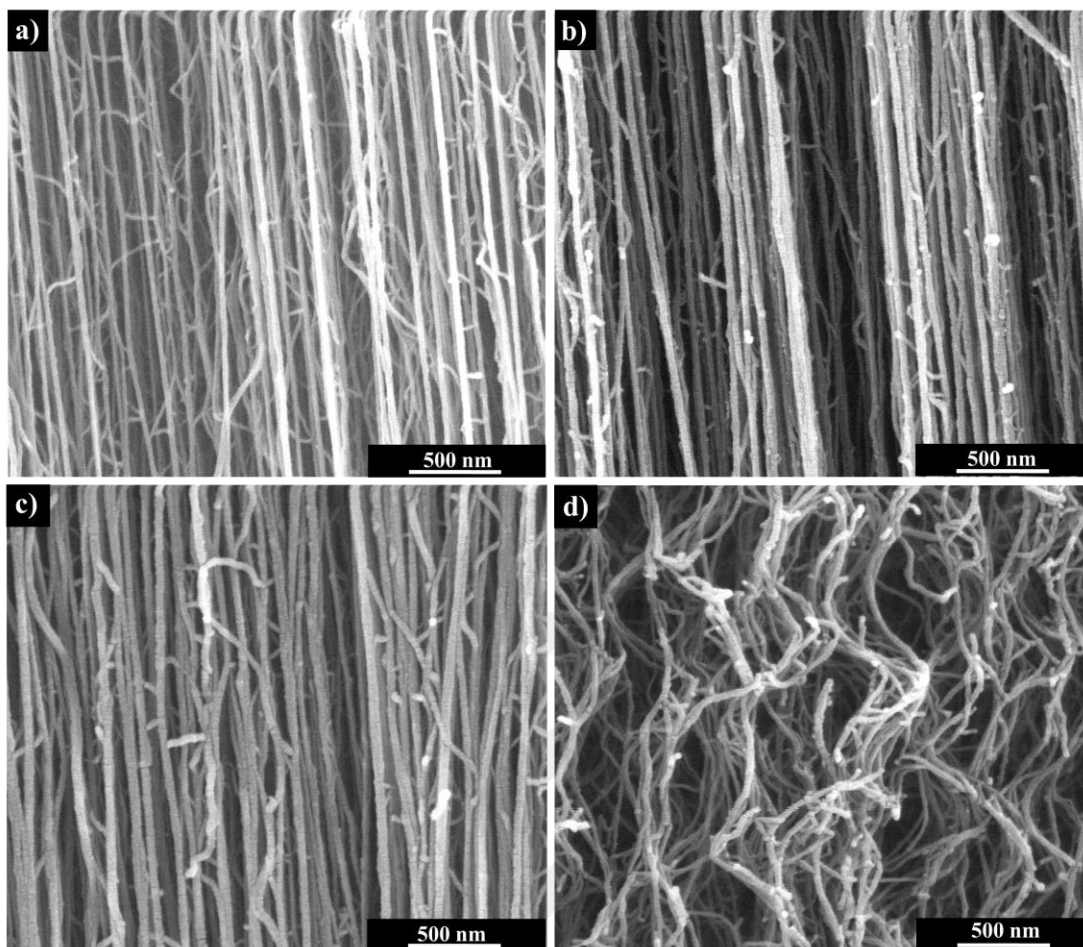
**Figure 4.16:** SEM images of (a) W-7, (b) W-8, (c) W-9 and (d) W-10 CNTs forest.

Super aligned CNTs with high density were essential in dry spinning. This structure could be succeeded with larger nucleation Fe particles by increasing the catalyst ratio [64]. First, new set of protocols inspired from the studies in literature were designed as explained in the previous section Chapter 3.2.2.2. Table 4.5 describes the characterization of CNTs arrays based on this protocol. First, the length of the CNTs forests were measured by the stereomicroscope as shown in Figure 4.17. The results showed that CNTs surface became rough and inconsistent growth occurred. Increasing the nucleation time could be beneficial to overcome this uneven growth. Focused on the morphology and length, 25 min was used as nucleation time. However, when the growth period was increased, still even growth could be achieved. Table 4.5 also displays the growth rate for each specimen in T-set. The water vapor passing through the system might be insufficient, hence it was increased next. It was seen that the ratio of 750:250 He in $H_2O$:He was optimum. In T-7 and T-9 sets, longer CNTs were synthesized.

**Table 4.5:** $I_G/I_D$, spinnability index and length of T-sets of CNTs forests with thicker Fe coating and assisted water vapor

| Sample Name | $I_G/I_D$ | Growth Rate (mm/min) | Length (μm) | Rank of spinnability |
|:---:|:---:|:---:|:---:|:---:|
| T-1 | - | - | - | 0 |
| T-2 | 1.18 | 0.0991 | 1486.6 ± 17.9 | 1 |
| T-3 | 1.22 | 0.1050 | 1574.8 ± 49 | 1 |
| T-4 | 1.26 | 0.1006 | 1508.7 ± 48.9 | 1 |
| T-5 | 1.11 | 0.0302 | 906.2 ± 35.3 | 2 |
| T-6 | 1.25 | 0.0879 | 878.9 ± 21.3 | 1 |
| T-7 | 1.21 | 0.0963 | 1445.1 ± 9.6 | 1 |
| T-8 | 1.26 | 0.0652 | 978.4 ± 7.2 | 1 |
| T-9 | 1.26 | 0.0661 | 1982.6 ± 33.6 | 1 |
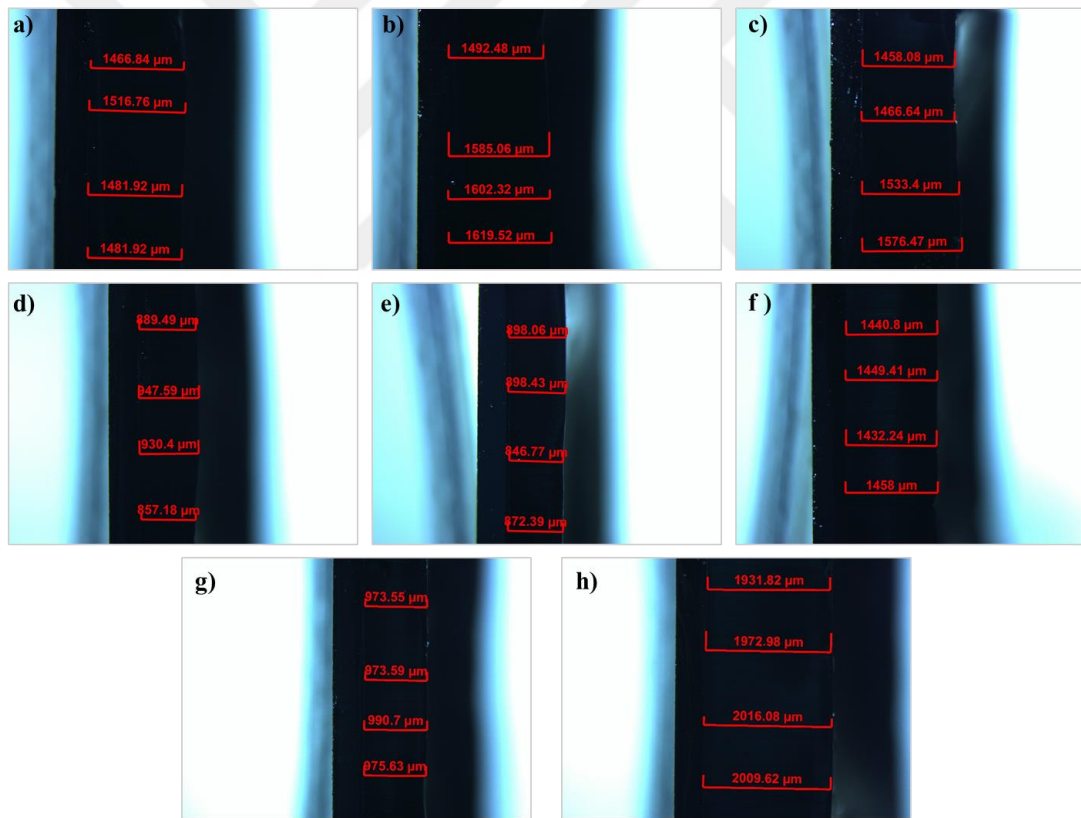


**Figure 4.17:** Stereomicroscope images of T set of CNTs forests. (a) T-2, (b) T-3, (c) T-4, (d) T-5, (e) T-6, (f) T-7, (g) T-8, (h) T-9

Preliminary spinning trials were done manually with tweezers and indicated that these set of CNTs were not optimum enough for spining. Figure 4.18 shows the spinning of T-5 with tweezers. CNTs fibers could be held together and be twisted. However, it was quite delicate, as shown in Figure 4.18. These fibers could be continuously spun in dry spinning device.

Raman analysis demonstrated that $I_G/I_D$ ratio of T-sets were slightly lower than C and W sets. In addition, optimization on the volume of gases, nucleation and growth steps dis not make a big difference in quality.
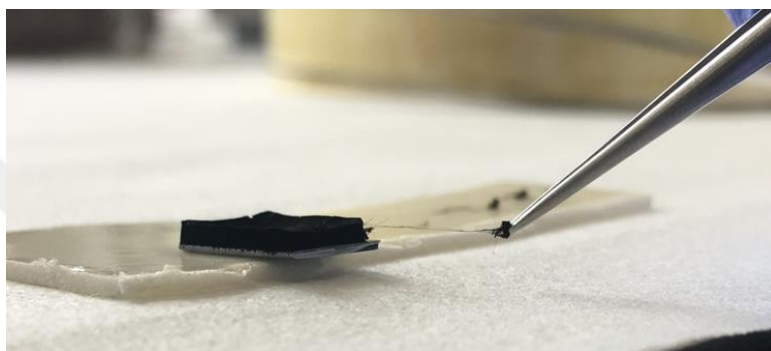


**Figure 4.18:** The spinning of the T-5 set with tweezers.
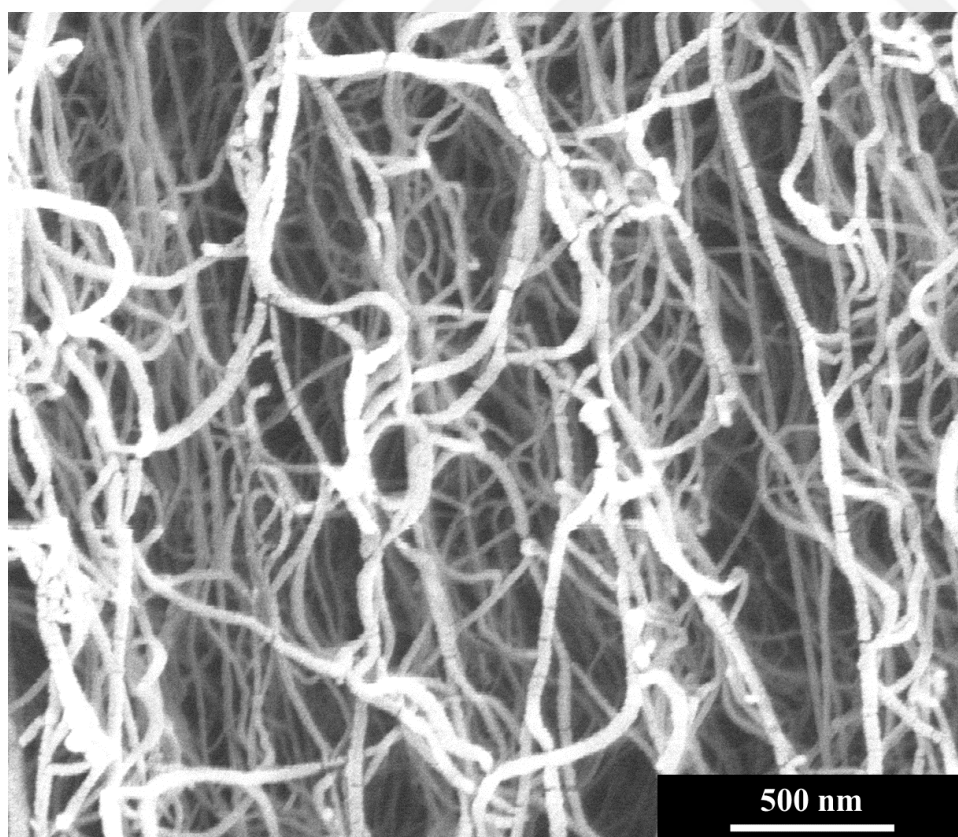


**Figure 4.19:** SEM images of T-5 CNTs forest.

SEM micrographs were examined to understand the inner morphological structure of T-5 CNTs forest, as displayed in. Figure 4.19. The waviness of CNTs were quite detectable. In addition, this T-set of CNTs had been less dense than earlier discussed CNTs sets. The high degree of waviness in CNTs forest was another factor, drastically reduced the spinnability.

In this thesis, protocols inspired from successful studies were also testes as discussed in the previous section Chapter 3.2.2.2. Figure 4.20 shows it was still inconvenient for spinning due to irregular packing, and waviness of structures.

**Table 4.6:** $I_G/I_D$, spinnability index and length of Z and J-sets of CNTs forests.

| Sample Name | Wafer Type | $I_G/I_D$ | Length (µm) | Rank of spinnability |
|---|---|---|---|---|
| Z-1 | SiO$_2$ free | - | - | 0 |
| | SiO$_2$ | - | 1691.4 ± 13.3 | 0 |
| Z-2 | SiO$_2$ free | - | - | 0 |
| | SiO$_2$ | - | 2058.5 ± 11.9 | 0 |
| Z-3 | SiO$_2$ free | - | - | 0 |
| | SiO$_2$ | - | - | 0 |
| Z-4 | SiO$_2$ free | - | - | 0 |
| | SiO$_2$ | - | - | 0 |
| Z-5 | SiO$_2$ free | - | - | 0 |
| | SiO$_2$ | - | - | 0 |
| Z-6 | SiO$_2$ free | - | 1100.6 ± 20.5 | 0 |
| | SiO$_2$ | - | 1155.9 ± 37.7 | 0 |
| Z-7 | SiO$_2$ free | - | - | 0 |
| | SiO$_2$ | - | 482.1 ± 18.9 | 0 |
| J-1 | SiO$_2$ free | - | 1169.8 ± 21 | 0 |
| | SiO$_2$ | - | 704.3 ± 5.4 | 0 |

**Figure 4.20:** Stereomicroscope images of Z and J sets of CNTs forests (a) Z-1 (SiO$_2$ wafer), (b) Z-2 (SiO$_2$ wafer), (c) Z-6 (SiO$_2$ free wafer), (d) Z-6 (SiO$_2$ wafer), (e) Z-7 (SiO$_2$ wafer), (f) J-1 (SiO$_2$ free wafer), (g) J-1 (SiO$_2$ wafer).
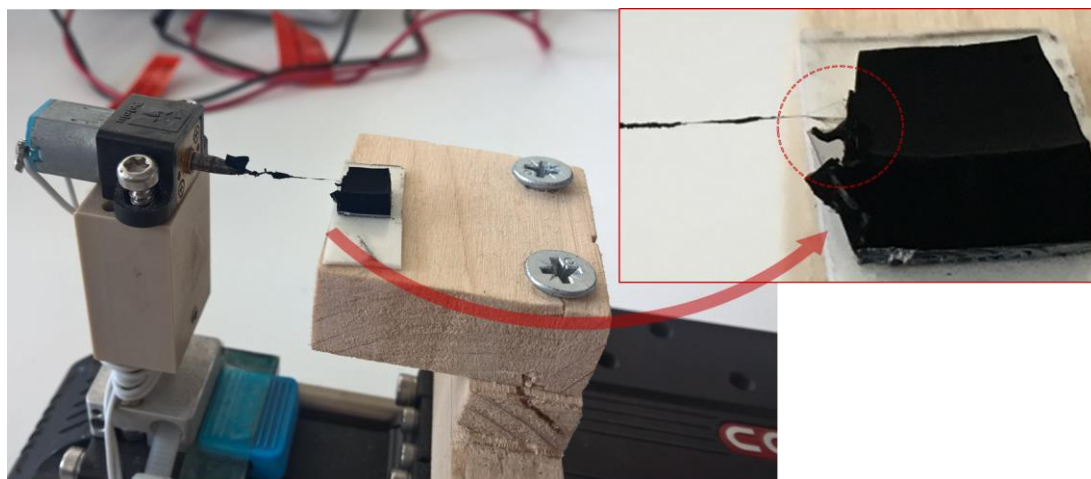


**Figure 4.21:** W-7 CNTs fiber production with custom-made dry spinning device with clear spinning triangle.

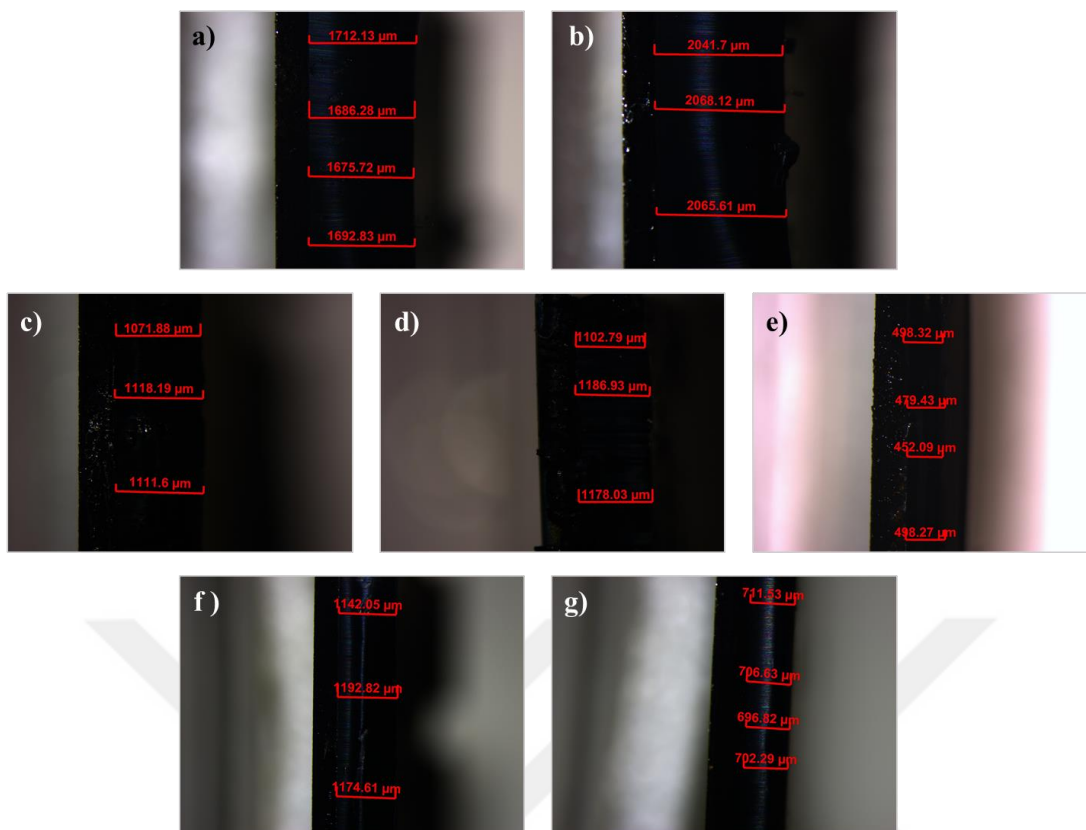This thesis also aimed to design custom-made spinning device for continous twisting. Figure 4.21 shows the implementation of W-7 CNTs forests. First, CNTs were attached to the spindle tip with tweezers. Then this tip was twisted and motion platform pulled back the grabbed fibers. The x-motion was triggered by the lowest possible motor rotation to avoid fiber breakages; yarn twist was given at 200 rpm. Spinning triangle was formed, which was the underpinnings of yarn spinning. However, these fibers were short and the production was not continuous. Spinning triangle did not embrace all CNTs cross-section, which caused to remain some parts untwisted. Figure 4.22 shows the SEM image of this CNTs fiber. The twisting direction depending on the twist direction of spindle end was Z due to clockwise rotation. Z twisted CNTs fiber was locally uniform and yarn diameter was 24.2 ± 3.4 µm. The bias angle was calculated as 40°. This angle could be changed with the twist applied to the fiber. When compared to the spun CNTs fiber bias angles in reference studies, CNTs yarn in Figure 4.23, exhibited much higher twist angle. Studies showed that higher bias angle ratio led to the lower mechanical properties of the CNTs yarns [77]. This angle could be easily reduced by increased x-motion and decreased spindle rotation.



**Figure 4.22:** SEM images of W-7 CNTs yarn.
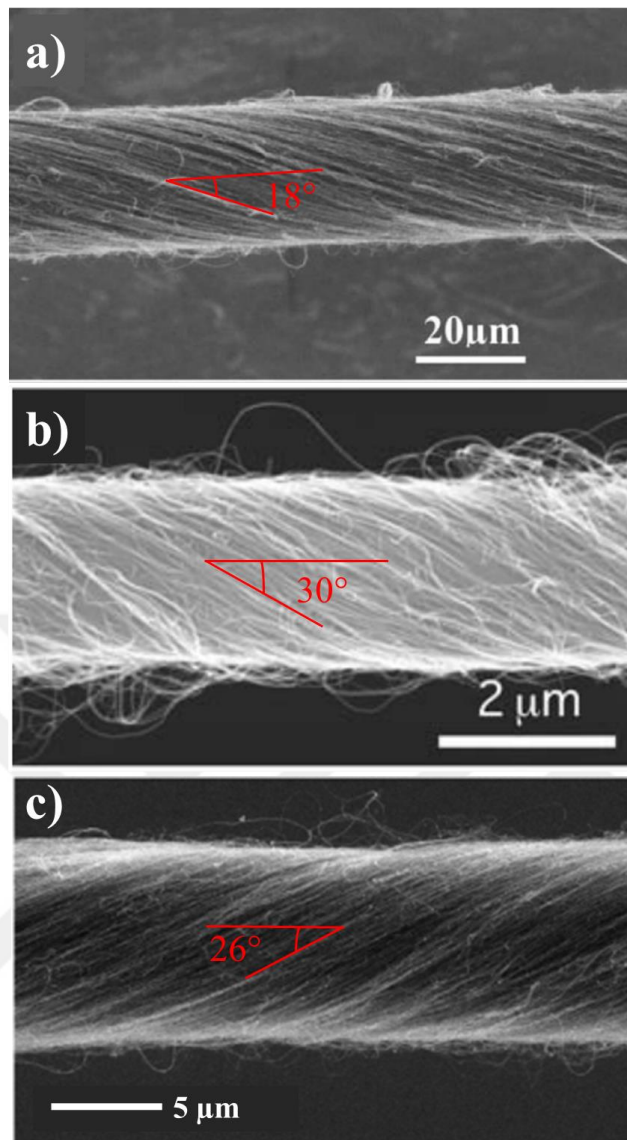
**Figure 4.23:** Some examples of SEM images of CNTs yarns retrieved from a) ref [77], b) ref [78] and c) ref [79].

# 5    CONCLUSION

## 5.1    Concluding Remarks on GO and Graphene Fiber
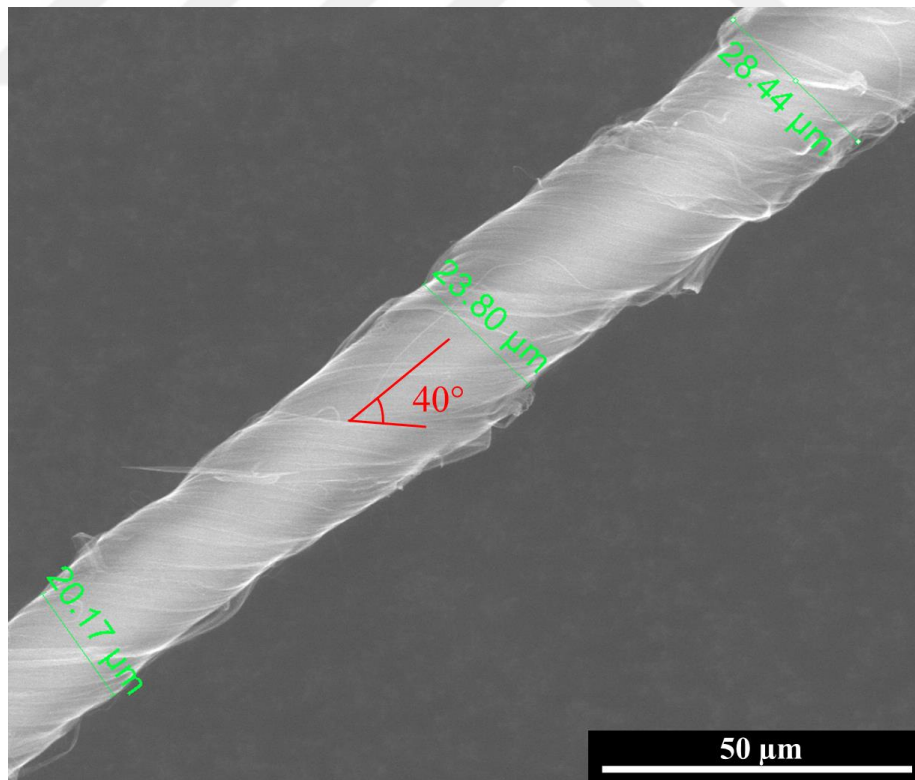
In this thesis, GO was synthesized by modified Hummer's methods. Then, custom-made wet spinning line was used to spin GO fibers continuously. Consecutively, GO fibers were reduced to obtain graphene fibers using chemical reduction methods. Overall,

- GO was produced by the proposed green approach.
    - ➢ Phosphoric acid was used instead of nitric acid, which enabled eco-friendlier processes for GO production
- A continuous wet spinning line was designed and constructed for the scalable production of GO fibers.
    - ➢ Process parameters such as feeding rate, take-up speed *etc*. were optimized.
    - ➢ Material parameters including the coagulation composition and GO concentration were optimized.
- Among three different chemical reduction agents, NaBH$_4$ chemical reduction which was carried out at 2.4 M concentration at 90 °C for 24 hours, had promising electrical conductivity results.

The tensile tested demonstrated that wet-spun GO fibers coagulated in CaCl$_2$ exhibited strain to failure (%) of 10% with higher specific ultimate strength. Through the NaBH$_4$ reduction process ($I_D/I_G = 0.53$), G30C5 revealed the electrical conductivity of 214 S cm$^{-1}$ along the fiber axis. In general, green, non-toxic and scalable production of GO and reduced graphene fibers exhibiting flexibility and high tensile strength had been succeeded, which have potential in emerging applications such as sensor and wearable electronics.

## 5.2 Concluding Remarks on CNTs Fiber

Second objective of this thesis is to spin pure CNTs fibers from CNTs arrays. Hence, dry spinning method was selected for fiber formation. CNTs production was optimized to have spinnable CNTs arrays. The production steps were as follows:

- CVD growth and water-assisted CVD growth systems were used in CNTs synthesis.
- Several protocols by tuning water assistance and its relative concentration, nucleation and growth time, gas fluxes were optimized focused on the spinnability index and the quality of CNTs.
- Growth protocol for spinnable CNTs were optimized.
- Different coated wafers were also used to investigate the spinnability of CNTs forests, which are listed as:
  - ➢ P-type <100> Si wafer and Fe ~2nm
  - ➢ P-type <100> Si wafer, $SiO_2$ ~300 nm, $Al_2O_3$ ~10 nm and Fe ~2nm
  - ➢ P-type <100> Si wafer, $Al_2O_3$ ~10 nm and Fe ~2nm
  - ➢ P-type <100> Si wafer, $Al_2O_3$ ~10 nm and Fe ~6nm

The Raman analysis on the C-sets exhibited $I_D/I_G$ = 2.5. Nevertheless, small bundles observed in the SEM micrographs impeded difficulties in spinning. Continuous dry spinning using custom-made device had not been succeeded. W-sets with water assistance revealed well aligned CNTs whereas they slightly lower quality ($I_D/I_G$=1.79). The results showed that longer growth process caused waviness in CNTs forests and that complicated the spinning. This wavy structure was still present when Fe thickness was increased. Moreover, areal density of CNTs was much lower than the ones in earlier protocols.

W-7 CNTs forests were mounted in custom-made dry spinning device to explore the spinnability. Z twisted CNTs fibers were spun, which had yarn diameter of $24.2 \pm 3.4$ μm. The bias angle was calculated as 40°, which caused preliminary fiber breakages during spinning. As future work, CNTs forests with higher areal density, which were not explored as an output in this thesis, would enable continuous dry spinning with well controlled spinning triangle.

## REFERENCES

[1] *Graphene Scientific Background on the Nobel Prize in Physics.pdf.* THE ROYAL SWEDISH ACADEMY OF SCIENCES, 2010.

[2] **Novoselov, K.S., et al.,** *Electric Field Effect in Atomically Thin Carbon Films.* Science, 2004. **306**: p. 666-669.

[3] **Meng, F., et al.**, *Graphene-Based Fibers: A Review.* Adv Mater, 2015. **27**(35): p. 5113-31.

[4] **Xu, Z. and C. Gao**, *Graphene fiber: a new trend in carbon fibers.* Materials Today, 2015. **18**(9): p. 480-492.

[5] **Terrones, M.,** *Science and Technology of the Twenty-First Century: Synthesis, Properties, and Applications of Carbon Nanotubes.* Annual Review of Materials Research, 2003. **33**(1): p. 419-501.

[6] **Das, S. and W. Choi,** *Graphene Synthesis and Applications*, W. Choi and J.-w. Lee, Editors. 2012, CRC. p. 27-63.

[7] **Viculis, L.M., J.J. Mack, and R.B. Kaner,** *A Chemical Route to Carbon Nanoscrolls.* Science, 2003. **299**(5611): p. 1361.

[8] **Bedeloğlu, A. and Taş, M.,** *Grafen ve Grafen Üretim Yöntemleri.* Afyon Kocatepe Üniversitesi Fen ve Mühendislik Bilimleri Dergisi, 2016. **16**: p. 544-554.

[9] **Acik, M., et al.**, *The Role of Oxygen during Thermal Reduction of Graphene Oxide Studied by Infrared Absorption Spectroscopy.* The Journal of Physical Chemistry C, 2011. **115**(40): p. 19761-19781.

[10] **Jeong, H.-K., et al.**, *Thermal stability of graphite oxide.* Chemical Physics Letters, 2009. **470**(4-6): p. 255-258.

[11] **Pei, S. and H.-M. Cheng,** *The reduction of graphene oxide.* Carbon, 2012. **50**(9): p. 3210-3228.

[12] **Stankovich, S., et al.,** *Synthesis of graphene-based nanosheets via chemical reduction of exfoliated graphite oxide.* Carbon, 2007. **45**(7): p. 1558-1565.

[13] **Li, D., et al.**, *Processable aqueous dispersions of graphene nanosheets.* Nat Nanotechnol, 2008. **3**(2): p. 101-5.

[14] **Shin, H.-J., et al.**, *Efficient Reduction of Graphite Oxide by Sodium Borohydride and Its Effect on Electrical Conductance.* Advanced Functional Materials, 2009. **19**(12): p. 1987-1992.

[15] **Yang, D., et al.,** *Chemical analysis of graphene oxide films after heat and chemical treatments by X-ray photoelectron and Micro-Raman spectroscopy.* Carbon, 2009. **47**(1): p. 145-152.

[16] **Héctor A. Becerril, et al.**, *Evaluation ofSolution-Processed Reduced Graphene Oxide Films as Transparent Conductors.* ACS Nano, 2008. **2**: p. 463–470.

[17] **Xuan Wang, Linjie Zhi, and K. Mullen,** *Transparent, Conductive Graphene Electrodes for Dye-Sensitized Solar Cells.* American Chemical Society, 2008. **8**: p. 323-327.

[18] **Gao, W., et al.**, *New insights into the structure and reduction of graphite oxide.* Nat Chem, 2009. **1**(5): p. 403-8.

[19] **M. J. Ferna´ndez-Merino, et al.,** *Vitamin C Is an Ideal Substitute for Hydrazine in the Reduction of Graphene Oxide Suspensions.* Journal of Physical Chemistry C, 2010. **114**: p. 6426-6432.

[20] **Pei, S., et al.**, *Direct reduction of graphene oxide films into highly conductive and flexible graphene films by hydrohalic acids.* Carbon, 2010. **48**(15): p. 4466-4474.

[21] **Zhu, Y., et al.,** *Graphene and graphene oxide: synthesis, properties, and applications.* Adv Mater, 2010. **22**(35): p. 3906-24.

[22] **Cheng, H., et al.**, *Graphene fibers with predetermined deformation as moisture-triggered actuators and robots.* Angew Chem Int Ed Engl, 2013. **52**(40): p. 10482-6.

[23] **Cote, L.J., R. Cruz-Silva, and J. Huang,** *Flash Reduction and Patterning of Graphite Oxide and Its Polymer Composite.* American Chemical Society, 2009. **131**: p. 11027-11032.

[24] **Yu, D., et al.**, *Scalable synthesis of hierarchically structured carbon nanotube-graphene fibres for capacitive energy storage.* Nat Nanotechnol, 2014. **9**(7): p. 555-62.

[25] **Dong, Z., et al.**, *Facile fabrication of light, flexible and multifunctional graphene fibers.* Adv Mater, 2012. **24**(14): p. 1856-61.

[26] **Xu, Z., et al.**, *Ultrastrong fibers assembled from giant graphene oxide sheets.* Adv Mater, 2013. **25**(2): p. 188-93.

[27] **Xu, Z. and C. Gao,** *Graphene chiral liquid crystals and macroscopic assembled fibres.* Nat Commun, 2011. **2**: p. 571.

[28] **Xu, Z., et al.**, *Highly Electrically Conductive Ag-Doped Graphene Fibers as Stretchable Conductors.* 2013. **25**: p. 3249–3253.

[29] **Cong, H.P., et al.**, *Wet-spinning assembly of continuous, neat, and macroscopic graphene fibers.* Sci Rep, 2012. **2**: p. 613.

[30] **Xiang, C., et al.**, *Large flake graphene oxide fibers with unconventional 100% knot efficiency and highly aligned small flake graphene oxide fibers.* Adv Mater, 2013. **25**(33): p. 4592-7.

[31] **Jalili, R., et al.**, *Wet-spinning of multifunctional graphene fibers using graphene oxide liquid crystals.* Australian Institute for Innovative Materials 2013.

[32] **Huang, G., et al.**, *Highly strong and elastic graphene fibres prepared from universal graphene oxide precursors.* Sci Rep, 2014. **4**: p. 4248.

[33] **Cao, J., et al.**, *Programmable Writing of Graphene Oxide/Reduced Graphene Oxide Fibers for Sensible Networks with in Situ Welded Junctions.* ACS Nano, 2014. **8**: p. 4325-4333.

[34] **Xu, Z., et al.**, *Strong, Conductive, Lightweight, Neat Graphene Aerogel Fibers with Aligned Pores.* ACS Nano, 2012. **6**: p. 7103-7113.

[35] **Liu, Z., et al.**, *Lyotropic Liquid Crystal of Polyacrylonitrile-Grafted Graphene Oxide and Its Assembled Continuous Strong Nacre-Mimetic Fibers.* Macromolecules, 2013. **46**(17): p. 6931-6941.

[36] **Hu, X., et al.**, *Liquid crystal self-templating approach to ultrastrong and tough biomimic composites.* Sci Rep, 2013. **3**: p. 2374.

[37] **Zhao, X., et al.**, *Macroscopic assembled, ultrastrong and H(2)SO(4)-resistant fibres of polymer-grafted graphene oxide.* Sci Rep, 2013. **3**: p. 3164.

[38] **Meng, Y., et al.**, *All-graphene core-sheath microfibers for all-solid-state, stretchable fibriform supercapacitors and wearable electronic textiles.* Adv Mater, 2013. **25**(16): p. 2326-31.

[39] **Cheng, H., et al.**, *Textile electrodes woven by carbon nanotube-graphene hybrid fibers for flexible electrochemical capacitors.* Nanoscale, 2013. **5**(8): p. 3428-34.

[40] **Chen, Q., et al.**, *MnO2-modified hierarchical graphene fiber electrochemical supercapacitor.* Journal of Power Sources, 2014. **247**: p. 32-39.

[41] **Li, J., et al.**, *Flexible graphene fibers prepared by chemical reduction-induced self-assembly.* Journal of Materials Chemistry A, 2014. **2**(18): p. 6359.

[42] **Xiang, C., et al.**, *Graphene Nanoribbons as an Advanced Precursor for Making Carbon Fiber.* ACS Nano, 2013. **7**: p. 1628–1637.

[43] **Naebe, M., T. Lin, and X. Wang**, *Carbon nanotubes reinforced electrospun polymer nanofibres.* 2010.

[44] **Iijima, S.**, *Helical microtubules of graphitic carbon.* Nature, 1991. **354**: p. 56.

[45] **Volder, M.F.L.D., et al.**, *Carbon Nanotubes Present and Future Commercial Application.* Science, 2013. **339**: p. 535-539.

[46] **Thostensona, E.T., Z. Renb, and T.-W. Chou**, *Advances in the science and technology of carbon nanotubes and their composites: a review.* Composites Science and Technology, 2001. **61**: p. 1899–1912.

[47] **Eatemadi, A., et al.**, *Carbon nanotubes properties synthesis purification and medical applications.* Nanoscale Research Letters, 2014. **9**(393).

[48] **Url-1** *<http://physicsworld.com/cws/article/news/>,* date retrieved 16.04.2017.

[49] **Popov, V.**, *Carbon nanotubes: properties and application.* Materials Science and Engineering: R: Reports, 2004. **43**(3): p. 61-102.

[50] **Iijima, S. and T. Ichihashi**, *Single-shell carbon nanotubes of 1-nm diameter.* Nature, 1993. **363**: p. 603-605.

[51] **Tessonnier, J.P. and D.S. Su**, *Recent progress on the growth mechanism of carbon nanotubes: a review.* ChemSusChem, 2011. **4**(7): p. 824-47.

[52] **Smalley, R.E., et al.,** *POLYMER-WRAPPED SINGLE WALL CARBON NANOTUBES*. 2006.

[53] **Jinno, M., S. Bandow, and Y. Ando**, *Multiwalled carbon nanotubes produced by direct current arc discharge in hydrogen gas*. Chemical Physics Letters, 2004. **398**(1-3): p. 256-259.

[54] **Kumar, M. and Y. Ando,** *Chemical Vapor Deposition of Carbon Nanotubes: A Review on Growth Mechanism and Mass Production*. Journal of Nanoscience and Nanotechnology, 2010. **10**(6): p. 3739-3758.

[55] **Dervishi, E., et al.,** *Carbon Nanotubes: Synthesis, Properties, and Applications*. Particulate Science and Technology, 2009. **27**(2): p. 107-125.

[56] **Zhong, X.H., et al.,** *Continuous multilayered carbon nanotube yarns*. Adv Mater, 2010. **22**(6): p. 692-6.

[57] **Ghemes, A., et al.,** *Fabrication and mechanical properties of carbon nanotube yarns spun from ultra-long multi-walled carbon nanotube arrays*. Carbon, 2012. **50**(12): p. 4579-4587.

[58] **Ericson, L.M., et al.,** *Macroscopic, neat, single-walled carbon nanotube fibers*. Science, 2004. **305**(5689): p. 1447-50.

[59] **Zhang, M. and R. Baughman,** *Assembly of Carbon Nanotube Sheets*, in *Electronic Properties of Carbon Nanotubes*, J.M. Marulanda, Editor. 2011. p. 3-17.

[60] **Huynh, C.P. and S.C. Hawkins**, *Understanding the synthesis of directly spinnable carbon nanotube forests*. Carbon, 2010. **48**(4): p. 1105-1115.

[61] **Ghobadi, S., et al.,** *Graphene-reinforced poly(vinyl alcohol) electrospun fibers as building blocks for high performance nanocomposites*. RSC Advances, 2015. **5**: p. 85009-85018.

[62] **Bakhtiari, R., et al.,** *Macroscopic Assembly of Flexible and Strong Green Graphene Fibres*. RSC Advances, 2017. **7**: p. 26735–26744.

[63] **Tian, Z., et al.,** *Self-assembled free-standing graphene oxide fibers*. ACS Appl Mater Interfaces, 2013. **5**(4): p. 1489-93.

[64] **Kim, J.-H., et al.,** *Tuning of Fe catalysts for growth of spin-capable carbon nanotubes*. Carbon, 2010. **48**(2): p. 538-547.

[65] **Jayasinghe, C., et al.,** *Spinning yarn from long carbon nanotube arrays*. Journal of Materials Research, 2011. **26**(05): p. 645-651.

[66] **Yingying Zhang, et al.,** *Tailoring the Morphology of Carbon Nanotube Arrays: From Spinnable Forests to Undulating Foams*. ACS Nano, 2009. **3**: p. 2157–2162.

[67] **DiLeo, R.A., B.J. Landi, and R.P. Raffaelle,** *Purity assessment of multiwalled carbon nanotubes by Raman spectroscopy*. Journal of Applied Physics, 2007. **101**(6): p. 064307.

[68] *Standard Test Method for Tensile Strength and Young's Modulus for High-Modulus Single-Filament Materials*, in *ASTM D3379-75*. 1975, ASTM Standarts.

[69] **Chen, S., et al.,** *Scalable non-liquid-crystal spinning of locally aligned graphene fibers for high-performance wearable supercapacitors.* Nano Energy, 2015. **15**: p. 642-653.

[70] **Park, S., et al.,** *Graphene Oxide Papers Modified by Divalent Ions—Enhancing Mechanical Properties via Chemical Cross-Linking.* ACS Nano, 2008. **2**(3): p. 572-578.

[71] **Kumar, P., et al**., *Rheological properties of graphene oxide liquid crystal.* Carbon, 2014. **80**: p. 453-661.

[72] **Chen, L., et al.,** *Toward high performance graphene fibers.* Nanoscale, 2013. **5**(13): p. 5809-15.

[73] **Zhang, Y., et al.,** *Influence of Al2O3 buffer layer on catalyst morphology and spinnability of carbon nanotube arrays.* Journal of Materials Science, 2017. **52**(11): p. 6196-6204.

[74] **Zheng, L., G. Sun, and Z. Zhan,** *Tuning array morphology for high-strength carbon-nanotube fibers.* Small, 2010. **6**(1): p. 132-7.

[75] **Ürk, D., et al.,** *Understanding the polymer type and CNT orientation effect on the dynamic mechanical properties of high volume fraction CNT polymer nanocomposites.* Composite Structures, 2016. **155**: p. 255-262.

[76] **Kuznetsov, A.A., et al.,** *Structural Model for Dry-Drawing of Sheets and Yarns from Carbon Nanotube.pdf.* ACS Nano, 2011. **5**: p. 985–993.

[77] **Miao, M.,** *The role of twist in dry spun carbon nanotube yarns.* Carbon, 2016. **96**: p. 819-826.

[78] **Zhang, M., K.R. Atkinson, and R.H. Baughman,** *Multifunctional Carbon Nanotube Yarns by Downsizing an Ancient Technology.* Science, 2004. **306**: p. 1358-1361.

[79] **Atkinson, K.R., et al.,** *Multifunctional carbon nanotube yarns and transparent sheets: Fabrication, properties, and applications.* Physica B: Condensed Matter, 2007. **394**(2): p. 339-343.

# CURRICULUM VITAE

Name Surname         : Esma Nur GÜLLÜOĞLU

Place and Date of Birth  : Florida, 11/03/1992

E-Mail                : engulluoglu@gmail.com

## EDUCATION:

B.Sc.                : Textile Engineering/İTU

## EXPERIENCE:

2015-2017      : TUBITAK Project MSc Scholar, ITUARC MSc Member

## PUBLICATIONS, PRESENTATIONS AND PATENTS ON THE THESIS

**Esma Nur Gulluoglu,** Lale Işıkel Şanlı, Elif Özden Yenigün, Selmiye Alkan Gürsel, Saijad BGhobadi, Rokhsareh Bakhtiari, Mechanical Properties of Continuous Graphene Oxide Fibers Prepared By Wet Spinning, 7 th European Conference on Protective Clothing, İzmir, Turkey 23-25 May 2016

Rokhsareh Bakhtiari, Sajjad Ghobadi, **Esma Nur Gulluoglu**, Lale Işıkel Şanlı, Selmiye Alkan Gürsel, Elif Özden-Yenigün, "Macroscopic Assembly of Flexible and Strong Green Graphene Fibers", RSC Advances, 2017, 7, 26735-26744